Elastic Modelling of Deformation Twinning on the Microscale

Dissertation

zur Erlangung des akademischen Grades

Doktoringenieurin / Doktoringenieur (Dr.-Ing.)

von Dipl.-Ing. Rainer Glüge,

geb. am 16.04.1980 in Magdeburg,

genehmigt durch die Fakultät für Maschinenbau

der Otto-von-Guericke-Universität Magdeburg.

Gutachter:

Prof. Dr.-Ing. habil. Albrecht Bertram
Prof. Dr.-Ing. habil. Thomas Böhlke
Prof. Dr. rer. nat. habil. Werner Skrotzki

Promotionskolloquium am 4.12.2009

Summary

Upon mechanical loading, many crystals develop crystal twins, which has to be considered as a special deformation mechanism. In contrast to crystallographic glide, twinning enables a crystal to accommodate rapid deformations at low temperatures, which may be exploited to expand the range of application of a material. However, twinning affects strongly the material properties, which is not always beneficial. The twins form as plates inside of grains, and alter significantly the morphological and the crystallographic texture, both influencing the yield locus and the elastic anisotropy, while the additional interfaces have an impact on the strain hardening. Moreover, the twinning mechanism is polar, which can cause a pronounced differential effect on the strength of the material and the forming limit, depending on the crystallographic texture. For many materials, these effects are not negligible. Especially the ductile TWIP steels and the lightweight hcp metals, magnesium and titanium, which are interesting for engineering applications, display extensive twin formation at room temperature. One is therefore interested in a proper modelling of twinning. One approach, proposed by Ericksen (1975), is to treat twinning as isothermal phase changes by a non-convex elastic modelling. In this work, a micro-mechanical elastic modelling approach for $\langle 0111 \rangle \{ 011\bar{2} \}$ twinning in magnesium is developed. It is coupled with basal glide, another dominant deformation mode encountered in most hexagonal crystals. The approach allows to compare simulation results to experimental findings on the microscale and, by numerical homogenisation by the representative volume element technique (RVE), to experimental findings on the macroscale.

Chapter 1 serves as an introduction, were the framework for the model derivation is set up. **Chapter 2** is dedicated to the geometrical description and classification of twins, the twin formation and their impact on the material properties. Different simulation techniques on the different scales are discussed in **chapter 3**. **Chapter 4 and 5** are devoted to the development of the microscale model, where the basic model is derived in **chapter 4** and modified in **chapter 5**. In **chapter 4**, the energy invariance in compound twins and its implications for the elastic modelling are discussed, as well. The material law is summarized in **chapter 6**, where a section is dedicated to the implementation of the crystallographic glide. In **chapter 7**, different simulation results are presented, namely three different FE-models that are settled on the microscale, while one FE simulation allows by numerical homogenization for a comparison with experiments conducted on the macroscale. The work is summarized in **chapter 8**, and a short outlook is given.

Zusammenfassung

Die vorliegende Arbeit behandelt die mechanisch induzierte Zwillingsbildung. Diese kann als sehr spezielle, isotherme kristallographische Umwandlung aufgefasst werden. Solche Festkörper zu Festkörper-Umwandlungen induzieren eine Reihe interessanter und ingenieurtechnisch nutzbarer Effekte. Zum Beispiel basiert der Formgedächtniseffekt auf der thermisch induzierten Martensit zu Austenit Umwandlung, während die augenscheinlich irreversiblen Deformationen in der Martensitphase durch das Verschieben von Grenzflächen zwischen Zwillingen realisiert werden. Als weiteres Beispiel ist die Zwillingsinduzierte Plastizität zu nennen. Sie kann gerade wenn kristallographisches Gleiten schwer aktivierbar ist, z.B. bei niedrigen Temperaturen und hohen Dehnraten, als alternativer Deformationsmechanismus zur Verfügung stehen. Allerdings hat die Zwillingsbildung einen starken Einfluss auf das Materialverhalten. Hier können Materialmodelle beim Verstehen und Vorhersagen der durch Zwillingsbildung verursachten Verfestigung und Texturentwicklung hilfreich sein. Ziel dieser Arbeit ist die Entwicklung eines Materialmodells, welches die Zwillingsbildung auf der Kristallebene beschreibt. Die Modellierung erfolgt im Kern durch die Kopplung eines pseudoelastischen Gesetzes mit einer viskosen Bewegungsgleichung. Dabei wird sich auf Zwillingsbildung in Magnesium und Magnesiumlegierungen konzentriert, wofür es mehrere Gründe gibt. Magnesium ist wegen seiner geringen Dichte für den Leichtbau interessant, allerdings sind Magnesiumlegierungen wegen ihrer geringen Duktilität hauptsächlich als Gussteile anzutreffen. Die Zwillingsbildung spielt für die Umformbarkeit von Magnesium und seinen Legierungen eine wichtige Rolle. Gerade stranggepresste Magnesiumlegierungen, deren Verwendung als Halbzeug bisher eine untergeordnete Bedeutung hat, zeigen aufgrund einer starken Textur eine ausgeprägte, durch Zwillingsbildung verursachte Zug-Druck-Anisotropie, was sowohl die Fließspannung als auch die Umformbarkeit betrifft. Dementsprechend umfangreich sind die zum Thema verfügbare Literatur und experimentelle Befunde, welche zum Vergleich mit Simulationen zur Verfügung stehen. Daher wurde das Modell für die häufig angetroffene $\langle 0111 \rangle \{ 011\bar{2} \}$ Zwillingsbildung implementiert.

Kapitel 1 dient der Einführung und steckt den Rahmen ab, innerhalb dessen das Materialmodell entwickelt wird. **Kapitel 2** befasst sich mit der geometrischen Beschreibung und der Klassifizierung der Zwillinge, sowie der Entstehung und dem Einfluss, den Zwillingsbildung auf das Materialverhalten hat. In **Kapitel 3** werden Simulationstechniken auf verschiedenen Skalen diskutiert. **Kapitel 4** und **5** sind der Entwicklung des Materialmodells gewidmet, wobei in Kapitel 4 nach einem Ansatz von Ball und James die elastische Energie entwickelt wird, welche in Kapitel 5 modifiziert wird. In Kapitel 4 wird ebenfalls die Energieinvarianz in sogenannten Compound-Twins diskutiert, sowie deren Bedeutung für die elastische Modellierung. Die Materialgleichungen werden in **Kapitel 6** zusammengefasst, wobei auf die numerische Implementierung des kristallographischen Gleitens eingegangen wird. In **Kapitel 7** werden verschiedene Simulationsergebnisse präsentiert, wobei die ersten drei Finite-Elemente-Modelle auf der Mikroebene angesiedelt sind, während das vierte FE-Modell einen Vergleich zu experimentellen Befunden auf der Makroebene erlaubt. Die Arbeit schließt mit **Kapitel 8** mit einer Zusammenfassung der Ergebnisse und Überlegungen zu zukünftigen Arbeiten ab.

Danksagung

Diese Arbeit entstand in den Jahren 2005-2009 während meiner Zeit als Stipendiat und wissenschaftlicher Mitarbeiter am Institut für Mechanik, an der Otto-von-Guericke-Universität in Magdeburg. Mir kam im Rahmen einer Landesgraduiertenstelle finanzielle Unterstützung durch das Kultusministerium des Landes Sachsen-Anhalt und dem von der DFG finanzierten Graduiertenkolleg 828 *„Micro-Macro Interactions in Structured Media and Particle Systems”* zugute, in welchem ich assoziiertes Mitglied war. Die finanzielle Unterstützung sowie der Austausch im Graduiertenkolleg waren beim Erstellen dieser Arbeit äußerst hilfreich.
Ich bedanke mich herzlich bei Prof. Albrecht Bertram und Prof. Thomas Böhlke für die Unterstützung. Die vorliegende Arbeit hätte ohne die von ihnen vermittelten Kenntnisse nicht angefertigt werden können. Die von Prof. Bertram angebotenen Kurse *Festigkeitslehre* und *Nichtlineare Kontinuumsmechanik* lieferten die für die Arbeit benötigten theoretischen Grundlagen, während Prof. Böhlke mir im während meiner Studienarbeiten und meiner Diplomarbeit das Rüstzeug zur numerischen Implementierung von Materialmodellen vermittelte. Desweiteren genoss ich das Privileg, die Schwerpunkte der Arbeit und die Vorgehensweise selbst wählen zu können. Ich bedanke mich ebenfalls recht herzlich bei Prof. Werner Skrotzki, der sich trotz des Organisationsaufwandes zur „15th International Conference on the Strength of Materials” die Zeit nahm als Gutachter meiner Arbeit zu fungieren.
Das angenehme und kollegiale Arbeitsklima am Institut trug maßgeblich zum Gelingen der Arbeit bei, wofür ich mich bei allen Kollegen bedanke. Spezieller Dank für hilfreiche Diskussionen und Anregungen gilt Jan Kalisch, Thorsten Hoffmann, Sebastian Borsch und Janko Kreikemeier. Bei Prof. Doris Regener und ihrem Team möchte ich mich für die Beschaffung des Materials und die Unterstützung beim experimentellen Teil der Arbeit bedanken, bei Prof. Franz Dieter Fischer, Prof. Alexander Mielke, Prof. Gerald Warnecke und Dr. Peter Streitenberger für anregende Diskussionen.

Magdeburg, Dezember 2009 Rainer Glüge

Contents

List of Figures

Chapter 1

Preliminaries

1.1 Introduction

Deformation twinning can be understood as a special deformation mode available in crystals. A crystal that undergoes twinning reorients its lattice without changing the symmetry class, unlike martensitic transformations. The twin configuration is achieved by a simple shear deformation of the parent crystal, while the crystallographic structure of the twin differs only by a rotation or a mirror operation from the parent one, which motivates the term ”twinning”. In real crystals the twins appear as lamellae, which are aligned approximately coplanar to the shear plane. A micrograph of a twin network in magnesium is given in Fig. 1.1, where the twins are aligned along characteristic planes. Mechanical twinning was propably firstly observed by Ewing and Rosenhain (1900). In mineralogy, crystal twinning was well known in the 19th century (Naumann, 1830).

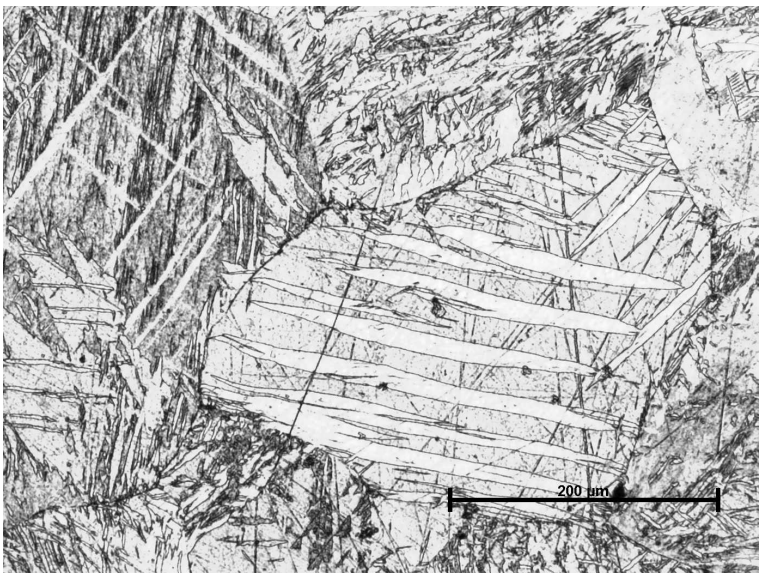

Figure 1.1: Light optical photograph of a polished magnesium sample.

The common view on the twin formation is that so called transformation dislocations exist in the crystal, which dissociate when a stress is applied, and accumulate at nucleation sites. Transformation

dislocations can also be generated. The nuclei are formed by dislocation walls, which enclose a small twinned volume. This nucleus then grows by moving the dislocation walls, which at some instance become large enough to be considered as interfaces. Mostly, twins become self-sustained at a certain size. The elastic misfit strain gives rise to further twin growth, until a sufficiently large counter-force or an obstacle is met. This causes the twinning induced load drops in the stress-strain curves. One can speak about a twin as a very special type of grain, recognisable by its shape, grain boundary orientation and lattice orientation with respect to the surrounding grain.

Twinning contributes strongly to the mechanical properties. By the lattice reorientation, twinning alters the crystal orientation distribution (COD, crystallographic texture), and by subgrain growth the grain morphology (morphologic texture). Both alterations affect, among other properties, the macroscopic elastic modulus and the yield locus. Further, twinning is polar, i.e., unlike crystallographic slip, the shear deformation is possible only in one direction. Twinning is available at high strain rates and low temperatures, and can therefore compensate the lack of crystallographic glide under the latter conditions. Twinning is targeted for in manganese alloyed steels (TWIP-steels, Twinning-Induced Plasticity, Grassel and Frommeyer (1998); Karaman et al. (2000); Frommeyer et al. (2003)), which can accommodate unusual large strains at room temperature mostly by deformation twinning.

For a suitable material modelling of materials that undergo deformation twinning, the underlying deformation mechanism has to be incorporated. For this purpose, many macroscale models have been proposed (e.g. Tomé et al. (1991); Staroselsky and Anand (2003)). They include twin formation in a homogenised sense, and account for one or more aspects of twinning, like the grain refinement or the texture evolution. One method to set up a macroscale model is to propose constitutive equations describing macroscopic quantities, which are adjusted to experiments. It is problematic to show that such a model is applicable to other processes than the experimental ones to which it has been adapted. Another method to derive macroscale constitutive equations is to apply an analytical homogenisation scheme to microscale constitutive equations, which are physically motivated. Here, the necessarily rough homogenisation (mostly the Taylor assumption) may lead to results that are not sufficiently accurate. It is highly complicated, if not impossible, to set up a macroscale material model that can incorporate, e.g., a grain morphology, a texture and a deformation path, which yields precise predictions of the material behaviour. Nevertheless, macromodels are important tools in industrial design. Their advantage is the numerical efficiency, and that one can choose a model that explicitely accounts for ones needs.

Another way to incorporate twinning on the macroscale is to use a numerical homogenisation scheme in conjunction with a microscale model. Following this way, one has to set up a material model that includes twinning only for a single crystal, while the homogenisation procedure is done numerically. An example would be the FE^2 method, where at each integration point (or at certain key points) of the macroscopic model another FE model of a representative volume element (RVE) is incorporated. The micromodel has to be adjusted only to the behaviour of a single crystal, which leaves few physically motivated parameters that have to be adjusted to an easy reproduceable experiment. It can be expected that the latter approach yields more precise predictions of the material behaviour than a macroscale model. The most significant disadvantage of the FE^2 method is the high computational effort when applied to engineering problems.

In this work, a microscale-model for deformation twinning based on a nonconvex elastic energy density is developed. Due to the twinning-induced rearrangement of the atoms, the lattice vectors do not behave like material vectors. This has to be regarded as a violation of the Cauchy-Born rule

(Born and Huang, 1954), which is so fundamental in the theory of elasticity that it is mostly adapted intuitively and without explicit declaration. The consequences of this violation have to be analysed in order to determine the limitations of a theory that models deformation twinning by means of elasticity. It is demonstrated that all compound twins exhibit an elastic energy invariance, and the consequences for the elastic modelling are discussed. Finally, the model is tested in characteristic FE simulations, which are comparable to experimental setups. The findings are summarised, and an outlook for future work is given.

1.2 List of Symbols

a edge length of the base hexagon in a hcp lattice, page 28
a_i regularisation element, page 57
c height of the unit cell of a hcp lattice, page 28
E elastic modulus (1D example), page 50
F force (1D example), page 50
G shear modulus, page 79
k regularisation parameter, page 57
k_B Boltzmann constant, page 56
u displacement (1D example), page 50
w context dependent, strain energy density or specific interface energy, page 39

δ_{ij} Kronecker symbol, page 23
γ amount of shear, page 14
γ_0 twinning shear, page 31
γ_{twin} critical twinning shear, page 81
λ projection distance parameter, page 79
η viscosity, page 53
Ω domain occupied by an elastic body, page 50
ϕ context dependent indicator function, page 79
τ context dependent shear stress, page 37
θ absolute temperature, page 56

$\boldsymbol{a}_i$ hexagonal lattice base vectors inside the basal plane, page 28
$\boldsymbol{c}$ hexagonal lattice base vector parallel to the cylinder axis, page 28
$\boldsymbol{d}$ shear direction, page 14
$\boldsymbol{d}^*$ normalised slip direction, page 74
$\boldsymbol{e}_i$ orthonormal basis, page 12
$\boldsymbol{k}$ vector of the plane of shear, page 14
$\boldsymbol{k}_{1,2}$ first and second twin plane in the classical twin notation, page 17
$\boldsymbol{k}'_{1,2}$ first and second twin plane after twinning in the classical twin notation, page 17
$\boldsymbol{n}$ (shear) plane normal, page 14
$\boldsymbol{p}_i$ lattice basis generating the parent lattice, page 20
$\boldsymbol{t}_i^{(\prime)}$ lattice basis generating the twin lattice, page 20
$\boldsymbol{u}$ displacement vector, page 14

$\boldsymbol{\eta}_{1,2}$ first and second shear direction in the classical twin notation, page 17

$\boldsymbol{C}$ right Cauchy Green tensor, page 61
$\boldsymbol{E}$ Green's strain tensor, page 56
$\boldsymbol{E}_{\mathrm{crit}}$ critical strain state, page 81
$\boldsymbol{F}$ deformation gradient, page 14
$\boldsymbol{H}$ displacement gradient, page 14
$\boldsymbol{I}$ second-order identity tensor on vectors, page 12
$\boldsymbol{P}$ plastic transformation, page 61
$\boldsymbol{Q}_{\beta\boldsymbol{v}}$ orthogonal second-order tensor, page 12
$\boldsymbol{R}_{\boldsymbol{v}}$ rotation of amount π around the axis $\boldsymbol{v}$, page 12
$\boldsymbol{S}$ deformation gradient of a simple shear deformation, page 14
$\boldsymbol{T}$ second Piola-Kirchhoff stresses, page 56
$\boldsymbol{T}_{\mathrm{crit}}$ critical stress state, page 79

$\boldsymbol{\sigma}$ Cauchy stresses, page 73

$\mathbb{C}_0$ reference stiffness tetrad, page 61
$\mathbb{I}^S$ Fourth-order identity tensor on symmetric second-order tensors, page 83

$[A]$ invertible integer matrix the inverse of which contains only integers, page 21

Inv set of invertible matrices, page 21
Inv^+ set of invertible second-order tensors with positive determinant, page 20
$Orth^+$ set of orthogonal second-order tensors with positive determinant, page 20
$Shear$ set of second-order tensors denoting a shear deformation, page 15
$\mathbb{Z}$ set of integer numbers, page 21

1.3 Notation

Throughout the work a direct tensor notation is preferred. If an expression cannot be represented in the direct notation without introducing new conventions, its components are given with respect to orthonormal base vectors $\boldsymbol{e}_i$, using the summation convention. Vectors are symbolised by lowercase bold letters $\boldsymbol{v} = v_i\boldsymbol{e}_i$, second-order tensors by uppercase bold letters $\boldsymbol{T} = T_{ij}\boldsymbol{e}_i \otimes \boldsymbol{e}_j$ or bold greek letters. The second-order identity tensor is denoted by $\boldsymbol{I}$. Fourth-order tensors are symbolised like $\mathbb{C}$. The dyadic product is defined as $(\boldsymbol{a}\otimes\boldsymbol{b})\cdot\boldsymbol{c} = (\boldsymbol{b}\cdot\boldsymbol{c})\boldsymbol{a}$. Matrices are denoted like $[A]$. A dot represents a scalar contraction. If more than one scalar contraction is carried out, the number of dots corresponds to the number of vectors that are contracted, thus $\boldsymbol{a}\otimes\boldsymbol{b}\otimes\boldsymbol{c}\cdot\cdot\,\boldsymbol{d}\otimes\boldsymbol{e} = (\boldsymbol{b}\cdot\boldsymbol{d})(\boldsymbol{c}\cdot\boldsymbol{e})\boldsymbol{a}$, $\alpha = \boldsymbol{A}\cdot\cdot\,\boldsymbol{B}$ and $\boldsymbol{\sigma} = \mathbb{C}\cdot\cdot\,\boldsymbol{\varepsilon}$. When only one scalar contraction is carried out, the scalar dot is frequently omitted, e.g., $\boldsymbol{v} = \boldsymbol{F}\boldsymbol{w}$, $\boldsymbol{A} = \boldsymbol{B}\boldsymbol{C}$. The Rayleigh-product is defined by applying a second-order tensor to the base vectors of a tensor. In case of a fourth-order tensor, $\boldsymbol{P} * \mathbb{C} = C_{ijkl}\boldsymbol{P}\boldsymbol{e}_i \otimes \boldsymbol{P}\boldsymbol{e}_j \otimes \boldsymbol{P}\boldsymbol{e}_k \otimes \boldsymbol{P}\boldsymbol{e}_l$, with $\mathbb{C} = C_{ijkl}\boldsymbol{e}_i \otimes \boldsymbol{e}_j \otimes \boldsymbol{e}_k \otimes \boldsymbol{e}_l$. Orthogonal tensors are denoted by $\boldsymbol{Q}_{\beta\boldsymbol{v}} = \tilde{\boldsymbol{e}}_i \otimes \boldsymbol{e}_i$, mapping one orthonormal basis $\boldsymbol{e}_i$ into another one $\tilde{\boldsymbol{e}}_i$. If $\boldsymbol{Q}$ can be interpreted as a rotation, the optional indexing contains the amount of rotation β and the normalised axial vector $\boldsymbol{v}$. Two-fold rotations are rotations of amount π. They are denoted as $\boldsymbol{R}_{\boldsymbol{v}} = -\boldsymbol{I} + 2\boldsymbol{v}\otimes\boldsymbol{v}$, with $\boldsymbol{v}$ being the normalised axial vector. The derivative, e.g., of a vector valued vector function with respect to its argument is denoted like $\boldsymbol{v}'(\boldsymbol{w}) = \partial\boldsymbol{v}(\boldsymbol{w})/\partial\boldsymbol{w} = \partial v_i/\partial w_j\ \ \boldsymbol{e}_i \otimes \boldsymbol{e}_j$. The material time derivative is indicated by a dot, placed

above the function under consideration.

1.4 Two-fold Rotations, Reflections and Self-Inverseness

$\boldsymbol{R_v}$ are referred to as two-fold rotations. They are orthogonal and symmetric, i.e. $\boldsymbol{R_v} = \boldsymbol{R_v}^T = \boldsymbol{R_v}^{-1}$. $-\boldsymbol{R_v}$ has the same properties, but represents a reflection on the plane normal to the axial vector of the rotation. A basis undergoes a central inversion if mapped by $-\boldsymbol{R_v}$ instead of $\boldsymbol{R_v}$, which does not affect the simple lattice generated by the basis that is obtained. Note that

$$\boldsymbol{R}_{\boldsymbol{e}_1}\boldsymbol{R}_{\boldsymbol{e}_2}\boldsymbol{R}_{\boldsymbol{e}_3} = \boldsymbol{I}, \tag{1.1}$$

which allows us in conjunction with the self-inverseness to write

$$\boldsymbol{R}_{\boldsymbol{e}_1} = \boldsymbol{R}_{\boldsymbol{e}_2}\boldsymbol{R}_{\boldsymbol{e}_3}, \tag{1.2}$$

or, using mirror operations,

$$-\boldsymbol{R}_{\boldsymbol{e}_1} = -\boldsymbol{R}_{\boldsymbol{e}_2}\boldsymbol{R}_{\boldsymbol{e}_3} \tag{1.3}$$

$$\boldsymbol{R}_{\boldsymbol{e}_1} = (-\boldsymbol{R}_{\boldsymbol{e}_2})(-\boldsymbol{R}_{\boldsymbol{e}_3}). \tag{1.4}$$

Mirror symmetries give rise to the Coxeter groups, although not all Coxeter groups can be described using only reflections. It is pointed out that from the viewpoint of application to simple lattices, the use of reflections or two-fold rotations is equivalent. Further, $\boldsymbol{R_v} = \boldsymbol{R_{-v}}$ holds, i.e. only the direction of the axial vector, but not the sense of direction matters.

Note that a tensor that is orthogonal and symmetric is self-inverse, but not all self-inverse tensors must be symmetric. Let $\boldsymbol{M}$ be a self-inverse tensor. Its eigenvalues can only take the values ± 1. Its projector representation is given by $\boldsymbol{M} = \boldsymbol{P}_1 - \boldsymbol{P}_2$, with $\boldsymbol{P}_1 = \frac{1}{2}(\boldsymbol{I} + \boldsymbol{M})$ and $\boldsymbol{P}_2 = \frac{1}{2}(\boldsymbol{I} - \boldsymbol{M})$. Note that $\boldsymbol{P}_i\boldsymbol{P}_i = \boldsymbol{P}_i$, and $\boldsymbol{P}_1 + \boldsymbol{P}_2 = \boldsymbol{I}$. In case of the two-fold rotations, one obtains $\boldsymbol{P}_1 = \boldsymbol{v} \otimes \boldsymbol{v}$ and $\boldsymbol{P}_2 = \boldsymbol{I} - \boldsymbol{v} \otimes \boldsymbol{v}$.

1.5 Continuum Mechanics

The modelling framework employed in this work is continuum mechanics, a theory based on the proposition of a continuous distribution of matter in space. The common treatment is to index the infinitely many material points of a body with $\boldsymbol{X}$, and spatial points with $\boldsymbol{x}$. A placement of the body assigns the material points to spatial points by $\boldsymbol{x} = \boldsymbol{\phi}(\boldsymbol{X})$. A motion of a body is given by a continuous change of placement, denotable as $\boldsymbol{x} = \boldsymbol{\chi}(\boldsymbol{X}, t)$. Note that often more elaborate definitions are used (Korobeynikov, 2008), but not needed here.

Usually, a reference placement is introduced. Since the coordinates X_i, x_i and t can be chosen freely, they are chosen mostly such that $\boldsymbol{x} = \boldsymbol{X}$ at $t = 0$ holds, which is called reference placement. This is presumed in the remainder. The use of this distinguished placement simplifys the treatment of standard elastic bodies, because the stress-free placements differ only by a rigid body motion, and the

stresses are denoteable in terms of a deviation from the stress-free placement in the elastic law. It is of limited benefit, e.g., in fluid mechanics. With respect to the reference placement one can denote the displacement vector $\boldsymbol{u} = \boldsymbol{x}(\boldsymbol{X}, t) - \boldsymbol{X}$. Further, the displacement gradient $\boldsymbol{H} = \partial \boldsymbol{u}/\partial \boldsymbol{X} = \partial \boldsymbol{x}/\partial \boldsymbol{X} - \boldsymbol{I}$ and the deformation gradient $\boldsymbol{F} = \partial \boldsymbol{x}/\partial \boldsymbol{X} = \boldsymbol{H} + \boldsymbol{I}$ are introduced. The deformation gradient $\boldsymbol{F}$ maps a line element from the reference placement to the actual placement. By applying the polar decomposition theorem $\boldsymbol{F} = \boldsymbol{Q}\boldsymbol{U} = \boldsymbol{V}\boldsymbol{Q}$, one can define strain measures with respect to the stretching in the material or the spatial placement by using either $\boldsymbol{U}$ or $\boldsymbol{V}$, respectively. In solid mechanics usually a material strain measure is used. For a comprehensive account on continuum mechanics see, e.g., Liu (2002); Bertram (2005).

1.6 Simple Shear Deformation

Since simple shear deformations play the leading part when twinning is examined, some explanations regarding shear deformations should be given. Consider Fig. 1.2, where the shear deformation of a cuboid is sketched. The shear deformation can be imagined as a deck of cards that glide along

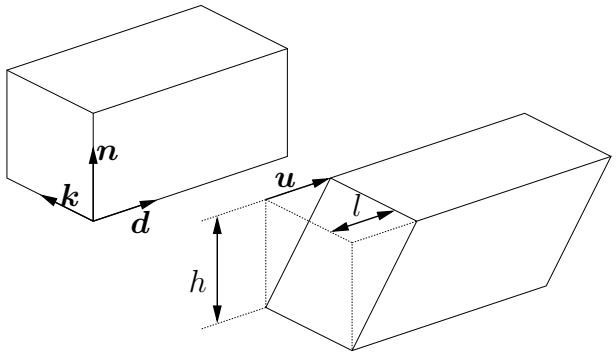

Figure 1.2: Simple shear deformation of a cuboid.

each other. Thus, the characteristic measures are the card deck normal $\boldsymbol{n}$, which is called shear plane normal, and the glide direction $\boldsymbol{d}$, which is called shear direction. $\boldsymbol{n}$ and $\boldsymbol{d}$ are normalised and perpendicular to each other. As a measure for the amount of shear the shear number $\gamma = l/h$ is introduced (see Fig. 1.2). The amount of glide of a plane parallel to the shear plane is proportional to the distance from the base plane. In the example, the displacement of the upper plane is $\boldsymbol{u}(h) = \gamma h \boldsymbol{d}$, with h denoting the distance from the base plane. The displacement gradient is therefore

$$\boldsymbol{H}_{\mathrm{ss}} = \frac{\partial \boldsymbol{u}}{\partial \boldsymbol{X}} = \gamma \boldsymbol{d} \otimes \frac{\partial h}{\partial \boldsymbol{X}} = \gamma \boldsymbol{d} \otimes \frac{\partial (\boldsymbol{X} \cdot \boldsymbol{n})}{\partial \boldsymbol{X}} = \gamma \boldsymbol{d} \otimes \boldsymbol{n}. \tag{1.5}$$

Commonly, γ is put into $\boldsymbol{d}$, at cost of the convenience of working with a normalised $\boldsymbol{d}$. In this work, γ and $\boldsymbol{d}$ are kept separately. Then the tensor $\boldsymbol{d} \otimes \boldsymbol{n}$ can be referred to as Schmid tensor or slip system tensor. Further, it is made use of the plane of shear, denoted by the normal vector $\boldsymbol{k} = \boldsymbol{n} \times \boldsymbol{d}$. $(\boldsymbol{n}, \boldsymbol{d}, \boldsymbol{k})$ form a positively oriented orthonormal basis.

The tensor $\boldsymbol{H}_{\mathrm{ss}}$ is a rank one tensor, which can be denoted by only one base dyad. The corresponding deformation gradient is given by $\boldsymbol{S} = \boldsymbol{I} + \boldsymbol{H}_{\mathrm{ss}}$. In the sequel, deformation gradients that describe a simple shear deformation are denoted by $\boldsymbol{S}$, and the set of all deformation gradients denoting a shear

deformation is written as $Shear = \{\boldsymbol{I} + \gamma \boldsymbol{d} \otimes \boldsymbol{n} | \boldsymbol{n} \cdot \boldsymbol{n} = 1, \boldsymbol{d} \cdot \boldsymbol{d} = 1, \boldsymbol{d} \cdot \boldsymbol{n} = 0, \gamma \in \mathbb{R}\}$. Shear deformations are isochoric, i.e. $\det(\boldsymbol{S}) = 1$.

Chapter 2

Mechanical Twinning

2.1 Usual Twin Description

In the literature, twins are mostly described by the twinning elements $\boldsymbol{k}_1$, $\boldsymbol{k}_2$, $\boldsymbol{\eta}_1$ and $\boldsymbol{\eta}_2$ (Fig. 2.1, see Pitteri and Zanzotto (2002) for a comprehensive description). $\boldsymbol{k}_1$ and $\boldsymbol{k}_2$ should not be confused with $\boldsymbol{k}$ introduced in section 1.6. $\boldsymbol{k}_1$ represents the shear plane, also referred to as the invariant plane. $\boldsymbol{\eta}_1$ indicates the shear direction, and $\boldsymbol{k}_2$ represents the one plane that is simply rotated but not stretched by the simple shear deformation, also referred to as the second undistorted plane. $\boldsymbol{k}_2'$ denotes the plane $\boldsymbol{k}_2$ after applying the twinning shear, respectively after mirroring or rotating the plane $\boldsymbol{k}_2$ accordingly. The twin lattice is obtained by mirroring the parent lattice at the shear plane $\boldsymbol{k}_1$ (type 1 twinning) or at the plane normal to the shear direction $\boldsymbol{\eta}_1$ (type 2 twinning). If $\boldsymbol{k}_1$ and $\boldsymbol{k}_2$ are rational, i.e., crystallographically embedded, one speaks of compound twins. In that case, both orientation relations hold. The term "compound twin" has been introduced by Cahn (1953). In many cases, $\boldsymbol{k}_1$ and $\boldsymbol{k}_2$ are even crystallographically equivalent. Then, $\boldsymbol{\eta}_2$ gives the shear direction for twinning along the plane $\boldsymbol{k}_2$, and the pairs $\boldsymbol{k}_1$, $\boldsymbol{\eta}_1$ and $\boldsymbol{k}_2$, $\boldsymbol{\eta}_2$ denote shearing in crystallographically equivalent twin systems, see Fig. 2.2. Non-compound twins are hardly reported, and appear to occur only in low-symmetry lattices (see Fig. 2.3 for a type 2 twinning mode). Examples for the occurrence of non-compound twins are α-uranium (Cahn, 1953) and sapphire (Clayton, 2009).

In this work, a shear plane is identified by $\boldsymbol{n}$ $(\boldsymbol{k}_1)$, the shear direction by $\boldsymbol{d}$ $(\boldsymbol{\eta}_1)$ and the plane of shear by $\boldsymbol{k}$, where all vectors are normalised. Therefore, a shear number γ is needed to uniquely identify the twinning mode.

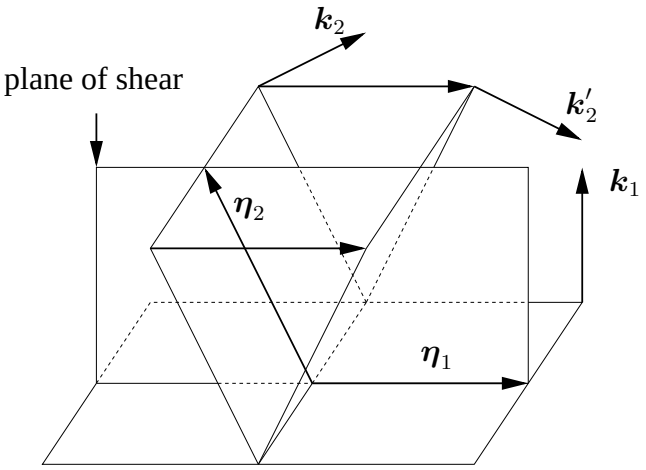

Figure 2.1: The commonly used twin elements.

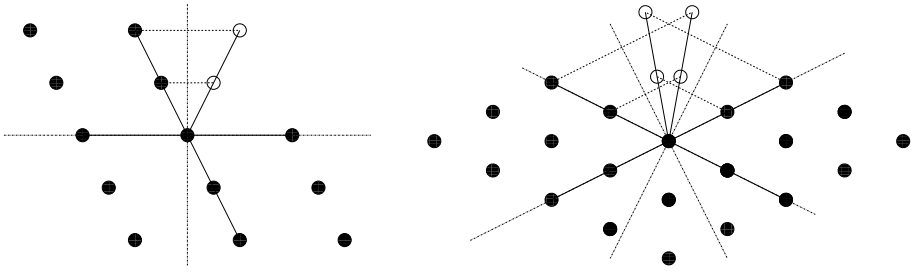

Figure 2.2: A compound twin (left), crystallographically equivalent compound twins (right).

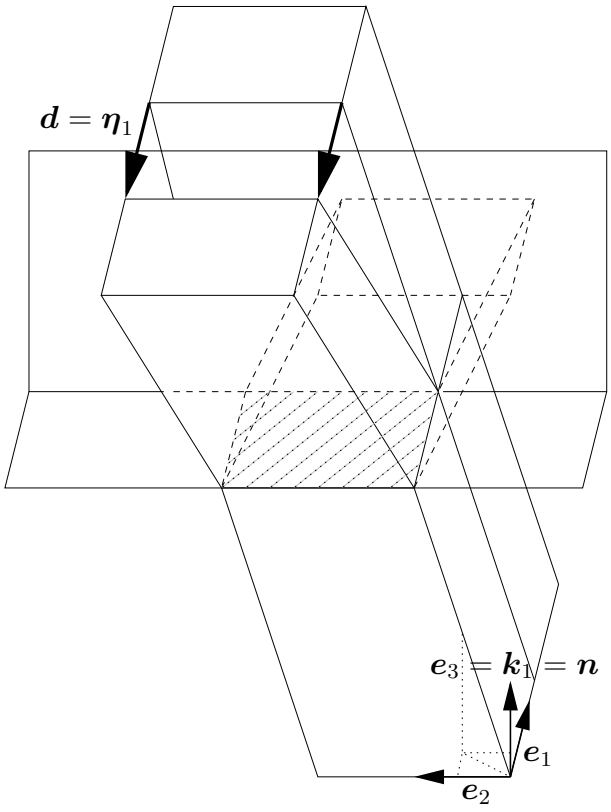

Figure 2.3: A type 2 twin in a triclinic unit cell. Shearing occurs in direction $\boldsymbol{d}$. The plane normal to $\boldsymbol{d}$ serves as a mirror plane, while the plane normal to $\boldsymbol{n}$ does not.

2.2 Mechanical Twinning in Simple Lattices

The variety of twinning modes and materials that undergo twinning is large. Practically all crystals can form twins (Cahn and Haasen, 1996) if crystallographic glide is disabled, e.g. at low temperatures. At room temperature, the most important materials for engineering applications which undergo twinning display a hexagonal close packed (hcp), a face centred cubic (fcc) or a body centred cubic (bcc) lattice. The most important hcp crystals are single phase Mg, Ti, Co, Zn, Be, Cd, Zr and their alloys, while the most interesting cubic crystals are intermetallic compounds, like fcc TiAl, bct NiMn and fcc FeMn, which exhibits the TWIP-effect. Furthermore, single phase fcc Cu owes its great ductility partially to deformation twinning. For magnesium, at least six different twinning modes have been reported (Reed-Hill and Robertson, 1957a; Klassen-Neklyudova, 1964), some of which are only active under very specific conditions.

Twinning is strongly connected to the crystallographic lattice. For a more general account to lattices see Pitteri and Zanzotto (2002). It is pointed out that the definition of a twin varies between different authors, each one choosing a definition meeting each ones purpose best. Here, the focus is on practicability for a continuum theory, and therefore in terms of deformations.

In a simple lattice, each lattice point can be reached by an integer linear combination of lattice base vectors $\boldsymbol{p}_i$. Then, $\boldsymbol{t}_i$ and $\boldsymbol{t}'_i$ are the lattice bases of a possible twin variant if

$$\boldsymbol{t}_i = \boldsymbol{F}\boldsymbol{p}_i, \quad \boldsymbol{F} \in Inv^+ \tag{2.1}$$

$$\boldsymbol{t}'_i = \boldsymbol{Q}\boldsymbol{p}_i, \quad \boldsymbol{Q} \in Orth^+ \tag{2.2}$$

$$\forall \alpha_i \in \mathbb{Z} \exists \alpha'_i \in \mathbb{Z}: \quad \alpha_i \boldsymbol{t}_i = \alpha'_i \boldsymbol{t}'_i. \tag{2.3}$$

are fulfilled. In words: Either a deformation or a rotation of the lattice basis $\boldsymbol{p}_i$ gives a lattice basis $\boldsymbol{t}_i$ or $\boldsymbol{t}'_i$, which both generate congruent simple lattices. Illustrative examples are given in Fig. 2.4. For convenience, $\boldsymbol{F}$ will be called the twin deformation, while $\boldsymbol{Q}$ is regarded as the reorientation.

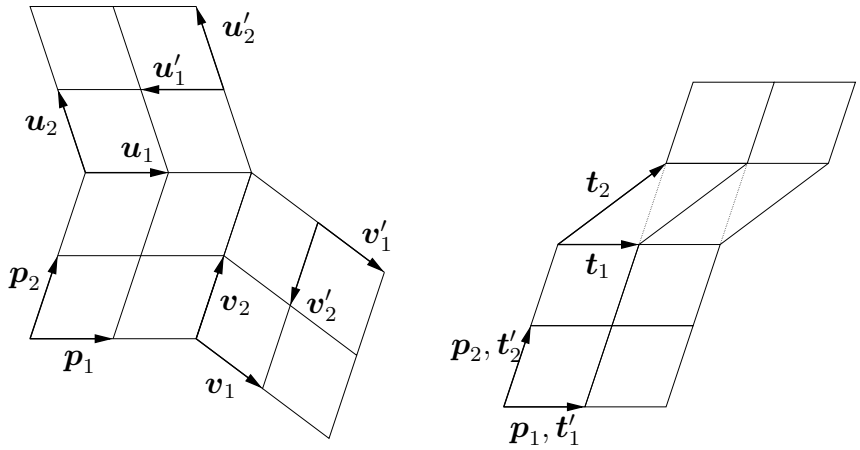

Figure 2.4: Left: Twinning along shear directions $\boldsymbol{p}_1$ and $\boldsymbol{p}_2$. The twin lattice bases $\boldsymbol{u}'_i$ and $\boldsymbol{v}'_i$ can be obtained by rotating the parent basis $\boldsymbol{p}_i$ 180° around the corresponding interface normal, while the twin lattice bases $\boldsymbol{u}_i$ and $\boldsymbol{v}_i$ are reached by shearing along the interface. Right: The lattice basis $\boldsymbol{t}_i$ generates a lattice congruent to the lattice generated by $\boldsymbol{t}'_i = \boldsymbol{I}\boldsymbol{p}_i$.

It is sufficient to focus on $\boldsymbol{Q}$ with $\det(\boldsymbol{Q}) = 1$, because the central inversion is included by expanding the three base vectors of $\boldsymbol{t}'_i$ and the corresponding α'_i with -1. The reader is encouraged to remember

that $\boldsymbol{t}_i$ comes from the deformation, while $\boldsymbol{t}'_i$ is given by rotating the parent basis, though this will be used frequently in the remainder of this Section.

Equations 2.1 to 2.3, which are basically the topic of this Section, are called "twinning condition" in the sense that potential twinning modes can be identified by searching for solutions of eq. 2.1 to 2.3, not to be confused with the loading conditions under which twinning occurs.

The set of possible twin deformations $\boldsymbol{F}$ can be reduced. We demand that a coherent interface between twin and parent exists. For simplicity, the parent lattice is taken as the undistorted reference configuration. Then, the kinematic compatibility condition imposes

$$\boldsymbol{F} = \boldsymbol{I} + \boldsymbol{a} \otimes \boldsymbol{n}, \tag{2.4}$$

with $\boldsymbol{n}$ being the interface normal (Liu, 2002). One can decompose $\boldsymbol{a}$ into its normal and tangential component with respect to $\boldsymbol{n}$, namely $\boldsymbol{a} = \gamma\boldsymbol{d} + \alpha\boldsymbol{n}$, $\boldsymbol{d} \cdot \boldsymbol{n} = 0$, and write

$$\boldsymbol{F} = \boldsymbol{I} + \gamma\boldsymbol{d} \otimes \boldsymbol{n} + \alpha\boldsymbol{n} \otimes \boldsymbol{n}. \tag{2.5}$$

Note that $\boldsymbol{n}$ and $\boldsymbol{d}$ are normalised. $\boldsymbol{F}$ represents a twinning mode if the lattice generated by $\boldsymbol{t}_i = \boldsymbol{F}\boldsymbol{p}_i$ can be obtained as well by rotating the parent basis. A necessary condition therefore is that the volumes of the unit cells are equal. The determinante of $\boldsymbol{F}$ is a measure for the volume change, and

$$\det(\boldsymbol{Q}) = \det(\boldsymbol{F}) = \det(\boldsymbol{I} + \gamma\boldsymbol{d}^* \otimes \boldsymbol{n} + \alpha\boldsymbol{n} \otimes \boldsymbol{n}) = 1 + \alpha = 1 \tag{2.6}$$

must be fulfilled. Therefore, α must be zero, and the twinning deformation must be a simple shear deformation $\boldsymbol{S} = \boldsymbol{I} + \gamma\boldsymbol{d} \otimes \boldsymbol{n}$, which already implicates that the interface is identical to the shear plane.

In order to fullfill eq. (2.3), it is sufficient to demand that the vectors $\boldsymbol{t}_i$ and $\boldsymbol{t}'_i$ can be represented by integer linear combinations of the other one, i.e., for $\alpha_i = 1$ and $\alpha'_i = 1$ one can write

$$\boldsymbol{t}_i = A_{ij}\boldsymbol{t}'_j, \tag{2.7}$$

$$\boldsymbol{t}'_i = A^{-1}_{ij}\boldsymbol{t}_j, \tag{2.8}$$

where $[A]$ is an invertible 3×3 matrix with integer components, the inverse of which contains only integers. In order to identify twinning modes for a simple lattice induced by a given basis $\boldsymbol{p}_i$, one has to search for $\boldsymbol{S}$, $\boldsymbol{Q}$ and $[A]$ such that

$$\begin{gathered}\boldsymbol{S}\boldsymbol{p}_i = A_{ij}\boldsymbol{Q}\boldsymbol{p}_j, \quad \boldsymbol{S} \in \mathit{Shear}, \quad \boldsymbol{Q} \in \mathit{Orth}^+ \\ [A] \in \mathit{Inv}, \quad A_{ij}, A^{-1}_{ij} \in \mathbb{Z}, \quad i,j = 1 \ldots 3\end{gathered} \tag{2.9}$$

is satisfied. This is not a trivial task. Moreover, the twinning condition (2.9) is too wide, because crystallographic slip in direction of $\boldsymbol{p}_i$ is included, as sketched in Fig. 2.4. A corresponding solution is

$$\boldsymbol{S} = \boldsymbol{I} + gV^{-1}\boldsymbol{p}_i \otimes (\boldsymbol{p}_i \times \boldsymbol{p}_j),\ V = \boldsymbol{p}_1 \cdot (\boldsymbol{p}_2 \times \boldsymbol{p}_3),\ i \neq j, \quad g \in \mathbb{Z}, \tag{2.10}$$

$$\boldsymbol{Q} = \boldsymbol{I} \tag{2.11}$$

with V being the volume of the unit cell. As one can check, the resultant $\boldsymbol{t}_k$ and $\boldsymbol{t}'_k$ for, e.g., $i = 1$ and $j = 2$ are

$$\boldsymbol{t}_1 = \boldsymbol{t}'_1 = \boldsymbol{p}_1, \tag{2.12}$$

$$\boldsymbol{t}_2 = \boldsymbol{t}'_2 = \boldsymbol{p}_2, \tag{2.13}$$

$$\boldsymbol{t}_3 = \boldsymbol{t}'_3 + g\boldsymbol{t}'_1 = \boldsymbol{p}_3 + g\boldsymbol{p}_1, \tag{2.14}$$

which clearly generate the same lattice, with

$$\boldsymbol{t}_i = A_{ij}\boldsymbol{t}'_j, \quad A_{ij} = \begin{bmatrix} 1 & 0 & 0 \\ 0 & 1 & 0 \\ g & 0 & 1 \end{bmatrix}. \tag{2.15}$$

Such lattice invariant shear deformations have been examined by Ericksen (1984a,b). They represent crystallographic glide along one of the lattice vectors, not by dislocation movement but by sliding along the entire shear plane. This is not of practical interest. Even if one is restricted to the so called "classical" twinning modes (Christian and Mahajan, 1995), which imposes further restrictions on $\boldsymbol{Q}$ and A_{ij}, lattice invariant shearing (slip) is still included, as shown later on.

In classical twinning, the twin lattice must be the mirror image of parent lattice on the interface plane or on the plane normal to the shear direction. Actually, there is no convincing experimental evidence for the occurrence of non-classical twins (Ericksen, 1991; Zanzotto, 1992; Christian and Mahajan, 1995). Therefore, the remainder is restricted to classical twinning. Following from the latter orientation relation, a twin lattice base can be obtained by
• mirroring the parent lattice at the interface/shear plane $\boldsymbol{n}$,
• mirroring the parent lattice at the plane normal to the shear direction $\boldsymbol{d}$,
• rotating the parent lattice 180° around the shear plane normal $\boldsymbol{n}$,
• rotating the parent lattice 180° around the shear direction $\boldsymbol{d}$ (Christian and Mahajan, 1995).
Due the restriciton $\det(\boldsymbol{Q}) = 1$ from above, in the remainder the rotations are the used orientation relations. Rotations around 180° can be represented by the special symmetric and orthogonal tensor $\boldsymbol{R} = -\boldsymbol{I} + 2\boldsymbol{a} \otimes \boldsymbol{a}$, with $\boldsymbol{a}$ being the normalised axial vector. The classical twinning then imposes

$$(\boldsymbol{I} + \gamma \boldsymbol{d} \otimes \boldsymbol{n})\boldsymbol{p}_i = A_{ij}\boldsymbol{R}\boldsymbol{p}_j, \tag{2.16}$$

$$\boldsymbol{p}_i = A_{ij}(\boldsymbol{I} + \gamma \boldsymbol{d} \otimes \boldsymbol{n})^{-1}\boldsymbol{R}\boldsymbol{p}_j, \tag{2.17}$$

$$\boldsymbol{p}_i = A_{ij}(\boldsymbol{I} - \gamma \boldsymbol{d} \otimes \boldsymbol{n})\boldsymbol{R}\boldsymbol{p}_j, \tag{2.18}$$

with $\boldsymbol{R_n} = -\boldsymbol{I} + 2\boldsymbol{n} \otimes \boldsymbol{n}$ or $\boldsymbol{R_d} = -\boldsymbol{I} + \boldsymbol{d} \otimes \boldsymbol{d}$. One speaks of type 1 twins in the first and type 2 twins in the second case. In both cases

$$(\boldsymbol{I} - \gamma \boldsymbol{d} \otimes \boldsymbol{n})\boldsymbol{R} = \boldsymbol{P} \tag{2.19}$$

yields a $\boldsymbol{P}$ that is self-inverse,

$$\boldsymbol{P} = \boldsymbol{P}^{-1}. \tag{2.20}$$

We may examine the difference between lattice bases that undergo type 1 and type 2 twinning by introducing the tensor $\boldsymbol{A}$ mapping the type 2 twinned basis on the type 1 twinned basis,

$$\boldsymbol{R}_1\boldsymbol{p}_i = \boldsymbol{A}\boldsymbol{R}_2\boldsymbol{p}_i. \tag{2.21}$$

$\boldsymbol{A}$ is easily evaluated,

$$\boldsymbol{A} = \boldsymbol{R}_1\boldsymbol{R}_2 = \boldsymbol{R_n}\boldsymbol{R_d} = \boldsymbol{R_k}. \tag{2.22}$$

Therefore, the distinction into type 1 and type 2 twins is not necessary if $\boldsymbol{R_k}$ is element of the symmetry group of the simple lattice induced by $\boldsymbol{p}$. The same has been found by Stark (1988). Such twins, for which both orientation relations hold, are named as compound twins, which are the

twinning modes of most practical relevance. The lattice symmetry of compound twins with respect to $\boldsymbol{R_k}$ is of importance when the strain energy invariance of conjugate twins is discussed (Section 4.8).

Eq. (2.20) can be used to restrict $[A]$ further by

$$\boldsymbol{p}_i = A_{ij}\boldsymbol{P}\boldsymbol{p}_j, \tag{2.23}$$

$$\boldsymbol{P}\boldsymbol{p}_i = A_{ij}\boldsymbol{p}_j, \tag{2.24}$$

which gives after renaming the indices $j \rightarrow k$ and $i \rightarrow j$ in eq. (2.24) and inserting into eq. (2.23)

$$\boldsymbol{p}_i = A_{ij}A_{jk}\boldsymbol{p}_k. \tag{2.25}$$

With $\boldsymbol{p}_i$ being a base of linear independent vectors, the latter equation is only fulfilled if

$$A_{ij}A_{jk} = \delta_{ik}, \qquad [A] = [A]^{-1}, \tag{2.26}$$

which shows that the self-inverseness of $\boldsymbol{P}$ is conducted to $[A]$. We therefore reformulate the twinning condition for type 1 twinning, putting the γ into $\boldsymbol{d}$ and taking $\boldsymbol{R} = -\boldsymbol{I}+2\boldsymbol{n}\otimes\boldsymbol{n}$ as orientation relation. $\boldsymbol{d}$ and $\boldsymbol{n}$ denote a possible twinning mode of a simple lattice generated by $\boldsymbol{p}_k$ if

$$\boldsymbol{n}\cdot\boldsymbol{n} = 1 \tag{2.27}$$

$$\boldsymbol{d}\cdot\boldsymbol{n} = 0 \tag{2.28}$$

$$\boldsymbol{P} = -\boldsymbol{I} - \boldsymbol{d}\otimes\boldsymbol{n} + 2\boldsymbol{n}\otimes\boldsymbol{n} \tag{2.29}$$

$$\boldsymbol{p}_i = A_{ij}\boldsymbol{P}\boldsymbol{p}_j, \qquad [A] = [A]^{-1}, \qquad A_{ij} \in \mathbb{Z},\ i,j = 1\ldots3 \tag{2.30}$$

are fulfilled. Similarly, the twinning conditions for type 2 twinning can be derived by taking $\boldsymbol{R_d}$ instead of $\boldsymbol{R_n}$. However, no qualitatively distinct results emerge, which is why it is focused on type 1 twinning in the remainder of this Section. $[A]$ is a self-inverse integer matrix, which is by definition *very nice* (Hanson, 1985). In the same article it is shown that every self-inverse integer matrix is equivalent to an upper triangular $m \times m$ matrix of the form

$$[M] = \begin{bmatrix} \delta_{ij} & x_{il} \\ 0 & -\delta_{kl} \end{bmatrix}, \quad i,j = 1\ldots n, \quad k,l = n+1\ldots m, \tag{2.31}$$

where the equivalence relation is

$$[A] = [P]^{-1}[M][P], \quad [P] \in Inv, (P_{ij}, P_{ij}^{-1}) \in \mathbb{Z},\ i,j = 1\ldots m. \tag{2.32}$$

$[P]$ is an integer invertible matrix, the inverse of which contains only integers, but does not need to be self-inverse (i.e. $[P]$ is only *nice*). A self-inverse integer matrix of the form (2.31) is called canonical. Hanson (1985) shows that every self-inverse integer $m \times m$ matrix is equivalent to only one canonical self-inverse integer matrix. This statement includes that two distinct canonical self-inverse integer matrices cannot be equivalent.

The reduced twinning condition still includes crystallographic slip. The example from above (eq. 2.10 and 2.11) can be slightly modified such that eq. 2.27 to 2.30 are satisfied. The shear deformation is unaffected, while $\boldsymbol{R}$ can be replaced by a rotation of 180° around the shear direction:

$$\boldsymbol{S} = \boldsymbol{I} + gV^{-1}\boldsymbol{p}_i \otimes (\boldsymbol{p}_i \times \boldsymbol{p}_j),\ V = \boldsymbol{p}_1 \cdot (\boldsymbol{p}_2 \times \boldsymbol{p}_3),\ i \neq j, \quad g \in \mathbb{Z}, \tag{2.33}$$

$$\boldsymbol{R} = -\boldsymbol{I} + \frac{2}{\boldsymbol{p}_i \cdot \boldsymbol{p}_i}\boldsymbol{p}_i \otimes \boldsymbol{p}_i, \tag{2.34}$$

$$\boldsymbol{P} = \boldsymbol{S}^{-1}\boldsymbol{R} \tag{2.35}$$

The evaluation for $i = 1$ and $j = 2$ gives

$$\boldsymbol{P} = -\boldsymbol{I} + gV^{-1}\boldsymbol{p}_1 \otimes (\boldsymbol{p}_1 \times \boldsymbol{p}_2) + \frac{2}{\boldsymbol{p}_1 \cdot \boldsymbol{p}_1}\boldsymbol{p}_1 \otimes \boldsymbol{p}_1, \tag{2.36}$$

and one finds

$$\boldsymbol{P}\boldsymbol{p}_1 = \boldsymbol{p}_1, \tag{2.37}$$

$$\boldsymbol{P}\boldsymbol{p}_2 = -\boldsymbol{p}_2 + \frac{2\boldsymbol{p}_1 \cdot \boldsymbol{p}_2}{\boldsymbol{p}_1 \cdot \boldsymbol{p}_1}\boldsymbol{p}_1, \tag{2.38}$$

$$\boldsymbol{P}\boldsymbol{p}_2 = -\boldsymbol{p}_3 + g\boldsymbol{p}_1 + \frac{2\boldsymbol{p}_1 \cdot \boldsymbol{p}_3}{\boldsymbol{p}_1 \cdot \boldsymbol{p}_1}\boldsymbol{p}_1. \tag{2.39}$$

The corresponding A-matrix is then

$$A = \begin{bmatrix} 1 & 0 & 0 \\ \frac{2\boldsymbol{p}_1 \cdot \boldsymbol{p}_2}{\boldsymbol{p}_1 \cdot \boldsymbol{p}_1} & -1 & 0 \\ \frac{2\boldsymbol{p}_1 \cdot \boldsymbol{p}_3}{\boldsymbol{p}_1 \cdot \boldsymbol{p}_1} + g & 0 & -1 \end{bmatrix}. \tag{2.40}$$

One can confirm that $[A] = [A]^{-1}$, and that $\boldsymbol{p}_i$ can be chosen such that $A_{ij} \in \mathbb{Z},\ i, j = 1 \ldots 3$ is met. The corresponding deformation and bases are depicted for an orthonormal basis $\boldsymbol{p}_i$ and $g = 1$ in Fig. 2.5a.

In the neighbouring figure, a common twinning mode found in the body centred tetragonal (bct) lattice (usually indexed as $\{101\}\langle 10\bar{1}\rangle$ with respect to the basis $(\boldsymbol{e}_1, \boldsymbol{e}_2, c\boldsymbol{e}_3)$) is depicted. The bct lattice can be generated by a rhombohedral basis, which base vectors point from one corner atom to three of the neighbouring body-centred atoms. The rhombohedral bct base and twin mode are given by

$$\boldsymbol{p}_1 = \frac{1}{2}(\boldsymbol{e}_1 + \boldsymbol{e}_2 + c\boldsymbol{e}_3), \tag{2.41}$$

$$\boldsymbol{p}_2 = \frac{1}{2}(-\boldsymbol{e}_1 + \boldsymbol{e}_2 + c\boldsymbol{e}_3), \tag{2.42}$$

$$\boldsymbol{p}_3 = \frac{1}{2}(-\boldsymbol{e}_1 - \boldsymbol{e}_2 + c\boldsymbol{e}_3), \tag{2.43}$$

$$\boldsymbol{n} = |\boldsymbol{p}_2 \times \boldsymbol{p}_3|^{-1}\boldsymbol{p}_2 \times \boldsymbol{p}_3 = (1 + c^2)^{-\frac{1}{2}}(c\boldsymbol{e}_1 + \boldsymbol{e}_3), \tag{2.44}$$

$$\boldsymbol{d} = -\gamma|\boldsymbol{p}_2 + \boldsymbol{p}_3|^{-1}(\boldsymbol{p}_2 + \boldsymbol{p}_3) = \gamma(1 + c^2)^{-\frac{1}{2}}(\boldsymbol{e}_1 - c\boldsymbol{e}_3), \quad \gamma = c - 1/c, \tag{2.45}$$

with c being the height of the unit cell divided by the edge length of the base square. It is particular interesting that $\boldsymbol{p}_2$ and $\boldsymbol{p}_3$ are unaffected by the twin deformation, though they span the shear plane. One could therefore suspect the deformation to represent crystallographic slip. As one can check, one obtains with $\boldsymbol{P} = -\boldsymbol{I} - \gamma\boldsymbol{d} \otimes \boldsymbol{n} + 2\boldsymbol{n} \otimes \boldsymbol{n}$

$$\boldsymbol{P}\boldsymbol{p}_1 = \frac{1}{2}(\boldsymbol{e}_1 - \boldsymbol{e}_2 + c\boldsymbol{e}_3) = \boldsymbol{p}_1 - \boldsymbol{p}_2 + \boldsymbol{p}_3, \tag{2.46}$$

$$\boldsymbol{P}\boldsymbol{p}_2 = \frac{1}{2}(\boldsymbol{e}_1 - \boldsymbol{e}_2 - c\boldsymbol{e}_3) = -\boldsymbol{p}_2, \tag{2.47}$$

$$\boldsymbol{P}\boldsymbol{p}_3 = \frac{1}{2}(\boldsymbol{e}_1 + \boldsymbol{e}_2 - c\boldsymbol{e}_3) = -\boldsymbol{p}_3, \tag{2.48}$$

with

$$\boldsymbol{P}\boldsymbol{p}_i = A_{ij}\boldsymbol{p}_j, \quad [A_{ij}] = \begin{bmatrix} 1 & -1 & 1 \\ 0 & -1 & 0 \\ 0 & 0 & -1 \end{bmatrix}, \tag{2.49}$$

being a self-inverse integer matrix that is already of the canonical form (2.31). One may choose

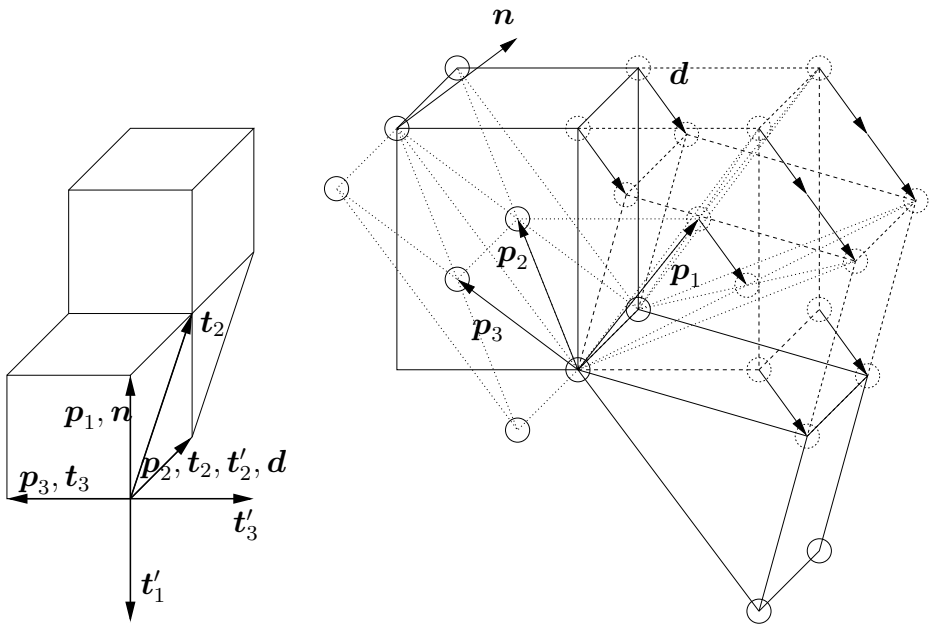

Figure 2.5: (a) Crystallographic slip fulfilling the twinning relations for type 1 twins in the primitive cubic lattice. (b) A common twinning mode in a bct lattice.

another basis that generates the same bct lattice, for example

$$\boldsymbol{p}_1 = \boldsymbol{e}_1 \tag{2.50}$$

$$\boldsymbol{p}_2 = \boldsymbol{e}_2 \tag{2.51}$$

$$\boldsymbol{p}_3 = \frac{1}{2}\boldsymbol{e}_1 + \frac{1}{2}\boldsymbol{e}_2 + \frac{c}{2}\boldsymbol{e}_3 \tag{2.52}$$

For the same twinning mode, one finds

$$\boldsymbol{P}\boldsymbol{p}_1 = c\boldsymbol{e}_3 = 2\boldsymbol{p}_3 - \boldsymbol{p}_1 - \boldsymbol{p}_2 \tag{2.53}$$

$$\boldsymbol{P}\boldsymbol{p}_2 = -\boldsymbol{e}_2 = -\boldsymbol{p}_2 \tag{2.54}$$

$$\boldsymbol{P}\boldsymbol{p}_3 = \frac{1}{2}\boldsymbol{e}_1 - \frac{1}{2}\boldsymbol{e}_2 + \frac{c}{2}\boldsymbol{e}_3 = \boldsymbol{p}_3 - \boldsymbol{p}_2, \tag{2.55}$$

with the corresponding very nice matrix

$$[A_{ij}] = \begin{bmatrix} -1 & -1 & 2 \\ 0 & -1 & 0 \\ 0 & -1 & 1 \end{bmatrix}. \tag{2.56}$$

By elementary matrix operations for self-inverse integer matrices presented by Hanson (1985) one can reduce $[A_{ij}]$ to its canonical form. It is interesting to note that one does not find the matrix in eq.

(2.49), although the same twinning mode in the same lattice has been described, but with different generating lattice bases. The elementary operations that yield equivalent self-inverse integer matrices are:
• Add k ($k \in \mathbb{Z}$) times row i to row j. Then, add $-k$ times column j to column i.
• Interchange row i and row j. Then, interchange column i with column j.
• Multiply row i by -1 and then multiply column i by -1.
Further, the transpose of a self-inverse matrix remains a self-inverse matrix. By carrying out the first operation with $k = -1$, $i = 3$ and $j = 1$ and the second with $i = 1$ and $j = 3$ one finds the corresponding canonical self-inverse matrix

$$[A_{ij}]_{\text{can.}} = \begin{bmatrix} 1 & -1 & 0 \\ 0 & -1 & 0 \\ 0 & 0 & -1 \end{bmatrix}, \tag{2.57}$$

which differs from the one given in eq. (2.49). Further, taking the transpose of the self-inverse matrix of eq. (2.40) and choosing $\boldsymbol{p}_i$ and g accordingly yields the self-inverse matrix of eq. (2.49). One comes from a solution representing crystallographic glide, the other from a twinning mode. In other words: the self-inverse integer matrix in the twinning condition does not serve for distinguishing whether a solution represents twinning or crystallographic glide, neither does it help to uniquely identify a twinning mode. This holds at least until a unique reduced basis to any simple lattice is defined and used, though the different $[A]$ matrices arise when the same lattice is described by different bases.

The twinning conditions (2.27)-(2.30) still include crystallographic glide, as the example above demonstrates. The main feature of gliding is that the lattice is not reoriented. In the notation used here, $\boldsymbol{p}_i$ and $\boldsymbol{t}'_i = \boldsymbol{R}\boldsymbol{p}_i$ generate the same simple lattice. This is identical to stating that if $\boldsymbol{R}$ is element of the symmetry group of $\boldsymbol{p}_i$, the corresponding solution of eq. (2.27)-(2.30) represents crystallographic slip. For this reason, in the cubic lattices the $\{100\}$ and $\{110\}$ planes do not serve for type 1 twinning, which is due to the fact that rotations of 180° around these directions are elements of the crystal symmetry group. One can search for solutions of eq. (2.27)-(2.30), and check afterwards whether $\boldsymbol{R}$ is element of the symmetry group of $\boldsymbol{p}_i$.

Until here, the twins discussed are produced by shearing the simple lattice generated by $\boldsymbol{p}_i$. However, twinning is not restricted to these modes. It may also happen that the twinning conditions hold only for a sublattice, see Fig. 2.6. In that case, the atoms not captured by the sublattice have to undergo a so called shuffling, because the simple shear deformation does not leave them in their new lattice positions. Shuffling is the nonhomogeneous but periodic movement of atoms not captured by the simple lattice that undergoes twinning, see Figs. 2.6 and 2.7 for illustrations. As pointed out by Christian and Mahajan (1995), twinning modes including shuffling are of practical relevance. In Fig. 2.7, several realizations of a $\{013\}$ twin in a simple cubic lattice (Hirth, 2000) are depicted, involving pure shear, pure shuffling and a mixture of both. The pure shuffling examples are not of practical interest, because the question which driving force triggers a sudden shuffling without a mean deformation and without a change of crystal class cannot be answered conclusively. Most twinning modes that are of practical interest are realized by a simple shear deformation plus shuffling, as depicted in the lower left subfigure of Fig. 2.7.

There has been made some effort to predict possible twinning modes by Bilby and Crocker (1965), based on the assumption that the twinning modes with small shear numbers and a minimum of shuffling are preferred. It is clear that one can search for a very large sublattice which can form a twin

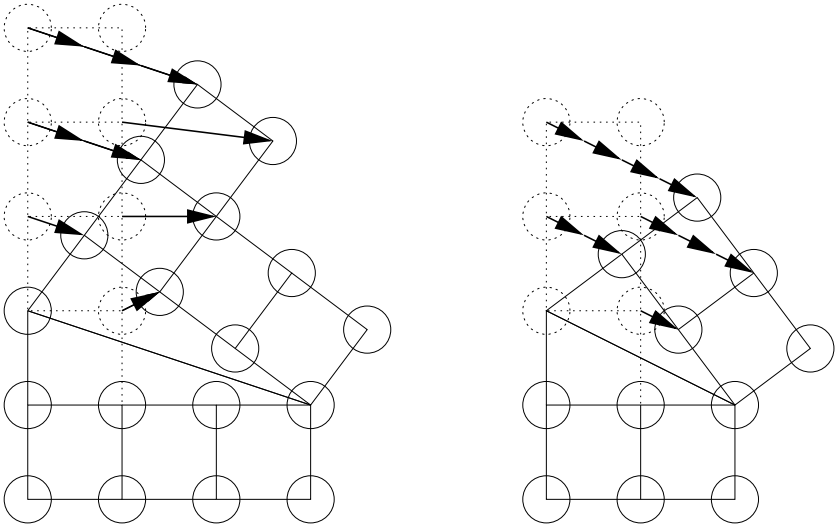

Figure 2.6: Left: Twinning mode involving shuffling, right: shuffle-free twinning.

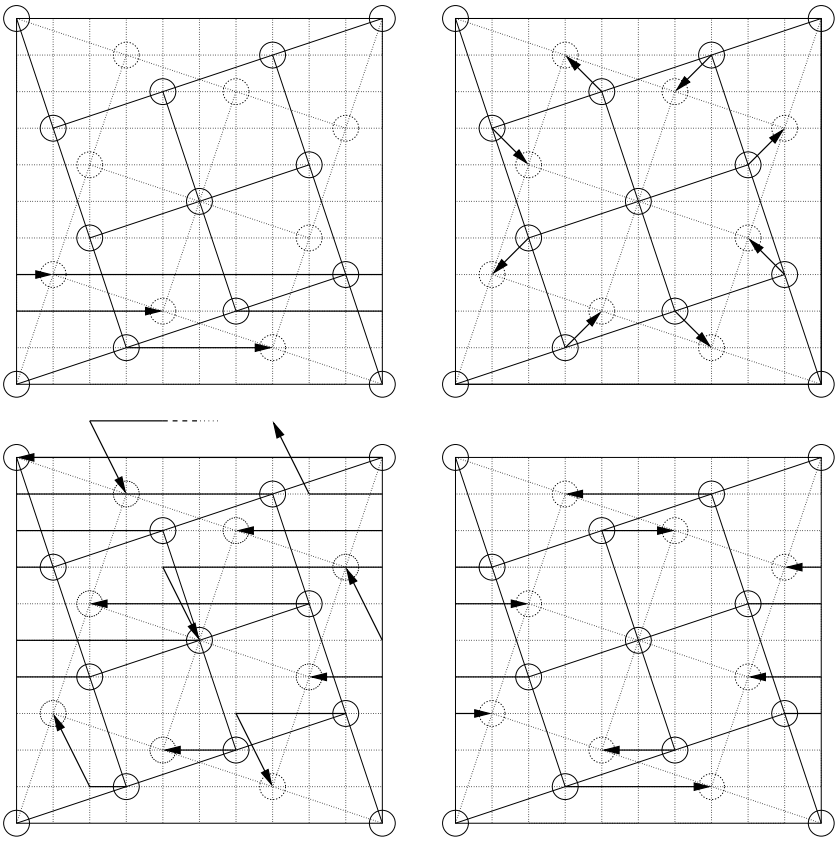

Figure 2.7: $\{013\}$ twinning in a simple cubic lattice. Note that shuffling does not need to occur parallel to the plane of shear. Upper left: pure simple shear deformation with $\gamma_0 = 4$. Upper right: pure shuffling. Lower left: simple shear deformation with $\gamma_0 = 1$ plus shuffling of 50% of the atoms. Lower right: pure shuffling parallel to the twin parent interface.

with a very small shear number, which would give a supposed easily activated twin systems. As countermove, growing with the size of the sublattice-basis, more shuffling is necessary. As well, the twin thickness is a multitude of the size of the sublattice basis, which makes an arrangement of more thicker unit twins more difficult. See Westlake (1966); Thornton (1966) for a discussion on shuffling and unit twin thickness.

However, by solely looking at perfect lattices, it is ignored that twin propagation is connected to dislocation movement and stacking faults, which will be discussed later on. Therefore, it is practically impossible to predict relevant twinning modes by solely looking at the lattice basis.

2.3 The Hexagonal Lattice

For a hexagonal lattice, it is convenient to use the Miller-Bravais basis

$$\boldsymbol{a}_1 = a\boldsymbol{e}_1, \tag{2.58}$$

$$\boldsymbol{a}_2 = -\frac{a}{2}\boldsymbol{e}_1 + \frac{a\sqrt{3}}{2}\boldsymbol{e}_2, \tag{2.59}$$

$$\boldsymbol{a}_3 = -\frac{a}{2}\boldsymbol{e}_1 - \frac{a\sqrt{3}}{2}\boldsymbol{e}_2, \tag{2.60}$$

$$\boldsymbol{c} = c\boldsymbol{e}_3. \tag{2.61}$$

This basis is widely used in the literature (see Fig. 2.8, Neumann (1966); Pitteri and Zanzotto (2002)). The lattice parameters c and a represent the height of the cell and the edge length of the base hexagon, respectively, and correspond to the norms of $\boldsymbol{c}$ and $\boldsymbol{a}$, $c = \sqrt{\boldsymbol{c}\cdot\boldsymbol{c}}$ and $a = \sqrt{\boldsymbol{a}\cdot\boldsymbol{a}}$. Although one usually does not appreciate the use of linearly dependent base vectors, this basis has the advantage that it reflects the hexagonal symmetry. Permutations of the components belonging to $\boldsymbol{a}_{1\ldots3}$, a change of sign of the c-component or a change of sign simultaneous on all $a_{1\ldots3}$ yield crystallographically equivalent directions, which are denoted as $\langle a_1 a_2 a_3 c\rangle$. Usually, negative components are denoted by $\bar{x}$ instead of $-x$. Further, due to the linear dependence of $\boldsymbol{a}_{1\ldots3}$, the condition $a_1 + a_2 + a_3 = 0$ is imposed, and therefore sometimes the third component a_3 is omitted.
To indicate planes, it is advantageous to introduce another basis. This is done by taking the dual basis $(\tilde{\boldsymbol{a}}_1, \tilde{\boldsymbol{a}}_2, \tilde{\boldsymbol{c}})$ of $(\boldsymbol{a}_1, \boldsymbol{a}_2, \boldsymbol{c})$ and defining the base vectors

$$\boldsymbol{a}_1^* = \frac{2}{3}\tilde{\boldsymbol{a}}_1 - \frac{1}{3}\tilde{\boldsymbol{a}}_2 = \frac{2}{3a}\boldsymbol{a}_1, \tag{2.62}$$

$$\boldsymbol{a}_2^* = -\frac{1}{3}\tilde{\boldsymbol{a}}_1 + \frac{2}{3}\tilde{\boldsymbol{a}}_2 = \frac{2}{3a^2}\boldsymbol{a}_2, \tag{2.63}$$

$$\boldsymbol{a}_3^* = -\frac{1}{3}\tilde{\boldsymbol{a}}_1 - \frac{1}{3}\tilde{\boldsymbol{a}}_2 = \frac{2}{3a^2}\boldsymbol{a}_3, \tag{2.64}$$

$$\boldsymbol{c}^* = \tilde{\boldsymbol{c}} = \frac{1}{c^2}\boldsymbol{c}. \tag{2.65}$$

This basis again satisfies $\boldsymbol{a}_1^* + \boldsymbol{a}_2^* + \boldsymbol{a}_3^* = 0$, but it is not the dual basis of $(\boldsymbol{a}_1, \boldsymbol{a}_2, \boldsymbol{a}_3, \boldsymbol{c})$. It also has the advantage that crystallographically equivalent planes are connected by permutations of the components and changes of sign as stated above. Again, the components should be restricted to $a_1^* + a_2^* + a_3^* = 0$. If this is done, several practical simplifications are obtained: If a normal vector

is given with respect to the basis $(\boldsymbol{a}_1^*, \boldsymbol{a}_2^*, \boldsymbol{a}_3^*, \boldsymbol{c}^*)$, the reciprocals of its components correspond to the piercing point distances of the plane with the base vectors $(\boldsymbol{a}_1, \boldsymbol{a}_2, \boldsymbol{a}_3, \boldsymbol{c})$. Therefore, the plane $\{10\bar{1}2\}$ can be visualised by considering the points $\boldsymbol{a}_1$, $-\boldsymbol{a}_3$ and $1/2\boldsymbol{c}$ (see Fig. 2.8). Moreover, one can easily see whether direction and normal vectors are perpendicular to each other by calculating the scalar product as if $(\boldsymbol{a}_1, \boldsymbol{a}_2, \boldsymbol{a}_3, \boldsymbol{c})$ and $(\boldsymbol{a}_1^*, \boldsymbol{a}_2^*, \boldsymbol{a}_3^*, \boldsymbol{c}^*)$ were dual bases. One notes easily that $\langle 10\bar{1}1\rangle$ and $\{\bar{1}012\}$ are perpendicular to each other:

$$(\boldsymbol{a}_1 - \boldsymbol{a}_3 + \boldsymbol{c}) \cdot (-\boldsymbol{a}_1^* + \boldsymbol{a}_3^* + 2\boldsymbol{c}^*) = -\boldsymbol{a}_1 \cdot \boldsymbol{a}_1^* + \boldsymbol{a}_1 \cdot \boldsymbol{a}_3^* - \boldsymbol{a}_3 \cdot \boldsymbol{a}_3^* + \boldsymbol{a}_3 \cdot \boldsymbol{a}_1^* + 2\boldsymbol{c} \cdot \boldsymbol{c}^* \tag{2.66}$$

$$= -\frac{2}{3} - \frac{1}{3} - \frac{2}{3} - \frac{1}{3} + 2 = -1 - 1 + 2 = 0. \tag{2.67}$$

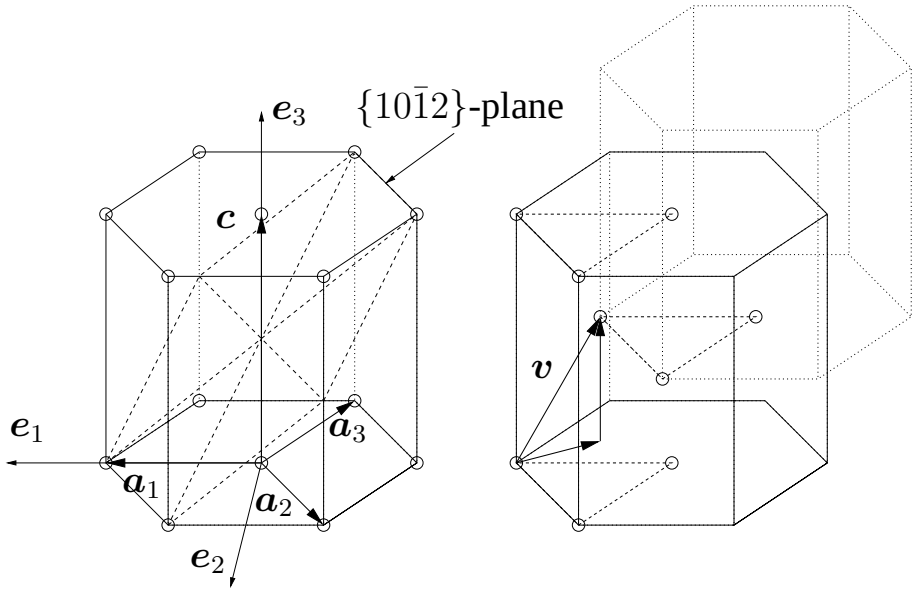

Figure 2.8: Simple hexagonal lattice with Miller-Bravais basis (left), hexagonal close packed multilattice constructed from the simple lattice by introducing additional translations in $\boldsymbol{v} = \langle \frac{\bar{1}}{3} 0 \frac{1}{3} \frac{1}{2} \rangle$ (right).

2.4 Partial Dislocations and Stacking Faults

A perfect crystal can be constructed by a pile of atomic layers, which have to be stacked in the proper sequence in order to construct a defect-free crystal; see Fig. 2.9 for an illustrative example with an abstract ABCABCABC stacking. A stacking fault is an error in the stacking. For example, in the Fig. 2.9, along line L the stacking is ABCACBABC, the layers B and C are interchanged. This stacking fault is enclosed by the two encircled partial dislocations, which would be line defects if the 2D sketch was considered as a cutting plane of a 3D-crystal. The term "partial dislocation" indicates that a finite stacking fault is limited by a pair of such dislocations. Partial dislocations at interfaces are sometimes referred to as twinning dislocations, Shockley dislocations, disconnections, transformation dislocations, structural ledges or growth ledges (Hirth, 2000). An illustrative explanation on the dissociation of ordinary dislocations into partial dislocations can be found in Reed-Hill and Abbaschian (1994).

In the given example, the partial dislocations enclose a twin lamella. As one can check, the lattice vectors $\boldsymbol{t}_1$ and $\boldsymbol{t}_2'$ in the lamella can be obtained by rotating the basis $\boldsymbol{p}_i$ around the vertical axis. An

alternative basis for the twin lamella consisting of the vectors $\boldsymbol{t}_1$ and $\boldsymbol{t}_2$ can be obtained from $\boldsymbol{p}_i$ by applying a simple shear deformation, with $\boldsymbol{p}_2$ as the shear direction and the vertical axis as the shear plane normal.

Stacking faults rise the level of the stored energy, especially the elastic strain energy by distorting the lattice. This energy is called stacking fault energy, the level of which depends on the crystal. Materials with a low stacking fault energy form more readily stacking faults than materials with a high stacking fault energy. Regarding a twin lamella as a stacking fault, it is concluded that materials with lower stacking fault energy are more inclined to form twins. A twin can be regarded as a pile of stacking faults (Boyko et al., 1994), see Fig. 2.10. Note that for stacking faults it is convenient to form neighbours, as the stored energy of the rejoined double layer stacking fault is reduced by eliminating two interfaces. The resulting twin nucleus is therefore more stable than the individual stacking faults, which renders the agglomeration of stacking faults to twin nuclei capable to reduce the internal energy of a crystal.

At this point, the interested reader is referred to the literature on dislocations in general (Reed-Hill and Abbaschian, 1994) and partial dislocations connected to twinning in special (Boyko et al., 1994). It is emphasised that the aforementioned is only a brief introduction, sketching the idea of how partial dislocations and stacking faults are connected to twinning.

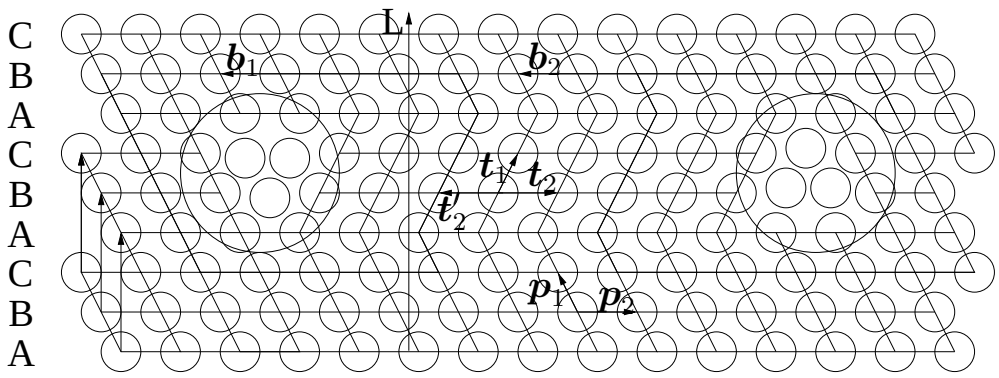

Figure 2.9: A stacking fault, enclosed by two partial dislocations.

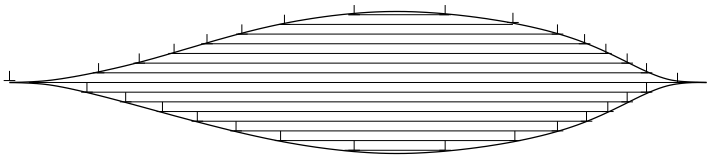

Figure 2.10: A twin can be considered as a pile of stacking faults.

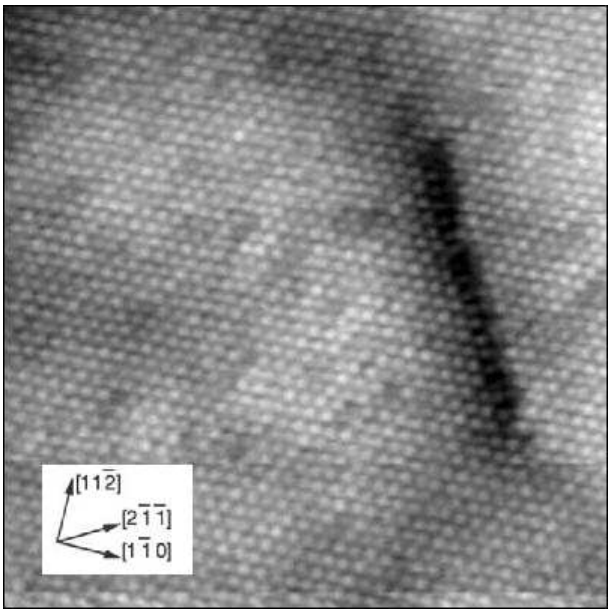

Figure 2.11: Scanning Tunnelling Microscope (STM) image of a stacking fault in a sputtered and annealed $\mathrm{Pt}_{25}\mathrm{Ni}_{75}$ single crystal, enclosed by two Shockley partial dislocations (courtesy of Schmid et al. (1992)).

2.5 Stacking of the HCP and the FCC Lattice

The hcp and the fcc crystal lattice can be constructed by regular stackings of planes of regularly densely packed spheres. By translating the base plane labeled A one obtains the variants B and C (see Fig. 2.12). By stacking ABAB... one obtains the hcp lattice, while ABCABC... results in the fcc lattice (Fig. 2.13, see, e.g., Pitteri and Zanzotto (2002)). Both lattices differ only by a parallel shift of planes, which facilitates the mechanical induced fcc to hcp transformation that is important for the TRIP effect (transformation induced plasticity). In the hcp case the stacking direction coincides with the cylinder axis of the unit cell, while in the fcc case the same unit cell can be obtained by stacking along the 4 distinct body diagonals $\langle 111 \rangle$. Following Kepler's conjecture, which can be regarded as proved (Hales, 2006), in both cases the stacking is as dense as possible, with $V_{\mathrm{Sphere}}/V_{\mathrm{total}} = \pi/(3\sqrt{2}) \approx 74\%$. However, real hexagonal crystals are not stacked ideally, resulting in a c/a ratio deviating from the ideally packed case with $c/a = \sqrt{8/3}$. This value is obtained by geometrical considerations on the regular tetrahedron. Note that the denomination "hexagonal closest packing" implies $c/a = \sqrt{8/3}$, while "hexagonal close packing" allows other c/a-ratios.

If $c/a = \sqrt{3}$, the $\{\bar{1}012\}\langle\bar{1}011\rangle$ twinning mode is not available (Fig. 2.14). In that case $\boldsymbol{k}_1$ and $\boldsymbol{k}_2$ are perpendicular to each other, and $\boldsymbol{k}_2$ and $\boldsymbol{k}_2'$ coincide, i.e. there is no shear deformation. If $c/a \neq \sqrt{3}$ one obtains from geometrical considerations the twinning shear to be

$$\gamma_0 = \frac{\sqrt{3}}{c/a} - \frac{c/a}{\sqrt{3}}. \tag{2.68}$$

The six possible shear directions are given by permutations of $\langle\bar{1}011\rangle$, where the $\boldsymbol{c}$-component has to be +1 due to the fact that a reversal of the shear direction by changing from $c/a < \sqrt{3}$ to $c/a > \sqrt{3}$ is implied in eq. 2.68.

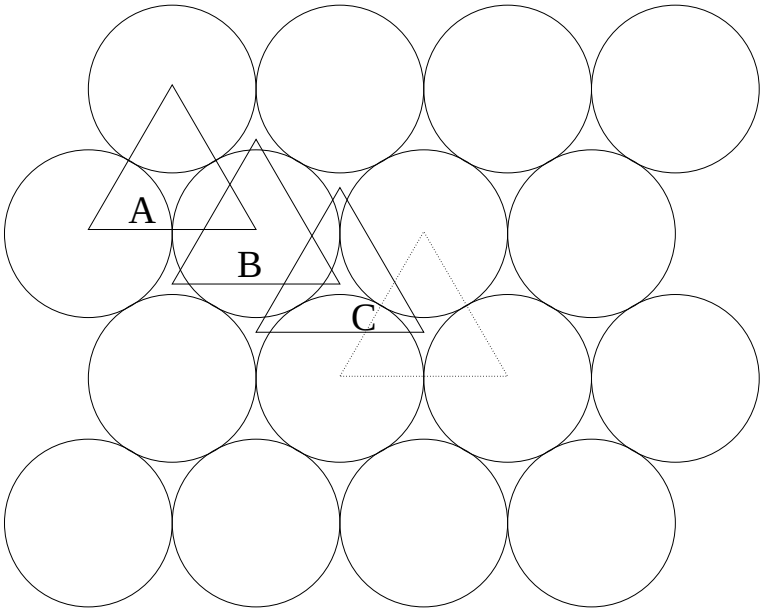

Figure 2.12: Densely packed spheres in 2D. By translating the plane A the variants B and C are obtained.

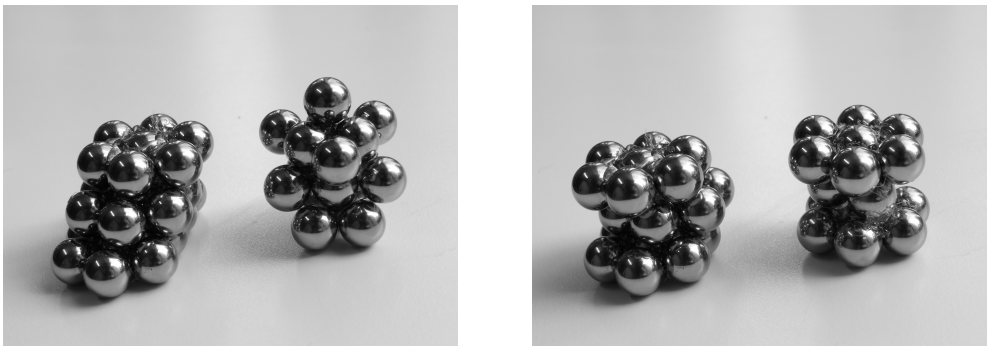

Figure 2.13: Stacking of fcc (left) and hcp (right) lattice. Note how the spheres form straight lines in the left figure, which are the face-diagonals in the fcc lattice.

2.6 Twinning in Magnesium

Twinning in magnesium has been studied in detail firstly by Reed-Hill and Robertson (1957a,b); Partridge (1965); Roberts and Partridge (1966); Wonsiewicz and Backofen (1967); Kelley and Hosford (1968). Since these pioneering works, a large amount of literature concerning twinning in magnesium and its alloys has been published. Usually, the twins are categorised as extension or compression twins, depending on wether they appear under elongation or compression along the $\boldsymbol{c}$-axis. Magnesium has $c \approx 0.52103$nm and $a \approx 0.32094$nm, which gives $c/a \approx 1.62345$, i.e. it is quiet close to the densest possible packing with $c/a = \sqrt{8/3}$. The unit cell is slightly less high than thick. This causes the $\{\bar{1}012\}\langle\bar{1}011\rangle$ twins to be extension twins (see Fig. 2.14), while twinning along the $\{10\bar{1}1\}$, $\{10\bar{1}3\}$, $\{30\bar{3}4\}$ and $\{10\bar{1}5\}$ planes (Meng et al., 2008) occurs under $\boldsymbol{c}$-axis compression. Recently, Stanford (2008) observed $\{11\bar{2}1\}$-twinning in the magnesium alloy WE54. The exact determination of the twinning mode is not an easy task, because precise measurements of lattice and interface orientations are necessary. Usually, the shear plane $\boldsymbol{n}$ is measured, and $\boldsymbol{d}$ is constrained by $\boldsymbol{n} \cdot \boldsymbol{d} = 0$. However, still more than one combination of twinning shear and atomic shuffling are possible. Though the shear is hard to measure in thin lamellae, it has been determined mostly by "ingenious geometric guesswork" (Zanzotto, 1992). For example, the $\{10\bar{1}1\}$ twinning mode in magnesium reported by Hall (1954) had to be corrected due to experimental findings by Reed-Hill (1960).

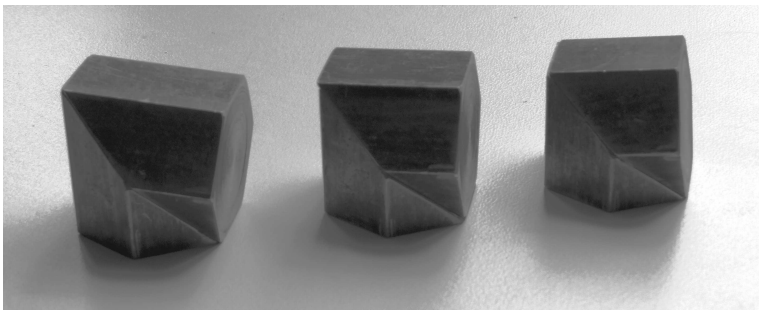

Figure 2.14: Visualisation of the effect of a variation of the c/a ratio on the magnitude of the shear deformation accompanying $\{10\bar{1}2\}$ twinning. Left: $c/a > \sqrt{3}$, twinning shear increases width of the entity, leading to $\boldsymbol{c}$-axis compression. Centre: $c/a = \sqrt{3}$, width and height do not change (the mean deformation is zero, no $\{10\bar{1}2\}$ twinning). Right: $c/a < \sqrt{3}$, twinning shear increases the height of the entity, leading to $\boldsymbol{c}$-axis elongation.

In a recent work (Al-Samman and Gottstein, 2008), plane strain compression tests on cuboid-shaped AZ31 samples with different processing histories are carried out. One of them is an extruded sample, that is compressed along the extrusion direction (Fig. 2.15). Extruded magnesium is textured such that the $\boldsymbol{c}$-axes and one of the $\boldsymbol{a}_i$ directions are distributed approximately uniformly and perpendicular around the extrusion direction, i.e. a compression along the extrusion direction results in a $\boldsymbol{c}$-axis elongation and vice versa. In a compression test, the strongly textured material undergoes a complete shift of texture, see Fig. 2.16. However, the impressive change of texture does not occur when the loading direction is reversed. As well, one observes a pronounced strength differential effect. The cause for this is the unidirectionality of twinning. The $\boldsymbol{c}$-axis elongation is accommodated by $\{\bar{1}012\}$ twins, while compression twins (mostly $\{\bar{1}011\}$) accommodate $\boldsymbol{c}$-axis compression, i.e. elongation along the extrusion direction. The twinning modes exhibit strong morphological differences. The $\{\bar{1}012\}$ tension twins are activated very easily, (namely at a shear stress of approximately 2.7MPa in

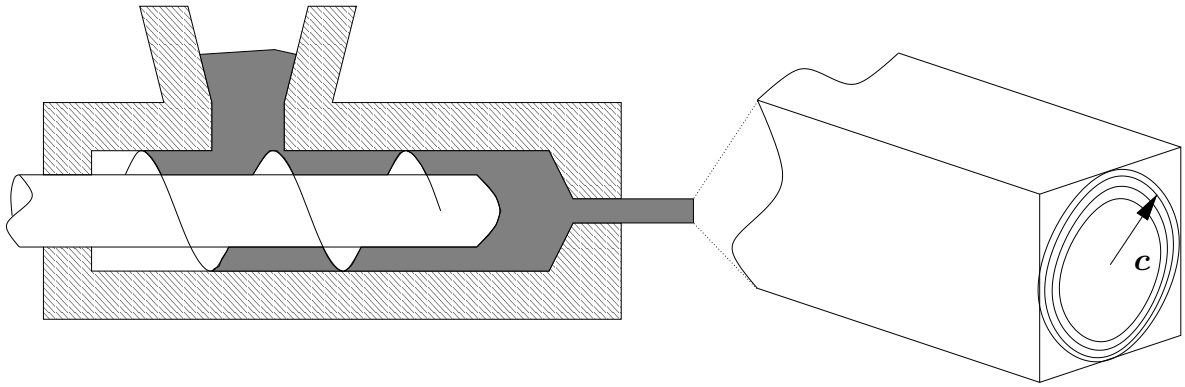

Figure 2.15: Schematic diagram of the extrusion process and the resulting texture.

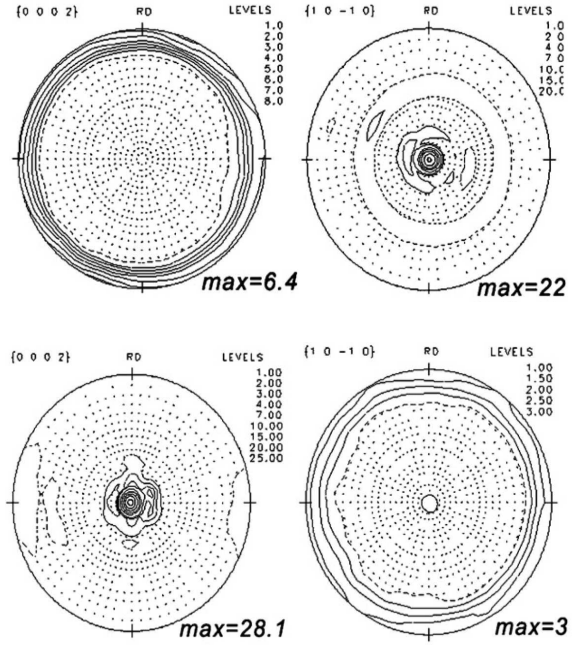

Figure 2.16: (0002) (left) and $(10\bar{1}0)$ (right) pole figures before (above) and after (below) the compression test at $\varepsilon = 0.28$ (courtesy of Al-Samman and Gottstein (2008)). The projection direction is parallel to the extrusion direction. As $\{10\bar{1}2\}$ twinning reorients the $\boldsymbol{c}$-axis about approximately 86°, the outer ring (upper left figure) transforms into the centre peek (lower left figure). The slight deviation from the approximately rotational symmetric starting texture comes from the asymmetry of the loading (plane strain compression, two opposing faces are kept fixed).

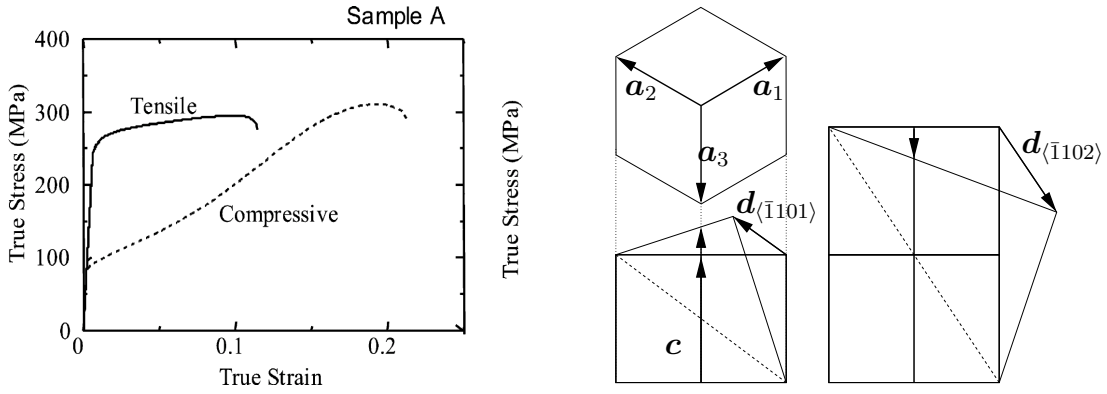

Figure 2.17: Strength differential effect in the AZ31 magnesium alloy (left, courtesy of Chino et al. (2008)), sketch of $\langle\bar{1}101\rangle\{1\bar{1}02\}$ extension and $\langle\bar{1}102\rangle\{1\bar{1}01\}$ compression twinning (right). The extension twins appear in an compression test along the extrusion direction and vice versa.

pure magnesium, Koike (2005)), and their boundaries are mobile. The $\{\bar{1}011\}$ compression twins are thin, pinned lamellae. Instead of growing in thickness like the elongation twins, double twinning (first $\{10\bar{1}1\}$ compression followed by $\{10\bar{1}2\}$ extension twins) is observed as loading continues (Yi et al., 2009).

Therefore, in a compression test, the major deformation mechanism are the $\{\bar{1}012\}$ elongation twins. After virtually occupying the entire volume, elongation twinning is no more disposable. Due to the reorientation of the $\boldsymbol{c}$-axis of approximately 86°, the deformation is then accommodated by $\{\bar{1}011\}$ compression twinning (Wonsiewicz and Backofen, 1967; Kelley and Hosford, 1968), as it occurs from the beginning if the contrary loading direction is chosen. As depicted in Fig. 2.17, the stress level is then approximately the same as in the tension test. Due to the immobile interfaces of the compression twins, the deformation accommodated before fracture is much lesser than in case of elongation twinning. The double twins have been identified to be crack initiation sites (Hartt and Reed-Hill, 1968; Yin et al., 2008).

Sumarising roughly, $\{\bar{1}012\}$ tension twins allow for large deformation accommodation, while $\{\bar{1}011\}$ compression twins preceed fracture. A similar behaviour is observed in titanium (Serra and Bacon, 1996; Ungár et al., 2008) and zinc (Lay and Nouet, 1994), which suggests that the morphological difference between the twinning modes is intrinsic to the hexagonal lattice structure. It is explained by the characteristics of the distinct interfaces and partial dislocations belonging to each twinning mode. In a series of articles, Serra and Bacon (1986, 1991, 1996) analysed twinning by the molecular dynamics technique. Firstly, they examined which of the different many-body potentials given in the literature suite best to each hcp metal (Bacon and Liang, 1986). Igarashi et al. (1991) even adapted parameters of the many-body potentials such that they reproduce the elastic properties and c/a ratio for eight hcp metals. With the potentials at hand, stacking fault and interface energies have been calculated, and found to be in agreement with experiments (Serra and Bacon, 1986). In Serra and Bacon (1991), the mobility of partial dislocations belonging to different twin interfaces has been studied by means of molecular dynamics. It is found that dislocations in $\{10\bar{1}2\}$ and $\{11\bar{2}1\}$ boundaries are very glissile, but sessile in $\{10\bar{1}1\}$ and $\{11\bar{2}2\}$ interfaces. In Serra and Bacon (1996), the interaction between basal slip dislocations and different twin interfaces has been studied. It is found that if a basal slip dislocation hits a $\{10\bar{1}2\}$ interface, a source for $\{10\bar{1}2\}$ partial dislocations is created, which forms pairs of partial dislocations if a shear strain of approximately ± 0.005 is applied. The

source therefore provides a mechanism to move the interface gradually by generating a pair of partial dislocations, as long as the load is not removed and no obstacle is met. The converse is reported for a basal slip dislocation that hits a $\{10\bar{1}1\}$ interface. It creates there a pair of partial dislocations, but not an independent source for twinning dislocations. Together with the findings from Serra and Bacon (1991), a convincing explanation for $\{10\bar{1}2\}$-twinning being the most prominent twinning mode in hcp metals is obtained.

Another explanation for the needle-like $\{10\bar{1}1\}$ twinning and the extensive $\{10\bar{1}2\}$ twinning is that the $\{10\bar{1}1\}$ twins produce a larger shear strain. Therefore, to accommodate a certain deformation, compared to $\{10\bar{1}2\}$ twinning, less volume fraction of $\{10\bar{1}1\}$ twins is necessary (Bingert et al., 2002; Jiang et al., 2007). At least for magnesium this explanation is rather improbable, as the corresponding shear numbers $\gamma_{\{10\bar{1}2\}} \approx 0.13$ and $\gamma_{\{10\bar{1}1\}} \approx 0.137$ differ only slightly.

Li and Ma (2009b) recently modeled the development of a $\{10\bar{1}1\}$ twin and its interface movement in magnesium by molecular dynamics. In their simulations, a magnesium single crystal is subjected to a strain driven tensile test. The crystal orientation is such that 2 of the 6 possible twin variants are not triggered, while 4 of them are equally preferable. It is found that in the process of twin nucleation, initially two twin variants develop, one of which is assimilated by the other one as the simulation continues. As the model is symmetric, it is to conclude that a small perturbation, like a dislocation, can cause the unfortunate twin to be the other one. This underlines the affinity of twinning to bifurcation. In order to obtain reproducible results, both, the simulations and the experimental setups should avoid ambiguities like equally preferred twin systems. Another interesting result is that three kinds of interface steps are observed, namely 1,2 and 4-layer steps. While the 1-layer step is sessile, the 2-lacer step is glissile. The 4-layer step is unstable and dissociates into two 2-layer steps, between which a repulsive force is acting. The movement of the interface is connected to the generation of prismatic dislocation. In another work, Li and Ma (2009a) focused on the atomic modelling of a $\{10\bar{1}2\}$ twin interface in magnesium, employing the embedded atom model by Liu et al. (1996). It has been found that the morphological difference between $\{10\bar{1}1\}$ and $\{10\bar{1}2\}$ twinning in magnesium can be explained by the mechanism underlying to the interface movement. In case of the $\{10\bar{1}1\}$ twinning, the interface movement rests upon the movement of partial dislocations, while in case of the $\{10\bar{1}2\}$ twinning, atomic shuffling appears to play the leading role, and no pronounced partial dislocation is observed. Therefore, unlike $\{10\bar{1}2\}$ twinning, the $\{10\bar{1}1\}$ twin propagation is restricted by the partial dislocation density, which renders the $\{10\bar{1}2\}$ interfaces more glissile compared to the $\{10\bar{1}1\}$ interfaces.

A direct comparison to the results of Serra and Bacon is difficult, though no interaction with basal slip dislocations is observed. However, the strategy employed by Li and Ma is promising to give considerable insight into the processes of twin nucleation and propagation, like the atomic shuffling that accompanies $\{10\bar{1}1\}$ twinning and the critical stress states. Unfortunately, Li and Ma (2009b) could not determine the stress necessary for $\{10\bar{1}1\}$ twinning, which is due to the high strain rate that has been applied in their simulation.

In this work we focus on deformation twinning. The appropriate candidate for implementation and testing purposes is the $\{10\bar{1}2\}$ twinning mechanism in magnesium, due to its capability to accommodate moderate deformations without fracture. Moreover, as magnesium and its alloys are of technical interest, the examination of twinning in the hcp structure may prove useful in the process of ductilising magnesium.

2.7 Ductility of Magnesium

At room temperature, crystallographic slip occurs only on the basal plane in magnesium. Therefore, it is not as ductile as needed for serious metal forming. Above 225°C, the pyramidal slip systems are activated (Emles, 1966), and sufficient slip systems are disposable to accommodate an arbitrary deformation.

Some attempts to ductilise magnesium and its alloys aim for providing glissile slip systems at room temperature which have their slip plane not parallel to the basal plane. The pyramidal and the $c+a$ slip systems, which are available at higher temperatures, should be potentially active at room temperature. It is the task of experimenters, metallurgists and molecular dynamic specialists to eventually find a good alloy composition or material processing. Kelley and Hosford (1968) found that alloying Mg with Li (approximately 12 at.%) makes the prismatic $\{10\bar{1}0\}\langle 1\bar{2}10\rangle$ slip systems available by decreasing their critical shear stress, while the shear stress needed for basal slip is increased such that $\tau_{\mathrm{prism}}/\tau_{\mathrm{basal}} \approx 5$ (Haferkamp and Jaschik, 2000). Therefore, a more ductile behaviour at low specific weight ($\rho_{\mathrm{Mg}} = 1,738\mathrm{g/cm}^3,\ \rho_{\mathrm{Li}} = 0.534\mathrm{g/cm}^3$) is obtained, although still no slip systems are available for $\boldsymbol{c}$-axis straining. By adding between 17at.% and 30at.% of Li, a two phase microstructure is obtained, while at a Li fraction of more than 30at.% the magnesium atoms are dissolved in the bcc Li lattice. If enriched, e.g., with aluminium, one obtains an alloy of moderate strength, which is due to its low mass density particular interesting for highly dynamic applications. Very light Mg-Li alloys have been used in the aerospace and arms industry in the 1950s and 1960s, but did not find broad application in civil engineering.

The tensile ductility, microstructure and texture of extruded magnesium to which rare earth elements are added have been recently studied by Stanford and Barnett (2008). The dependence of the tensile ductility and fracture elongation on the alloy composition of cast Mg-Li has been recently studied by Regener et al. (2007).

A more direct approach to produce a more ductile material is to generate a fine microstructure, which has been recently demonstrated for the magnesium alloys ZE41A by Ma et al. (2009) and ZK60 by Li et al. (2009). By a large number of equal channel angular pressing passes (ECAP), an average grain size of approximately 1.5 μm and 0.8 μm is obtained. This can enable so called superplastic deformation mechanisms, which are mainly grain boundary sliding and recovery by dynamic recrystallisation. Similar has been shown for Mg-9Li-1Zn by Kim et al. (2009), who found that a single „high-speed-ratio differential speed rolling" process generates an ultrafine microstructure in Mg-9Li-Zn, which enables a fracture elongation up to 50% of logarithmic strain at room temperature. The ECAP can be used as well to generate a homogeneous texture and particle distribution (Gan et al., 2009).

2.8 Experimentally Observed Twins in Magnesium

In order to illustrate the latter chapter, some micrographs of pure magnesium are presented. Stripes have been cut out of cast magnesium, which has coarse-grained Voronoi-like microstructure. The specimens have been grinded and polished, with a maximum roughness of 1μm. To visualise the morphology, the samples have been etched approximately 40 seconds in 3% nitric acid. As twins

form in magnesium at very low stresses, the preparation procedure induced already a large number of twins, see Fig. 1.1. An impression on the twin formation on loading is given in Fig. 2.8. It has been obtained by preparing a cubic sample as described above. After finding relatively homogeneous and twin free grains, the sample has been gradually deformed in a bench vice, and the grains have been reviewed. One notes that a twin network evolves with ongoing deformation, and the surface of the sample roughens noteably due to the inhomogeneous deformation. An atomic force micrograph of small free twins can be found in Fig. 2.8, left. These twins form part of a line of short, free, parallel twins, (see Fig. 2.8 right, the upper region), which is propably a trace of a scratch that has been introduced during the surface preparation.

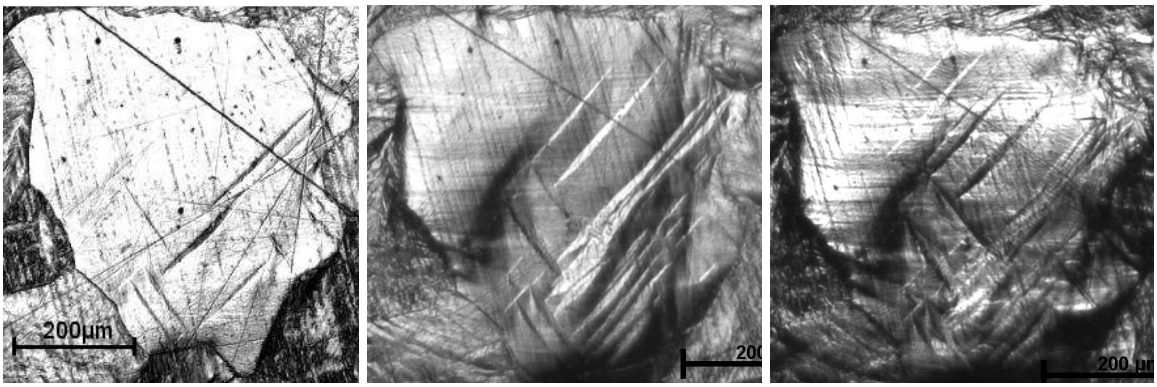

Figure 2.18: Evolution of a twin network under gradual loading.

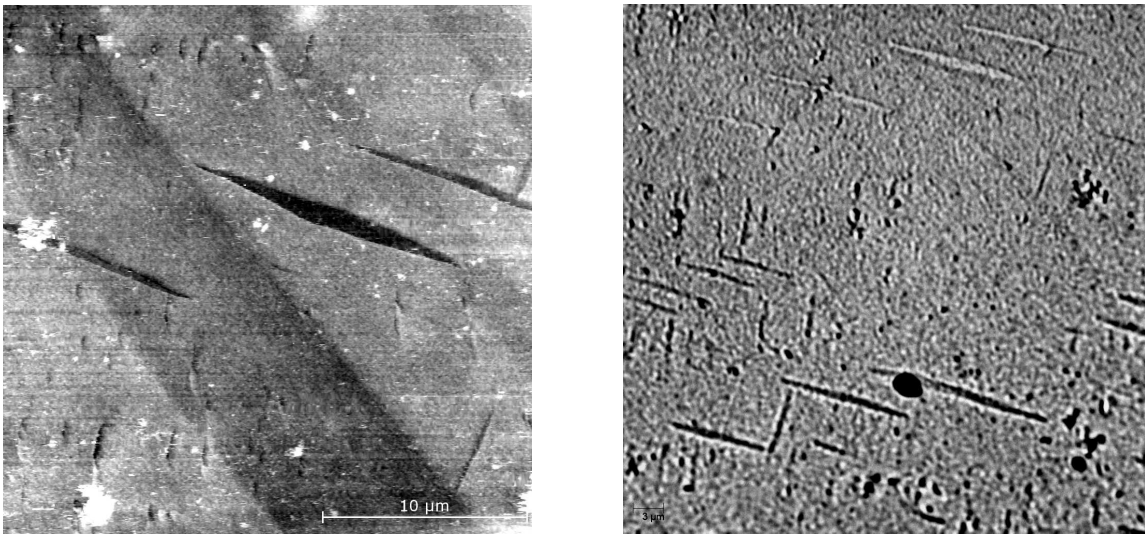

Figure 2.19: A small free twin (left, AFM figure), which belongs to a chain of similar twins (right, optical microscope figure, upper region).

2.9 Twin-Parent Interface

Considering the mirror symmetry of the atomic arrangement found on a coherent twin-parent interface, the classification into twin and parent is rather arbitrary. The unique assignment is given by the

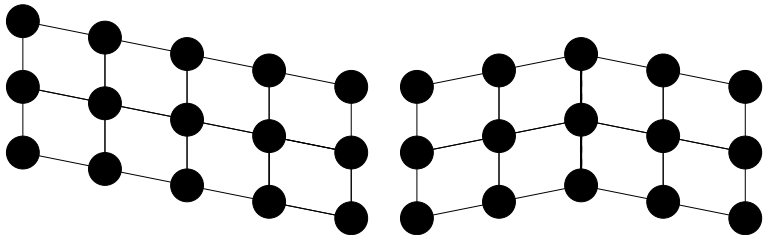

Figure 2.20: Untwinned (left) and twinned (right) crystal. The interface is a a plane of mirror symmetry.

order of appearance, i.e. the parent is the primary structure, while the twin forms afterwards. It has in general a much smaller volume fraction than the parent, and is surrounded by the parent. The twin parent interface can be regarded as a planar perturbation of the crystallographic structure. As such, it contributes to the internal energy, which is physically based on the fact that the atoms on the interface cannot occupy their energy minimising configurations according to the crystal structure (Fig. 2.20). Therefore, the existence of the interface does not correspond to a state of minimum energy, but is determined by the history of the material (Haasen, 1996). Due to the fact that a coherent twin-parent interface is a plane of mirror symmetry, no driving force on the position of the interface is induced by the existence of the interface solely. A driving force can be derived by stating that the interface moves towards the crystal which accommodates the macroscopic strain with the lesser elastic strain, i.e. by minimising the elastic energy. If the driving force is large enough, the partial dislocations move along the interface such that the interface moves towards an energetically favourable configuration. In such a process, the change of the size of the interface is of minor importance, which holds therefore for the interface energy as well.

By assuming that the twins arrange such that a local energy minimum is obtained, one can derive some properties of the twins, if the elastic strain energy and the interface energy are given. E.g., by prescribing the twin geometry except for the thickness, one can obtain the twin thickness by minimising the the sum of elastic strain energy and interface energy (Khachaturyan, 1983). Conversely, this approach can be used as well to estimate the interface energy by measuring the twin thickness (Demczyk, 1990). Additional to the interface and strain energy, one can consider the „intrinsical dissipation" to estimate a critical resolved shear stress (Petryk et al., 2003). These approaches compare distinct states in finite volumes, while the focus in this work is on local modelling equations that are continuous in space and time.

It is generally difficult to treat interfaces in a continuum theory, which is due to the fact that the interfaces represent discontinuities in space and, in the moment of formation, in time, while one is interested in smooth modelling equations. The modelling equations are written down for a material point, which cannot contain discrete interface. Several authors use strain gradients to energetically penalise sharp strain changes like those found at twin-parent interfaces (see, e.g., Truskinovsky and Zanzotto (1996)). Such a strategy has to be regarded as a regularisation of the strain jump at the interface, which requires a strongly nonlinear dependence on the strain gradient. This is inconvenient from the practical viewpoint, though a fine spatial discretisation is needed when the solution is approximated numerically.

Haasen (1996) stated that twin-parent-interfaces should have extremely low energies, with $\mathrm{mJ/m^2}$ being a reasonable measuring unit. In Serra and Bacon (1991), the values $w_{\mathrm{IFMG}\{\bar{1}012\}} \approx 187\mathrm{mJ/m^2}$ and $w_{\mathrm{IFna56}\{\bar{1}012\}} \approx 141\mathrm{mJ/m^2}$ are given. The indexing corresponds to the two different potentials

used by Serra and Bacon (1991) and the twinning mode. Both potentials display characteristics close to real magnesium. The $\{\bar{1}012\}$ twin interface energy is in both cases larger than the interface energy belonging to the less frequently observed $\{\bar{1}011\}$ compression twins, $w_{\mathrm{IFMG}\{\bar{1}011\}} \approx 141\mathrm{mJ/m}^2$ and $w_{\mathrm{IFna56}\{\bar{1}011\}} \approx 79\mathrm{mJ/m}^2$. In fact, the values given for $\{11\bar{2}1\}$ and $\{11\bar{2}2\}$ twinning are below the values for $\{\bar{1}012\}$ twinning as well. The $\{\bar{1}012\}$ twinning mode is the most easily activated twinning mode, although it charges more interface energy than the alternative modes. This leads Serra and Bacon (1991) to the conclusion that the interface energy is of minor importance compared to the partial dislocation core properties.

It appears therefore reasonable to exclude the interface energy from the modelling efforts in the first place, as it is done in many publications (e.g., Kochmann and Le (2009)). It may be used as a fine tuning tool. In fact, some problems that arise in the elastic modelling of twinning are possibly solved by incorporating an interface energy, namely the infinitely fine twin-parent mixing and the energy invariance in conjugate twin systems.

2.10 Twinning-Induced Effects

The twinning mechanism induces a number of practical relevant effects. As twins form as lamella-shaped subgrains with a reoriented lattice (Figs. 1.1, 2.10 and 2.8), twinning contributes strongly to the grain refinement, the morphological texture and the crystallographic texture evolution. Therefore, the elastic behaviour, yield locus and plastic behaviour are altered. Unlike crystallographic slip, twinning is polar and practically reversible (Lubenets et al., 1980), which induces a strength differential effect and a pronounced or reversed Bauschinger effect, depending on the crystallographic texture.

Hardening behaviour. The influence of twinning on the work hardening can be quite complex. An important contribution is given by the dynamic Hall-Petch relation. Due to the grain partitioning by twinning, the mean free path for dislocations movement is reduced, as well as the mean free length for the growth of a new twin. To obtain a certain mean deformation by twinning, more twins have to nucleate (by dislocation movement) in a fine grained structure than in a coarse grained structure.

Recently, it is discussed whether this effect may be rather secondary (Cáceres et al., 2008; Sevillano, 2009) compared to the effect of twin saturation. At the onset of twinning, twins form at the most favourable sites in the crystal. As the potential twinning volume is limited, the available twin formation sites decrease with ongoing deformation. Consequently, the less favourable nucleation sites have to be occupied, for which a higher loading is necessary.

Another contribution to the strain hardening is given by the Basinski mechanism (Basinski et al., 1992), who observed that in fcc Cu8Al glissile dislocations in the parent are converted into sessile dislocations in the twin. To find out whether similar changes happen in hcp crystals is a challenge for experimenters and molecular dynamic simulation experts.

Twinning has a strong impact on the crystallographic texture, which can influence the hardening behaviour. For example, the reorientation of the lattice under $\{\bar{1}011\}$ twinning by approximately 56° can leave the basal plane in a more advantageous orientation for basal slip, which could reduce the yield stress. In $\{\bar{1}012\}$ twins, this effect is negligible due to the reorientation by approximately 86°.

In a cyclic deformation, another contribution to hardening is given by the strength difference of twinning and detwinning, which is due to the unilateral prior twin nucleation. For the magnesium-aluminium alloy AZ31B, Lou et al. (2007) estimated that obstacle-hardening to basal slip (Hall-Petch), textural hardening and the twinning-detwinning strength difference contribute at the same order of magnitude to the overall hardening behaviour. The results, however, depend strongly on the alloy composition, texture and deformation mode.

It has been observed that the work hardening rate may increase as the temperature is raised or the strain rate is decreased (Christian and Mahajan, 1995), which is a rather uncommon behaviour. A possible explanation may be that higher temperatures and lower strain rates promote dislocation movement. As the twin nucleation is explained by the agglomeration of partial dislocations, a possible explanation for this behaviour may be that in a slowly driven test or at higher temperatures, twin nucleation is eased, leading to a high twin density. For magnesium, it is reported that the number of twins increases with a decreasing strain rate (Maksoud et al., 2009). Consequently, the grain partitioning due to twinning, which forwards the Hall-Petch-hardening, is more pronounced than in fast or low temperature tests. When twin nucleation is hindered, but twin propagation not, the first few nuclei have to rapidly expand in order to accommodate the deformation, and fewer but larger twins evolve. In that case, the partitioning of the grains is less pronounced, resulting in a lower work hardening rate. Moreover, the more pronounced slip at high temperatures and low strain rates leaves a more heterogeneous grain structure that hinders twinning.

In alloys, the rather complex hardening behaviour is even more complicated by the slip-twin interaction with precipitates, which can increase the hardening rate especially for twinning-dominated deformations. Fine particles serve as nucleation sites and therefore increase the number of twins, but their size and overall volume fraction is reduced. The twin fragmentation increases the total twin-parent interface, and consequently the stored interface energy, which indicates an increased hardening rate. As precipitates hinder basal slip, which is necessary for accommodating the $\{10\bar{1}2\}$ twin tips, Stanford and Barnett (2009) state that the hardening effect due to precipitates affects this twinning mode always equally or stronger than the basal slip. Clark (1968) found that in a Mg-9 wt.% Al alloy, precipitation plates form along the basal plane, which suppress the $\{10\bar{1}2\}$ twin formation, but not basal glide. Therefore, in this alloy, strain hardening is more relevant than precipitation hardening. Moreover, the hardness can be considerably increased by annealing, which has been confirmed by (Regener and Dietze, 2006). However, other alloying additions (e.g. Zn) can lead to different precipitation behaviour, which can considerably contribute to age hardening (Smola et al., 2004; Liu et al., 2009).

Creep. Twinning can contribute differently to creep, depending on the crystallographic texture and the loading conditions. Sato and Kral (2008) studied creep of cast samples of a complex magnesium alloy. It is found that in the first stage of creep, significant twinning takes place in some grains. In the second stage, steady state creep linearly related to twinning has been observed. Finally, fracture starts mostly from a fully twinned grain that cannot accommodate more deformation. It is to conclude that by adapting the texture appropriate to loading conditions of a part, a certain control over twinning-induced creep is gained. This is especially interesting due to the polarity of twinning, which may be used to adapt textures to the loading conditions, such that creep due to twinning is virtually excluded.

Creep due to twinning can be significantly reduced by the formation of precipitates. In magnesium-rare earth base alloys, „plate shaped precipitates, which form on the prismatic planes of the matrix

in a dense triangular arrangement, provide not only most effective barriers to the motion of basal dislocations motion but are also very effective against creep deformation." (Summary in Smola et al. (2004)).

Moreover, precipitates nucleate at stacking faults, dislocations and grain- or twin boundaries Kaya et al. (2004). The latter hinders the twin boundary motion, and contributes therefore to strain hardening and creep resistance.

Low-temperature ductility. Crystals that deform by twinning can show a behaviour reverse to the experiences made with deformations by crystallographic slip. For example the ductility of CuSn3.1 at.% bronze, silver and the silver alloy AgAu25 at.% is considerably increased as the temperature is lowered to values such as 20K (Reed-Hill and Abbaschian, 1994; Christian and Mahajan, 1995), see Fig. 2.21. Usually, thermal fluctuations assist the rearrangement of atoms and dislocation glide, and one expects the ductility to decrease with temperature. It is to suspect that at higher temperatures, slipping, being the primary deformation mode, causes the grains to deform inhomogeneously. Therefore, an inhomogeneous crystal orientation distribution (COD) inside the grains emerges, which is disadvantageous for twin propagation.

Strain rate dependence. The flow stress due to twinning depends only weakly on the temperature and the strain rate, see Fig. 2.21. For both dependencies, positive and negative sensitivities are reported, depending on the lattice structure and the twin system. The tendency to substitute slip by twinning changes rather slowly with temperature, but rapidly with the strain rate (Christian and Mahajan, 1995). This is due to the higher sensitivity of the slip activity on the strain rate. Moreover, at low strain rates, the grain partitioning due to twinning is more pronounced, which influences the hardening behaviour via a dynamic Hall-Petch effect.

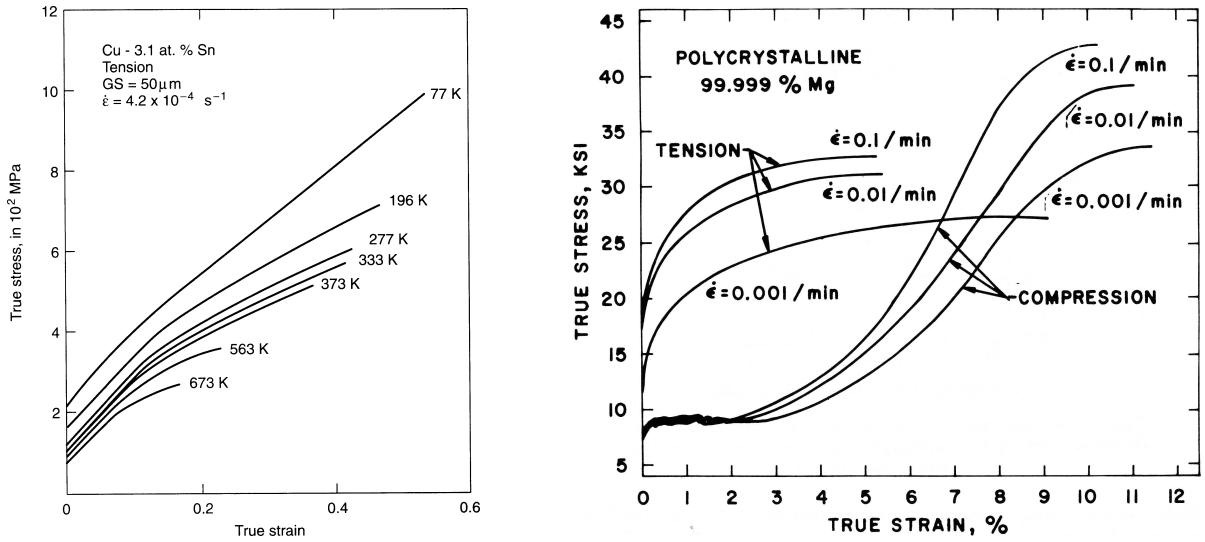

Figure 2.21: Left: Low temperature ductility caused by twinning, from Reed-Hill and Abbaschian (1994). Right: Strength differential effect in textured polycrystaline magnesium at different strain rates, from Reed-Hill (1973). Note that the twinning-induced plateau in the compression test is rather unaffected by strain rate changes.

Elastic twinning. Another unusual and often cited finding is that relatively large twinning-induced strains (up to 12%) may vanish upon unloading, which suggests that the twinning is practically fully elastic (Bolling and Richman, 1965; Lubenets et al., 1980). Bolling and Richman (1965) claim that their FeBe25-specimens deform primarily by twinning and by a negligible amount of slip, and draw conclusions regarding twinning. Unfortunately, the term twinning is misplaced in their work, since they observed mechanical induced martensitic transformations. Therfore, a considerable chemical driving force comes from the fact that the unstable, lower symmetry orthorhombic lattice transforms back to the cubic phase (Laves, 1966). Although this driving force biases most of their findings when applied to pure twinning, they are cited sometimes rather uncritical. If real twinning is considered, the elastically recoverable strains are quite small (Wu et al., 2008).

It is particularly difficult to understand how twins are able to propagate at speeds at the order of the speed of sound, while a reasonable speed for dislocation movement is approximately 50m/s (Sleeswyk, 1964), which is well below the shear wave speed. Therefore, the twin propagation mechanism by partial dislocation movement cannot be the full explanation. It is to suspect that it is a mixture of homogeneous shearing and dislocation movement.

The lightweight metals magnesium and titanium are of high technical interest. Both exhibit a hexagonal atomic structure, which makes both of them prone to mechanical twinning. The known problems connected to twinning, like fracture initiation, strength differential effect and largely unpredictable behaviour are opposed by potential benefits, like an outstanding ductility by inducing the TWIP-effect, or the design of texture distributions adjusted to the components demand (Jiang et al., 2008).

Chapter 3

Simulation of Mechanical Twinning

Since mechanical twinning influences the material properties by changing its microstructure, one is interested in its proper modelling. In the following, a rough overview on the simulation of twinning at different scales is given. For a more detailed account see Roubíček (2004).

3.1 Macromodels

This modelling approach uses and predicts information from the microscale in an averaged and homogenised sense. With respect to mechanical twinning, at one material point, the volume fraction of each phase (e.g. Tomé et al. (1991)) or the average grain size (e.g. Allain et al. (2004)) are predicted. The model length has to be considerably larger than the length scale at which the microscale processes take place. I.e. for twinning, which occurs on the grain scale, the model size has to be at least sufficiently large to cover a representative number of grains. Macromodels have the advantage of being computationally less intense than models that serve on a smaller length scale, and are therefore more useful for engineering problems. Further, if one is only interested in a specific information, one can pick a macromodel that accounts to ones needs.

Macromodels can be formulated purely phenomenologically by adapting model parameters to experimental findings, or they couple a physically motivated approach on the microscale with a necessarily crude analytical homogenisation scheme. A prominent example is the Taylor-homogenisation applied to single crystal slip (see, e.g., Böhlke (2001)). Due to the rough homogenisation, non-negligible information may be lost. For example, the Taylor-homogenisation used to predict the change of the crystal orientation distribution (COD) by crystallographic glide may lack texture components (Böhlke et al., 2007). It also overestimates the texture sharpness. Some remedies for the latter are proposed, e.g. the superposition of an isotropic background model (Böhlke et al., 2006) or of the Sachs homogenisation scheme, which underestimates the texture sharpness (Ahzi and M'Guil (2008) and references within). A more refined homogenisation is the self-consistent scheme, which uses Eshelby's solution (Eshelby, 1957) of an ellipsoidal inclusion to implicitely derive the material behaviour of the surrounding homogenised equivalent medium (HEM).

Macromodels that rely on a homogenisation scheme can be numerically quite expensive. The numerical effort for the determination of the HEM-behaviour as well as the number of internal variables

grows with the number of crystal orientations that are incorporated. In order to approximate an isotropic COD by single orientations, one needs a large amount of orientations to obtain a reasonable approximation. In order to reduce the number of internal variables and calculation time, the ODF can be approximated by weighted components instead of discrete orientations. Different decomposition techniques are proposed in the literature. Prominent techniques are the use of Mises-Fisher distributions around discrete orientations (Fisher, 1953), the spherical harmonics expansion of the ODF (Bunge, 1977) and the tensorial series expansions of the ODF (Böhlke et al., 2006).

A recent application of the self-consistent viscoplastic homogenisation scheme to magnesium and its alloys is given by Proust et al. (2009), who homogenised over 1800 orientations. The used material model is relatively complex by, among other subtleties, incorporating the directional Hall Petch effect, which results in considerable numerical effort. The simulated stress-strain curves for a deformation process including strain-path changes are in reasonable agreement to experimental findings.

Macromodels are mostly computationally advantageous compared to micromodels. However, in order to obtain qualitatively reasonable predictions, complicated models have to be introduced, with a large number of material parameters. In many cases, the material parameters have no physical interpretation, and the quality of the predictions may strongly depend on the strain path, leaving an uncertainty which is not always acceptable. In principle, experimental confirmation is always necessary when results are obtained from microstructural initial conditions that deviate strongly from the conditions at which the material parameters have been adapted. Further, macromodels are improper to gain understanding of the underlying mechanisms. In the context of twinning, a macromodel that respects crystallographic glide and twinning simultaneously cannot offer insight into the interaction between slip and twinning. It can, of course, help to understand observations on the macroscale.

3.2 Micromodels

Micromodels claim to predict the material properties without homogenisation. With respect to mechanical twinning, the crystal (parent or twin) is determined at each material point. By doing so, micromodels automatically have the problem of dealing with the phase transition in an erratic way, while the phase transition as seen from a macroscopic point of view is smooth due to the continuous change of the volume fractions. Therefore, micromodels that incorporate phase changes exhibit some inconvenient properties regarding the stability and the uniqueness of the solution (Abeyaratne and Knowles, 2006), which are object of research in mathematics and mechanics.

The minimum model size is restricted to be larger than the length scale at which the material can no more be described by means of a continuum theory. Therefore, it is doubtful whether the mechanical behaviour of very fine twin structures like observed by Fissel et al. (2006) (≈ 6 atom layers per twin) can be modeled by using a microscale model.

The advantage of microscale modelling is that one can obtain information which is usually lost in the homogenisation process when employing a macromodel. In conjunction with a numerical homogenisation procedure, one is able to obtain more precise estimations of the macroscopic material behaviour as by using a macroscale model. A common numerical homogenisation procedure is the RVE-technique. Being computationally more expensive than macromodels, micromodels offer more precise predictions in return. Moreover, micromodels are simplistic compared to macromodels. While

macromodels should respect in some way the grain morphology and the COD, micromodels contain less modelling parameters, which are determined by the material behaviour of a single crystal. This is advantageous for the physical interpretation of the modelling parameters, as well as for the reproducibility of the experiments. Compared to macroscale considerations, in a repeated experiment bias due to different microstructures is excluded. A micromodel in which twinning and slip are simultaneously incorporated may help to understand their interaction, though experiments become more difficult the smaller the length scale is.

This is motivation enough for setting up micromodels for mechanical twinning, which has been done by Silling (1989); Collins (1993); Forest and Parisot (2000); Idesman et al. (2000); Lapczyk et al. (2000); Pitteri and Zanzotto (2002); Wang et al. (2004). Silling (1989) and Collins (1993) approach the problem by setting up a nonconvex elastic energy function, which has been suggested by Ericksen (1980). Silling (1989) uses his CHIMP algorithm to track the twin evolution, but does not consider real twinning modes, avoiding the problems explained in Section 4.8. Collins (1993) treats the problem as purely elastic. He approaches the global energy minimum by using an optimisation algorithm, and obtains phase mixtures as fine as the spatial discretisation allows. Forest and Parisot (2000) approach mechanical twinning by regarding twin systems as slip systems that undergo softening until reaching the twin shear. In contrast to Silling (1989) and Collins (1993) his model allows for the straightforward use of a critical twinning stress. Idesman et al. (2000); Lapczyk et al. (2000) use an order-parameter that smears out the transition from one phase to another. Wang et al. (2004) describes the formation of martensitic plates by using the phase-field-microelasticity. Each modelling technique has its advantages and disadvantages, like the possibility of remaining ”intermediate twins” after load removal (Forest and Parisot, 2000; Idesman et al., 2000), restriciton to small strains (Wang et al., 2004) or the overestimation of critical strains and stresses (Silling, 1989).

One may ask why one should not set the material model instantaneously from the parent to the twin configuration as, e.g., a resolved shear stress condition is reached. A straightforward approach could be to reorient the stiffness tetrad and map the stress-free configuration by the corresponding shear strain. Unfortunately, such a model would induce instantaneously, due to the relatively large shear strain, large elastic stresses. These elastic stresses would cause, if it were permitted, immediate detwinning on the same system. Moreover, in a numerical simulation, the large elastic stresses would cause a snowballing twin growth, far from realistic behaviour.

From the latter considerations it is clear that modelling a continuous shift from the parent to the twin configuration is a more promising approach. In this work, a continuous differentiable nonconvex elastic strain energy is employed. If one is interested in a an inelastic modelling approach, a starting point could be to postulate differential equations which describe the evolution of the twin volume fractions, where the condition that the phase volume fractions have to sum up to one at any time has to be fulfilled. The behaviour of the latter defines whether one obtains a macro- or a micromodel. If stable phase mixtures are predicted, one has a macromodel, while one has a micromodel if only the one-phase states are stable. In case of a micromodel, it may be a good idea to employ delayed differential equations, though the existence of a waiting time for twin growth has been confirmed experimentally (Kawabata et al., 2000). DDEs can be designed such that the reaction does not immediately follow to the cause, which allows to incorporate the waiting time, as well the snowballing twin propagation can be avoided.

3.3 Molecular Dynamics

Modelling on the molecular level combined with numerical evaluation and homogenisation is very helpful in understanding macroscopic phenomena, see, e.g., the references in Section 2.6, or the recent works of Hildebrand and Abeyaratne (2008); Jin et al. (2008); Xu et al. (2008); Kastner and Ackland (2009); Li and Ma (2009b). Li and Ma (2009b) accomplished to simulate the complex 3D atom movement that accompanies the interface movement of a $\{10\bar{1}1\}\langle 10\bar{1}\bar{2}\rangle$ compression twin, which is in reasonable agreement with TEM observations. If the computing power increases further, one may think of a numerical two-step homogenisation, from the atomic scale to the grain scale and from the grain scale to the macroscale. In such a modelling strategy, not only spatial but temporal homogenisation would be necessary. Although a large number of problems has to be solved for such an approach, it may be capable of reproducing a large variety of observations, including slip and twinning, by very few modelling parameters that are interpretable on the atomic scale. By applying the Cauchy-Born rule to a periodic unit cell of atoms (which makes the Taylor assumption appear to be very mild), one may already analytically deduce a nonconvex strain energy from summing up the atomic potentials, which would already recover the energy minimum for shuffle-free twin configurations. For magnesium, the embedded atom model of Liu et al. (1996) could serve as a starting point (disposable at http://www.fisica.uniud.it/∼ercolessi/potentials/Mg/). Liu et al. (1996) adjusted the three characteristic functions (pair potential, embedding energy function and density function) by piecewise cubic splines to magnesium, such that many properties of the magnesium single crystal are reproduced.

For now, molecular dynamics are unattractive for engineering applications. Microscale models appear to fall in range of practicability soon, as the increased research activities in the use of the FE^2 method suggest.

Chapter 4

Setting up a Micromodel

4.1 Elastic Modelling of Phase Transitions

Consider the following 1D-example: Two horizontally aligned and compressed springs are connected by a joint, which can only move vertically (see Fig. 4.1, which may be a switch or similar). By applying a force F in vertical direction, one is able to change the stress-free configuration to which the system returns after load removal, if F is sufficiently large. Apparently, a permanent deformation can be obtained, with purely elastic ingredients. In regard of this, such material behaviour is often referred to as pseudoelastic. It is in principle possible to construct a chain of such switches, which would allow for a gradual increase of the permanent deformation, similar to the practically continuous plasticity induced by dislocation movement. Such chains of snap-springs have been used by Müller and Villaggio (1977) to model plastic material behaviour. By imposing a certain displacement at the ends of such a chain, it is clear that the imposed deformation can be achieved by more than one combination of flipping snap-springs, which indicates that the pseudoelastic boundary value problem needs not to have a unique solution. With such behaviour has to be dealt when one approaches mechanical twinning. One

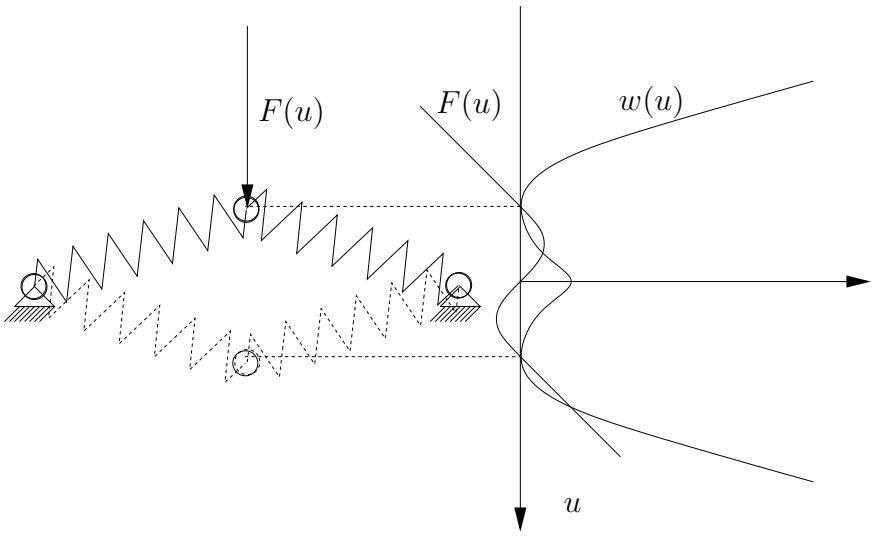

Figure 4.1: Sketch of a snap spring.

notes that in the example there is a third equilibrium configuration with $F = 0$ just halfway between the two energy minimising configurations. The energy-criterion generally adapted (Ericksen, 1975) tells that this is not a stable configuration. By considering the second derivative of the strain energy with respect to the displacement we find $w''(u) < 0$, which corresponds locally to a negative Youngs modulus. With w'' being the curvature of w, one could say that this is in the nonconvex range of w. It separates clearly the two ranges where a stable equilibrium can be found. Therefore, as micromodels claim to predict which phase forms at a material point instead of phase mixtures, nonconvex elastic modelling appears to be appropriate for this purpose. For illustrative purposes, take the potential

$$w(u) = (u-1)^2(u+1)^2, \tag{4.1}$$

which could be of a snap-spring. For the sake of simplicity it is assumed that material parameters are normalised, and physical units are ignored. The force-displacement curve is given by

$$F = w'(u) = 4(u^3 - u), \tag{4.2}$$

and the tangential modulus E is given by

$$E = F'(u) = w''(u) = 4(3u^2 - 1), \tag{4.3}$$

see Fig. 4.2. By demanding $F = 0$ one finds the three force-free configurations $u_{F=0} = \{-1, 0, 1\}$. They correspond to local extrema of $w(u)$, of which $u = 0$ corresponds to a local maximum and $u = \pm 1$ to local minima, i.e. $E(u = 0) < 0$ while $E(u = \pm 1) > 0$. The roots $u_{1,2} = \pm 3^{-0.5}$ of E correspond to the local extrema of F and mark the points where w changes from a convex to a concave curvature.

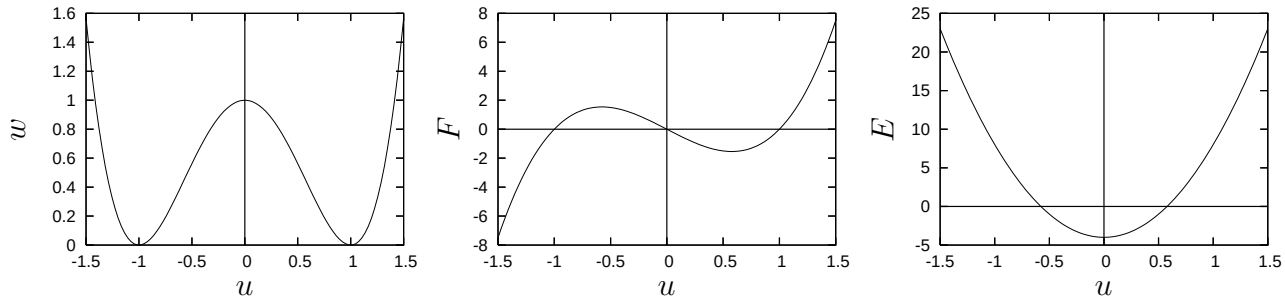

Figure 4.2: Strain energy $w(u) = (u-1)^2(u+1)^2$ and its first and second derivative, namely the force displacement curve and the tangent modulus.

4.2 Solution Strategies for the Pseudoelastic Model

Mechanical twinning is modelled here based on a nonconvex elastic energy density w. The solution of the quasistatic elastic boundary value problem is obtained by minimising the stored energy

$$W = \int_\Omega w(\boldsymbol{C}) \mathrm{d}V \tag{4.4}$$

by determining $\boldsymbol{C}$ such that $\min(W)$ is obtained, where Ω denotes the domain that is occupied by the elastic body. It is well known that w must be at least rank one convex to ensure the existence of a unique minimiser and to prevent the prediction of infinitely fine phase mixtures. A fundamental work on convexity in elasticity is given by Ball (1977). Note that all hyperelastic laws that are isotropic and physically linear in a Lagrangian strain measure $\boldsymbol{E} = f(\boldsymbol{C})$ fail to be rank one convex (Bertram et al., 2007), like e.g. the widely used Saint-Venant Kirchhoff law. This, however, happens usually at strains which are too large to expect elastic behaviour.

In order to obtain a well-posed problem, one can enforce a convex strain energy by carrying out modifications. However, one can interpret the deficiency of the pseudo-elastostatic boundary value problem as a lack of physical considerations (Abeyaratne and Knowles, 2006). Regarding the fact that most phenomena which are modelled by the pseudoelastic approach are strain path-dependent (twinning, martensitic transformations), it appears to be reasonable to not stick to a purely elastic modelling, but introduce a kinetic relation. However, the most prominent convexification techniques, namely the relaxation of w or the introduction of an adequate strain gradient dependence, should be mentioned shortly.

Convexification. Given a nonconvex strain energy, one may construct a convex hull, and use it in place of the starting strain energy (Pagano and Alart, 1999; Lambrecht et al., 2003; Bartels et al., 2004; Carstensen, 2005). Obviously, one looses the nonconvex branches of the strain energy. In this way, the uniqueness of the solution can be restored at the cost of a clear assignment of the different phases at each material point. Nevertheless, a volume fraction of each phase at each material point can be locally determined by looking at the distance of the solution from the stress-free configurations that correspond to the individual phases (see Fig. 4.3). Talking about volume fractions, one has arrived at a macromodel. Therefore, the convexification procedure is a special way of homogenisation, which comes along with loss of information about the microstructure. One can refer to the convexified strain energy as the mesoscopic strain energy, while the nonconvex strain energy is interpreted as the microscopic strain energy (Peigney, 2009).

In the 1D-case, the construction of a convex hull is not difficult. However, different convex hulls lead to different material behaviour. In the above example, the determination of a tangent that connects the two minima leads to a constant force displacement curve, which leaves the uniqueness issue unresolved (Fig. 4.3). In the example, $F = 0$ corresponds to any displacement between -1 and 1. In this branch, the material behaves fluid-like. In the multidimensional case, convexity appears to be a criterion that is too strict. For example, elastically almost incompressible material behaviour already violates the convexity condition. Therefore, weaker notions of convexity are applied, namely poly-, quasi- and rank one-convexity (Ball, 1977). Moreover, the construction of a convex hull is not as straightforward as in the 1D-case, and mostly several simplifying assumptions are necessary, like elastic isotropy in all phases and small strains. Sometimes, the construction of a convex hull is referred to as a relaxation procedure, because it corresponds to the relaxation of the constraint that at each material point only one phase exists. Some recently proposed relaxation procedures can be found in Pagano and Alart (1999); Lambrecht et al. (2003); Acerbi et al. (2003); Govindjee et al. (2003); Schmidt (2008) and Peigney (2009).

Higher-order strain gradients. By incorporating a contribution of the strain gradient to the elastic energy, one is able to penalise sharp strain gradients, which means that infinitely fine phase mixtures

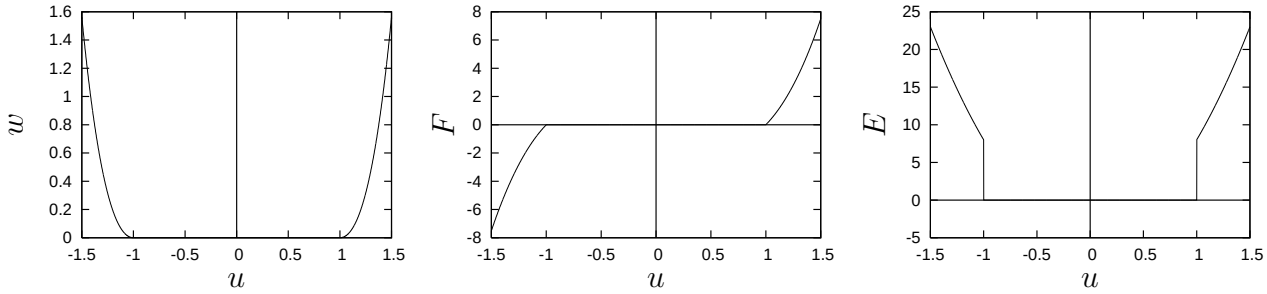

Figure 4.3: Convexified strain energy $w(u) = (u-1)^2(u+1)^2$ and its first and second derivative, namely the force displacement curve and the tangent modulus. The former minima at $u = \pm 1$ correspond to the phases 1 and 2. Phase volume fractions can be calculated by considering the distance from the former minima. For example, at $u = 0$ one could speak of a 1:1 phase mixture.

are no more minimisers of the global strain energy. Physically, this comes close to the incorporation of an interface energy, and is therefore denoted as a capillarity. Moreover, the convexity of the strain energy is determined by the dependence on the highest strain gradient (Sidi Ammi and Torres, 2008), i.e., one can regain the overall convexity of the strain energy but maintain a nonconvex dependence on the strains. The use of higher-order strain gradients, however, has certain disadvantages. In reality, the deformations undergo a sharp jump at an interface separating the two phases. Therefore, the penalisation of sharp strain gradients corresponds to a regularisation of the jump at the interface. In order to obtain a reasonable approximation of the strain jump, the dependence of the strain energy on the strain gradient has to be strongly nonlinear. Moreover, the numerical treatment is more difficult, as well as the interpretation of the additional boundary conditions that have to be specified.

Kinetic relation. Abeyaratne and Knowles (2006) state that the missing part of the pseudoelastic boundary value problem is a nucleation criterion plus a kinetic relation. Haasen (1996) stated similarly that phase mixtures are the result of kinetic processes, not of energy minimisation alone. Even Gibbs himself supposed the existence of obstacles, preventing global energy minimisation (Pego, 1987). In fact, it is known that the interface movement underlying the twin propagation is controlled by the movement of partial dislocations, which has to be considered as a kinetic process. Even in the case of the snap spring one can argue that the joint must have a mass, and consider the pseudo-elasto-dynamic problem. By incorporating a kinetic relation, time-dependence enters into the considerations. One does not consider a global energy minimum anymore, but tracks the evolution of a system.

Two common methods to introduce a kinetic relation are to incorporate dynamics or to regard the material behaviour as visco-pseudoelastic. One can speak about the dynamic and the viscous regularisation. The viscosity term incorporates the dissipation of energy into the model, unlike the dynamic regularisation. In order to demonstrate the characteristics of both regularisations, the example problem from Section 4.1 is regularised. A force F_{ext} is applied, which has to be in balance with the reaction force of the snap spring. In case of the dynamic regularisation the differential equation to solve is

$$F_{\text{ext}} = w'(u) + m\ddot{u}, \tag{4.5}$$

while in the viscous case

$$F_{\text{ext}} = w'(u) + \eta\dot{u} \tag{4.6}$$

has to be solved. The initial conditions are $u(t=0) = -1$, and $\dot{u} = \ddot{u} = 0$. Physical units are ignored again. The external force is raised proportional in time, the factor of proportionality is 1. The results of the numerical time integration of both equations are given in Fig. 4.4. As the local force maximum $F \approx 1.54$ at $u = -1/\sqrt{3}$ is reached, the joint jumps to the opposing configuration. In case of the dynamic regularisation, loaded with kinetic energy, it oscillates around the stable equilibrium configuration, while in case of the viscous regularisation no oscillation results.

The work needed to carry out a $u(t)$-controlled process is given by

$$W = \int_{u_{\text{start}}}^{u_{\text{end}}} F \mathrm{d}u. \tag{4.7}$$

Inserting $F = w'(u) + m\ddot{u}$ yields

$$\begin{aligned} W &= \int_{u_{\text{start}}}^{u_{\text{end}}} (w'(u) + m\ddot{u}) \mathrm{d}u && (4.8)\\ &= w(u_{\text{end}}) - w(u_{\text{start}}) + m \int_{u_{\text{start}}}^{u_{\text{end}}} \frac{\mathrm{d}\dot{u}\mathrm{d}u}{\mathrm{d}t} && (4.9)\\ &= w(u_{\text{end}}) - w(u_{\text{start}}) + m \int_{\dot{u}_{\text{start}}}^{\dot{u}_{\text{end}}} \dot{u}\mathrm{d}\dot{u} && (4.10)\\ &= w(u_{\text{end}}) - w(u_{\text{start}}) + \frac{m}{2}(\dot{u}_{\text{end}}^2 - \dot{u}_{\text{start}}^2). && (4.11) \end{aligned}$$

If one returns to the initial state by driving a circular process, i.e. $u_{\text{end}} = u_{\text{start}}$ and $\dot{u}_{\text{end}}^2 = \dot{u}_{\text{start}}^2$, no energy is needed or gained, which means that the system is conservative. In the case of the additional viscous force one obtains

$$\begin{aligned} W &= \int_{u_{\text{start}}}^{u_{\text{end}}} (w'(u) + \eta\dot{u}) \mathrm{d}u && (4.12)\\ &= w(u_{\text{end}}) - w(u_{\text{start}}) + \eta \int_{u_{\text{start}}}^{u_{\text{end}}} \frac{\mathrm{d}u}{\mathrm{d}t}\mathrm{d}u\frac{\mathrm{d}t}{\mathrm{d}t} && (4.13)\\ &= w(u_{\text{end}}) - w(u_{\text{start}}) + \eta \int_{t_{\text{start}}}^{t_{\text{end}}} \dot{u}^2 \mathrm{d}t. && (4.14) \end{aligned}$$

A general solution for the latter integral cannot be given, but one notes that the integrand is positive for any $\dot{u} \neq 0$, i.e. any circular process with $t_{\text{end}} > t_{\text{start}}$ and $\eta > 0$ must give a positive W. This means that an energy input is necessary to carry out the process. Conservation of the total energy is a basic principle in physics. However, it is not necessary to model the temperature increase due to the internal friction (e.g. by dislocation movement) if it is not of interest. The viscous force represents a convenient modelling tool to incorporate dissipative effects without introducing, e.g., the temperature field.

The zero-dimensional snap-spring serves as a draft for Ericksen's bar (Ericksen, 1975), a one-dimensional bar with an analogous nonlinear material law. Let $[0, L]$ denote the length of a bar. The equation of motion without body forces at each point is given by

$$F_{,x} = \rho\ddot{u}, \tag{4.15}$$

with ρ being the mass per length unit. The force F depends on the strain and the strain rate by

$$F = w'(u_{,x}) + \eta\dot{u}_{,x} \tag{4.16}$$

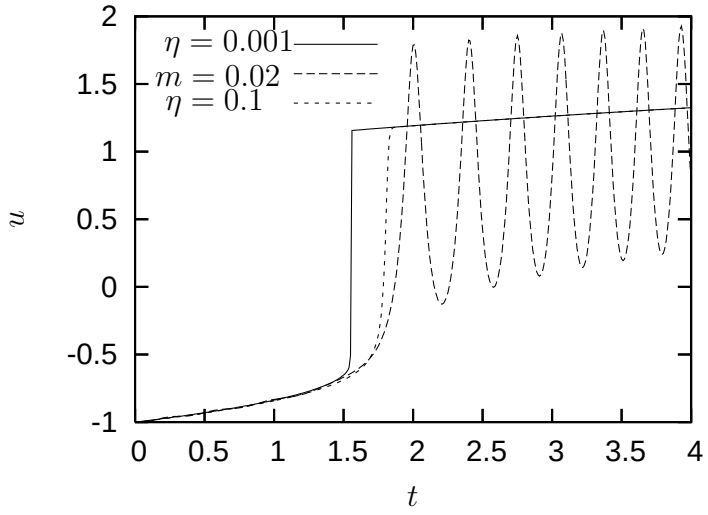

Figure 4.4: Result of the numerical time integration of eq. 4.5 and 4.6. One notes that in case of the dynamic regularisation the systems oscillates around the stable configuration after snapping through.

which is an unspecified stress-strain law resulting from a strain energy $w(u_{,x})$ plus a linear viscosity. This partial differential equation can be rewritten as

$$w''(u_{,x})u_{,xx} + \eta\dot{u}_{,xx} - \rho\ddot{u} = 0. \tag{4.17}$$

Dynamic regularisation. Setting $\eta = 0$ one obtains a second-order PDE, which can be classified by looking at the coefficients w'' and ρ, which belong to the highest derivatives. According to the nomenclature of conic sections, the PDE is elliptic, parabolic or hyperbolic if $-w''\rho$ is greater, equal or lower than zero, respectively. Note that the type of the PDE changes as w'' changes its sign. In case of a standard material with $w'' > 0$ and $\rho > 0$, one has to handle a hyperbolic PDE. Its treatment is considerably more difficult than in the other cases. One has to deal with travelling waves, shocks that can emerge even if the initial data is smooth, and it may happen that due the lack of damping stationary states are not reached. Moreover, the second time derivative induces a more complicated numerical treatment when the time integration is carried out. As the $\rho\ddot{u}$-term stems from the potential of the kinetic energy, both terms represent local changes of energies. Thus, there is no damping due to the energy balance between strain and kinetic energy.

Viscous regularisation. Setting $\rho = 0$ corresponds to the quasistatic treatment. In the resulting PDE one can replace $\varepsilon = u_{,x}$, which yields

$$w''(\varepsilon)\varepsilon_{,x} + \eta\dot{\varepsilon}_{,x} = 0. \tag{4.18}$$

This PDE is hyperbolic if $\eta^2 > 0$, which holds for real values of η. Although eq. 4.18 is still a hyperbolic PDE, its treatment is less difficult than in case of the dynamic regularisation. It is formulated in terms of strains, which means that solutions of eq. 4.18 do not depend on the choice of the strain measure, while eq. 4.17 can be considerably complicated if a nonlinear strain measure is employed. It contains only one mixed second derivative compared to two second derivatives with respect to x and t in eq. 4.17. Thus, the numerical time integration is less difficult. Further, a positive

viscosity is connected with energy dissipation, which allows for stationary states. Finally, one can say that most solids exhibit a positive viscosity, though relatively small in metals, which renders the latter regularisation physically substantiated.

The mathematical treatment of Ericksen's bar is challenging. The case of a strictly monotonic increasing elastic law combined with a linear viscosity has been considered by Greenberg et al. (1968); Greenberg (1969); Greenberg and MacCamy (1970), who showed the existence, uniqueness and stability of global solutions. Dafermos (1969) analysed the dynamic one-dimensional viscoelastic bar in a more general way, and found that the viscous part dominates the elastic part and assures the existence of a unique solution in the large, and that this solution is asymptotically stable in the sense that as t tends to ∞ the stresses and time derivatives of u vanish. Moreover, the positive viscosity ensures the compliance of the Clausius-Duhem-inequality.

The uniqueness of the solution has been restudied by Andrews (1980); Andrews and Ball (1982), where the asymptotic behaviour is examined, and the incorporation of a strain gradient is proposed as a remedy for the uniqueness issue, all focusing on a linear rate dependence. Pego (1987) shows that solutions tend strongly to stationary and stable states in time, which may contain coexistent phases, but are not necessarily minimisers of the energy. He argued that the minimisation of energy does not serve as a stability criterion in materials undergoing phase changes. Haasen (1996) stated similarly that phase mixtures are the result of kinetic processes, not of energy minimisation alone. In regard of this, Abeyaratne and Knowles (2006) suggest to equip a nonconvex energy-minimisation problem with a kinetic relation. As mentioned before, Gibbs also supposed the existence of obstacles that prevent global energy minimisation.

However, when focusing on energy minimisation alone, it has been found that the state of minimum energy is obtained by an infinitely fine phase mixture (see, e.g., Ball and James (1987); Truskinovsky and Zanzotto (1996); Carstensen (2005); Abeyaratne and Knowles (2006)). Ball et al. (1991) found that if the strain energy is supported with a nonlocal potential energy term (a strain-gradient dependence), a dense set of solutions of Ericksen's bar model represent energy minimisers. Moreover, the artificial result of infinitely fine phase mixtures is also avoided. Physically, the incorporation of strain gradients into the strain energy corresponds to a penalisation of steep strain gradients as found at interfaces (Truskinovsky and Zanzotto, 1996). The augmentation of the strain energy can serve as a selection criterion, avoiding the non-uniqueness of the minimisation problem (Truskinovsky and Zanzotto, 1996). By extending the strain energy with a strain gradient, rank one convexity can be ensured, and energy minimisation can be applied. However, the numerical treatment is more difficult, as well as the interpretation of the additional boundary conditions that have to be specified.

Regarding the kinetic relation, the viscous regularisation is by far the most favourable extension to the pseudoelastic model. Efendiev and Mielke (2006) showed that solutions can be established by considering the limit of the viscous regularisation $\eta \to 0$. Although the use of a viscous regularisation is hardly manageable analytically in the three-dimensional case, it proved to be a useful tool in crystal plasticity (Hutchinson, 1976; Asaro and Needleman, 1985; Böhlke, 2004). There, it does not only avoid the Taylor problem of uniquely selecting a combination of active slip systems that realise the plastic deformation. Moreover, instabilities due to softening coming from the rotation of the crystal (geometric softening can cancel out strain hardening) are avoided as well. Further, by choosing a proper dependence on the strain rate, it can be regarded as a penalty method in perfect plasticity, transforming the system of algebraic and differential equations into ordinary differential equations,

which can be treated by well established numerical methods (Simo and Hughes, 1998).

Summarising, one can say that a regularising viscosity is physically reasonable and mathematically helpful. In regard of this, the viscous regularisation is used in this work. The overall modelling strategy employed here is therefore as follows.
1.) Construct a nonconvex energy density w with local minima with $w = 0$ at each stress-free configuration (parent and twins). This is done in terms of Green's strain $\boldsymbol{E}$.
2.) Derive the material law by taking $\boldsymbol{T} = \partial w / \partial \boldsymbol{E}$, with $\boldsymbol{T}$ being the second Piola-Kirchhoff stresses.
3.) Add a regularising viscosity term to the material law. By this, the modelling category is no more a global energy minimisation, but an evolution equation.
The model derivation is given in the following Sections.

Numerical Problems and Homogenisation. It is well known that nonconvex energy minimisation without a capillarity can lead to infinite fine phase mixtures. When such a minimum is approached numerically, the solution oscillates at the level of the spatial discretisation (Carstensen, 2005). Moreover, even if the solution does not oscillate, it does not need to be unique, as the spatial arrangement of the phase mixture may be arbitrary. However, if treated numerically, although one may not observe convergence on the microscale as the spatial resolution is increased, it is shown that the homogenised quantities converge (Bartels et al., 2004).

4.3 Construction of the Nonconvex Strain Energy

Ball and James (1987, 1992) argued that the energy density w of a material that can form n different phases is given

$$w(x) = \min_{i=1\ldots n} (w_1(x), w_2(x), \ldots w_n(x)). \tag{4.19}$$

In words: the determining energy density is the smallest individual energy density w_i of the n potential phases. Applied to the snap-spring example, one could approach the strain energy in each phase by a quadratic relation, and compose w using the Ball and James-approach (see Fig. 4.5). In general, the w_i depend on the deformation, temperature and internal variables. By changing the temperature, it may happen that another w_i becomes smaller than the current one. For example, in martensitic transformations, one crystal structure becomes at a transformation temperature more favourable than another one, involving, e.g., transformations from a bct to a fcc lattice (NiTi). Here, the w_i depend only on the deformation, though twinning is (unlike martensitic transformations) not temperature-driven. Of course, the temperature plays a role for the movement of the partial dislocations, but one can treat twinning without regarding the temperature-dependence, though unlike martensitic transformations twinning does not change the crystal class. If the temperature dependence is not neglectable, it may be more suggestive to assemble the overall stored energy by the partition function

$$w(x) = -k_B \theta \ln \left(\sum_{i=1}^{n} e^{\frac{-w_i(x)}{k_B \theta}} \right), \tag{4.20}$$

with the Boltzmann constant k_B and the tempertature θ (Roubíček, 2004). The latter composition is backed up by statistical physics, and gives a continuous stored energy. However, neither the position

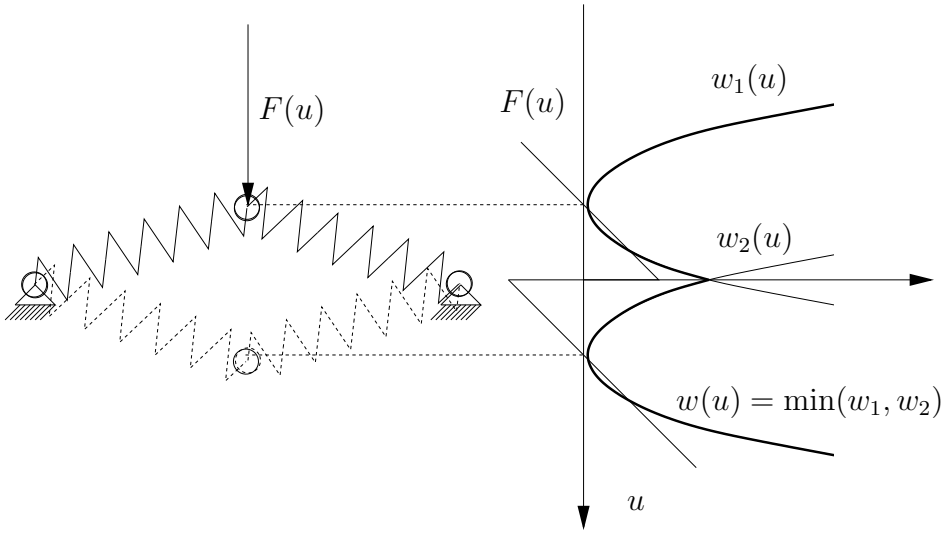

Figure 4.5: Example for a nonconvex elastic energy (bold) composed from two convex (quadratic) strain energies.

of the minima nor the properties close to the minima, essentially the elastic modulus, are conducted from the individual strain energies to the compound stored energy.

By using the work-conjugacy of Green's strain and the second Piola Kirchhoff stresses, the stresses are given by the strain energy by

$$\boldsymbol{T} = \frac{\partial w(\boldsymbol{E})}{\partial \boldsymbol{E}}. \tag{4.21}$$

The algebraic assignment (4.19) is evaluated pointwise. As such, it is not continuously differentiable. In order to get a continuous stress-strain law, in the following Section a regularisation to replace eq. (4.19) is constructed.

4.4 A Regularisation for the Ball and James-Approach

Here, the strain energies depend only on the strain $\boldsymbol{E}$, which is omitted in the remainder. The regularisation for the Ball and James-approach (4.19) should contain a regularisation parameter, say k, so that the limit becomes

$$\lim_{k\to\infty} \tilde{w} = w. \tag{4.22}$$

The w_i represent the elastic strain energies, which means that $w_i = 0$ in the stress-free state, and $w_i \geq 0$ holds. As a starting point, the pointwise addition

$$\tilde{w} = \sum_{i=1}^{n} a_i(w_1, w_2, \ldots w_n) w_i \tag{4.23}$$

is made (Glüge and Böhlke, 2007), where the a_i are weight factors. In the limit case (eq. 4.22), the weight factor a_m of the smallest w_m should approach 1, while all the other a_i should tend to zero.

Therefore the normalisation

$$\sum_{i=1}^{n} a_i(w_1, w_2, \dots w_n) = 1 \tag{4.24}$$

is imposed. It is obtained by

$$a_i(g_1, g_2, \dots g_n) = \frac{g_i(w_1, w_2, \dots w_n)}{\sum_{j=1}^{n} g_j(w_1, w_2, \dots w_n)} \tag{4.25}$$

where now $g_i(w_1, w_2, \dots w_n)$ has to be specified. The location of the minima of the individual w_i are transferred to $\tilde{w}$ independently of the regularisation parameter k. This restriction is imposed in order to not alter the location of the stress-free configurations by the choice of k. As the minimum of the individual strain energies w_i is equal to zero, the $g_i(w_1, w_2, \dots w_n)$ are constructed such that all $g_i(w_1, w_2, \dots w_n) = 0$ and $g_m(w_1, w_2, \dots w_n) > 0$ when $w_m = 0,\ i = 1 \dots n, i \neq m$. This results in vanishing $g_i(w_1, w_2, \dots w_n)$ except the one $g_m(w_1, w_2, \dots w_n)$ corresponding to the vanishing energy density w_m. The imposed restrictions are met by the ansatz

$$g_i(w_1, w_2, \dots w_n) = h(w_i) \prod_{j=1, j\neq i}^{n} (1 - h(w_j)) = \frac{h(w_i)}{1 - h(w_i)} \prod_{j=1}^{n} (1 - h(w_j)) \tag{4.26}$$

with

$$h(w = 0) = 1, \qquad h(w \to \infty) = 0. \tag{4.27}$$

By this constraint, the minima of the w_i are transferred to $\tilde{w}$ independently of the regularisation parameter k, as long as the minimum corresponds to a zero energy density. The constraints imposed on $h(w)$ are met, e.g., by

$$h(w) = \exp(-kw). \tag{4.28}$$

By inserting the deduced $g_i(w_1, w_2, \dots w_n)$ into the $a_i(g_1, g_2, \dots g_n)$, one sees that the product term is cancelled out, and it suffices to take

$$g_i = \frac{h(w_i)}{1 - h(w_i)}. \tag{4.29}$$

Finally, the regularised strain energy

$$\tilde{w} = \left(\sum_{j=1}^{n} \frac{h(w_j)}{1 - h(w_j)} \right)^{-1} \sum_{i=1}^{n} \frac{h(w_i)}{1 - h(w_i)} w_i, \qquad h(w) = \exp(-kw) \tag{4.30}$$

is obtained. The given approach is visualised for testfunctions in Fig. 4.6. In the remainder of this Section it is shown that the regularisation approaches the Ball and James-approach from above for $k \to \infty$. For facility of inspection, the chain-like dependency of $a_i(g_1, g_2 \dots g_n)$, $g_i(w_i)$ is omitted in the notation.

By subtracting pointwise the smallest w_m out of the w_i from $\tilde{w}$ gives a remainder $\delta = \tilde{w} - w_m$, which should vanish for $k \to \infty$:

$$\delta = \sum_{i=1}^{n} a_i w_i - w_m, \qquad w_m = \min_{i=1\dots n} (w_1, w_2, \dots w_n). \tag{4.31}$$

All w_i can be written as w_m plus some positive difference Δw_i

$$\delta = \sum_{i=1}^{n} a_i(w_m + \Delta w_i) - w_m. \tag{4.32}$$

With $\sum_{i=1}^{n} a_i = 1$ one finds

$$\delta = \sum_{i=1, i\neq m}^{n} a_i \Delta w_i, \tag{4.33}$$

which is positive due to $a_i \geq 0$ and $\Delta w_i \geq 0$. This means that $\tilde{w} \geq w$, which means that the regularisation approaches the Ball and James-approach from above. To show that δ tends to zero for $k \to \infty$, the latter equation is divided by a_m, which corresponds to the weight factor of w_m:

$$\frac{\delta}{a_m} = \sum_{i=1, i\neq m}^{n} \frac{a_i}{a_m} \Delta w_i, \tag{4.34}$$

Calculating the limit $k \to \infty$ of the a_i/a_m yields

$$\lim_{k\to\infty} \frac{a_i}{a_m} = \lim_{k\to\infty} \frac{g_i}{g_m} \tag{4.35}$$

$$= \lim_{k\to\infty} \frac{h(w_i)(1 - h(w_m))}{h(w_m)(1 - h(w_i))} \tag{4.36}$$

$$= \lim_{k\to\infty} \frac{h(w_i)}{h(w_m)} \lim_{k\to\infty} \frac{1 - h(w_m)}{1 - h(w_i)}. \tag{4.37}$$

Due to $\lim_{k\to\infty} h = 0$ the limit (4.37) is obtained by

$$\lim_{k\to\infty} \frac{a_i}{a_m} = \lim_{k\to\infty} \frac{h(w_i)}{h(w_m)} \tag{4.38}$$

$$= \lim_{k\to\infty} \exp(-k(w_i - w_m)), \tag{4.39}$$

which yields 0 for $w_i > w_m,\ i \neq m$, which in fact is our initial assumption. We are left with

$$\lim_{k\to\infty} \frac{\delta}{a_m} = 0. \tag{4.40}$$

Due to $\sum_{i=1}^{n} a_i = 1$, and $\lim_{k\to\infty} (a_i/a_m) = 0$ for $i \neq m$, $a_m = 1$ must hold, which finally yields

$$\lim_{k\to\infty} \delta = 0 \quad \Leftrightarrow \quad \lim_{k\to\infty} \tilde{w} = \min_{i=1\ldots n} (w_1, w_2, \ldots w_n). \tag{4.41}$$

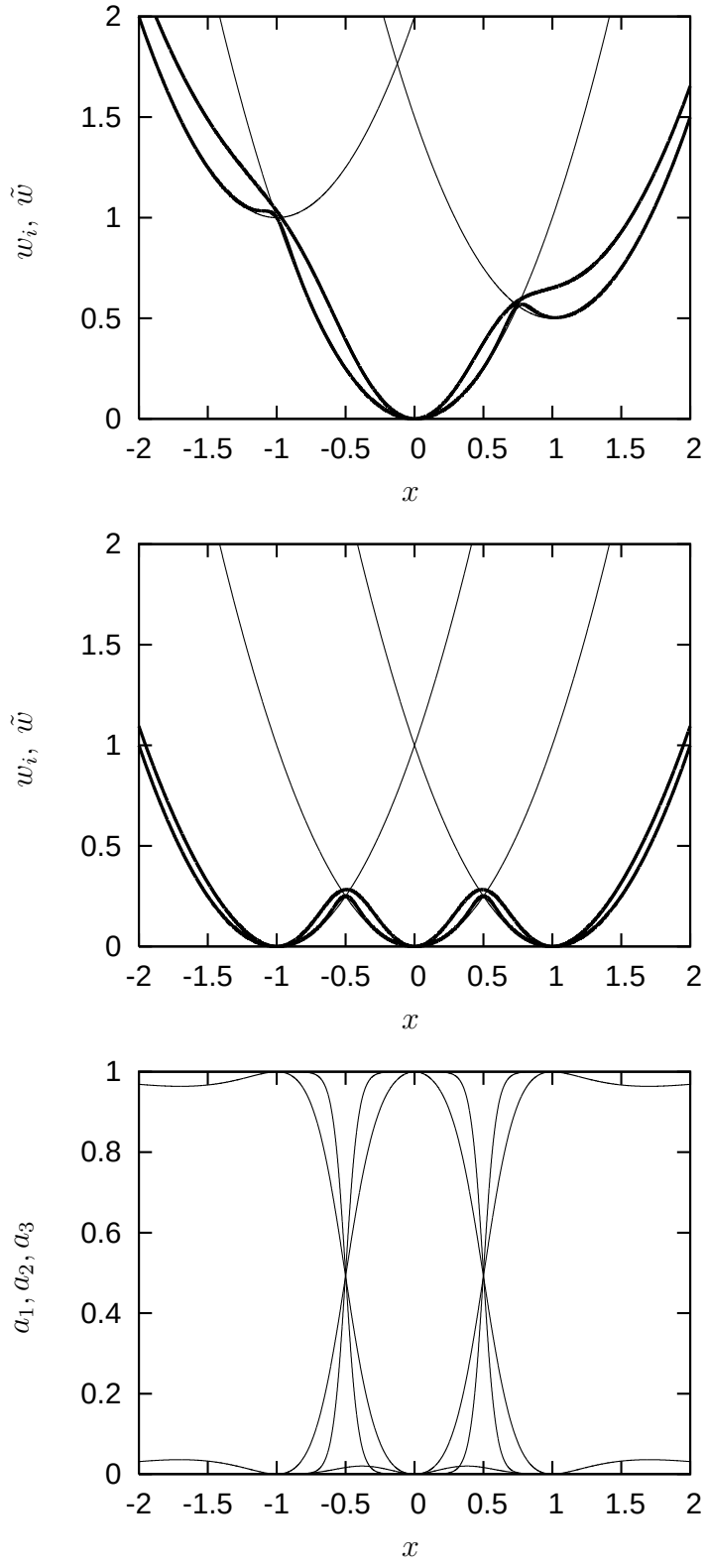

Figure 4.6: Regularisation (bold lines) applied to $w_1 = x^2$, $w_2 = (x-1)^2 + 0.5$, $w_3 = (x+1)^2 + 1$ (top) and $w_1 = x^2$, $w_2 = (x-1)^2$, $w_3 = (x+1)^2$ (centre), with $k = 1$ and $k = 10$. In the second case, as all w_i have zero as minimum, the regularisation transfers the minima of the w_i to w irrespective of k. Bottom: Weight factors a_i for $k = 1$ and $k = 10$. The transition from one $a_i = 1$ to another $a_j = 1$ becomes sharper as k grows.

4.5 The Individual Strain Energies

Now that a regularisation of eq. (4.19) is given, we focus on the individual strain energies w_i. The widely used principle of Euclidean invariance (Bertram, 2005) demands that the strain energy density w_i depends only on the material stretching, but not on a superimposed rigid body motion.

Consequently, it is sufficient to note $w_i(\boldsymbol{C})$ instead of $w_i(\boldsymbol{F})$ (Truesdell and Noll, 1965), with $\boldsymbol{C} = \boldsymbol{F}^T\boldsymbol{F}$ and the deformation gradient $\boldsymbol{F}$. The elastic material behaviour of most crystals can be described sufficiently well by a linear stress-strain relation. Therefore, the St. Venant-Kirchhoff strain energy will be employed here. The elastic reference strain energy is given by

$$w_0(\boldsymbol{C}) = \frac{1}{2}\boldsymbol{T} \cdot\cdot\, \boldsymbol{E} \tag{4.42}$$

$$= \frac{1}{8}(\boldsymbol{C}-\boldsymbol{I}) \cdot\cdot\, \mathbb{C}_0 \cdot\cdot\, (\boldsymbol{C}-\boldsymbol{I}), \tag{4.43}$$

with the stiffness tetrad $\mathbb{C}_0$. The second Piola-Kirchhoff stresses $\boldsymbol{T}$ and Green's strains $\boldsymbol{E} = \frac{1}{2}(\boldsymbol{C}-\boldsymbol{I})$ are work-conjugate, which simplifies the formulation of w_0 and its derivatives with respect to $\boldsymbol{E}$ (Hill, 1968).

4.6 Isomorphy of the Elastic Law

Due to the fact that the twinned crystal has the same crystallographic structure as the parent crystal, essentially the same elastic energy applies. Therefore, the concept of elastic isomorphisms (Bertram, 2003) is used in order to map the same elastic reference energy (4.43) to the parent and to the twin. By using the plastic transformation $\boldsymbol{P}_i$, the elastic energy can be transformed by

$$w_i(\boldsymbol{C}) = w_0(\boldsymbol{P}_i^T\boldsymbol{C}\boldsymbol{P}_i) \tag{4.44}$$

to the elastic energy of the i^{th} twin variant, where $\boldsymbol{P}_i$ maps lattice reference basis $\boldsymbol{c}_b$ into the reference placement of the parent or the ith twin variant. The second Piola-Kirchhoff-stresses are given by

$$\boldsymbol{T}_i = \frac{\partial w_i}{\partial \boldsymbol{E}} \tag{4.45}$$

$$= 2\frac{\partial w_i}{\partial \boldsymbol{C}} \tag{4.46}$$

$$= 2\frac{\partial w_0(\boldsymbol{P}_i^T\boldsymbol{C}\boldsymbol{P}_i)}{\partial(\boldsymbol{P}_i^T\boldsymbol{C}\boldsymbol{P}_i)} \cdot\cdot\, \frac{\partial \boldsymbol{P}_i^T\boldsymbol{C}\boldsymbol{P}_i}{\partial \boldsymbol{C}} \tag{4.47}$$

$$= 2\boldsymbol{P}_i w_0'(\boldsymbol{P}_i^T\boldsymbol{C}\boldsymbol{P}_i)\boldsymbol{P}_i^T. \tag{4.48}$$

In the following Section, the plastic transformations are derived.

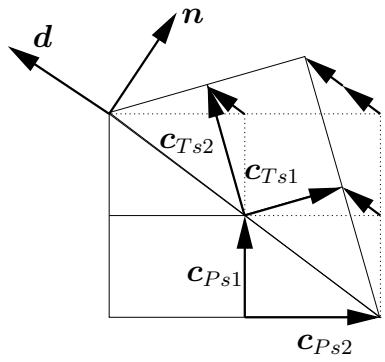

Figure 4.7: In the spatial description, the lattice vectors of parent and twin differ by a rotation of π around $\boldsymbol{n}$. The associated deformation is a simple shear.

4.7 The Elastic Isomorphisms

The plastic transformations $\boldsymbol{P}_P$ and $\boldsymbol{P}_T$ map the reference lattice basis $\boldsymbol{c}_b$ into the reference placement, either into the parent ($\boldsymbol{c}_{Pb}$) or the twin ($\boldsymbol{c}_{Tb}$),

$$\boldsymbol{c}_{Pb} = \boldsymbol{P}_P \boldsymbol{c}_b \tag{4.49}$$
$$\boldsymbol{c}_{Tb} = \boldsymbol{P}_T \boldsymbol{c}_b. \tag{4.50}$$

The spatial lattice base vectors $\boldsymbol{c}_{Ps}$ and $\boldsymbol{c}_{Ts}$ are given by the deformation gradients $\boldsymbol{F}_P$ and $\boldsymbol{F}_T$,

$$\boldsymbol{c}_{Ps} = \boldsymbol{F}_P \boldsymbol{c}_{Pb}, \tag{4.51}$$
$$\boldsymbol{c}_{Ts} = \boldsymbol{F}_T \boldsymbol{c}_{Tb}. \tag{4.52}$$

$\boldsymbol{c}_{Ps}$ and $\boldsymbol{c}_{Ts}$ are related by

$$\boldsymbol{c}_{Ts} = \boldsymbol{R} \boldsymbol{c}_{Ps}, \tag{4.53}$$

where, in compound twins, $\boldsymbol{R}$ can be taken as $\boldsymbol{R}_{\boldsymbol{n}}$ or $\boldsymbol{R}_{\boldsymbol{d}}$ (see Fig. 4.7). Now one can evaluate the plastic transformation $\boldsymbol{P}_T$ by means of

$$\begin{aligned}
\boldsymbol{P}_T \boldsymbol{c}_b &= \boldsymbol{c}_{Tb} && (4.54)\\
&= \boldsymbol{F}_T^{-1} \boldsymbol{c}_{Ts} && (4.55)\\
&= \boldsymbol{F}_T^{-1} \boldsymbol{R} \boldsymbol{c}_{Ps} && (4.56)\\
&= \boldsymbol{F}_T^{-1} \boldsymbol{R} \boldsymbol{F}_P \boldsymbol{c}_{Pb} && (4.57)\\
&= \boldsymbol{F}_T^{-1} \boldsymbol{R} \boldsymbol{F}_P \boldsymbol{P}_P \boldsymbol{c}_b && (4.58)
\end{aligned}$$

which allows for the identification

$$\boldsymbol{P}_T = \boldsymbol{F}_T^{-1} \boldsymbol{R} \boldsymbol{F}_P \boldsymbol{P}_P. \tag{4.59}$$

By taking the elastic law of the parent to be the reference law and the placement of the parent to be the reference placement,

$$\boldsymbol{P}_P = \boldsymbol{I}, \quad \boldsymbol{F}_P = \boldsymbol{I}, \tag{4.60}$$

eq. (4.59) simplifies to

$$\boldsymbol{P}_T = \boldsymbol{F}_T^{-1}\boldsymbol{R}. \tag{4.61}$$

$\boldsymbol{F}_T$ describes the deformation from the parent to the twin configuration, which is given by a simple shear deformation

$$\boldsymbol{F}_T = \boldsymbol{I} + \gamma_0 \boldsymbol{d} \otimes \boldsymbol{n}. \tag{4.62}$$

Due to the orthogonality of $\boldsymbol{d}$ and $\boldsymbol{n}$, its inverse is given by $\boldsymbol{F}_T^{-1} = \boldsymbol{I} - \gamma_0 \boldsymbol{d} \otimes \boldsymbol{n}$, which finally yields

$$\begin{aligned} \boldsymbol{P}_{T(\boldsymbol{n})} &= (\boldsymbol{I} - \gamma_0 \boldsymbol{d} \otimes \boldsymbol{n})(-\boldsymbol{I} + 2\boldsymbol{n} \otimes \boldsymbol{n}) && (4.63)\\ &= -\boldsymbol{I} - \gamma_0 \boldsymbol{d} \otimes \boldsymbol{n} + 2\boldsymbol{n} \otimes \boldsymbol{n} && (4.64) \end{aligned}$$

in the case of $\boldsymbol{R} = \boldsymbol{R}_{\boldsymbol{n}}$ and

$$\begin{aligned} \boldsymbol{P}_{T(\boldsymbol{d})} &= (\boldsymbol{I} - \gamma_0 \boldsymbol{d} \otimes \boldsymbol{n})(-\boldsymbol{I} + 2\boldsymbol{d} \otimes \boldsymbol{d}) && (4.65)\\ &= -\boldsymbol{I} + \gamma_0 \boldsymbol{d} \otimes \boldsymbol{n} + 2\boldsymbol{d} \otimes \boldsymbol{d} && (4.66) \end{aligned}$$

in the case of $\boldsymbol{R} = \boldsymbol{R}_{\boldsymbol{d}}$. In both cases, $\boldsymbol{P}_T$ has the remarkable property of self-inverseness, $\boldsymbol{P}_T = \boldsymbol{P}_T^{-1}$. Therefore, double twinning on the same twin system results in a recovery of the parent (see Section 2.2).

4.8 Conjugate Twin Systems

In any compound twin defined by rational $\boldsymbol{k}_1, \boldsymbol{k}_2, \boldsymbol{\eta}_1, \boldsymbol{\eta}_2$ there exist two conjugate twin systems. These are given by shearing in direction of $\boldsymbol{\eta}_1$ parallel to $\boldsymbol{k}_1$ such that $\boldsymbol{k}_2$ is turned over, and shearing along $\boldsymbol{\eta}_2$ parallel to $\boldsymbol{k}_2$ such that $\boldsymbol{k}_1$ is turned over. The second undistorted plane of one twinning mode is the shear plane of the other one, and vice versa, see Fig. 4.8 for a sketch. In the remainder of this section, $\boldsymbol{d}^*$ and $\boldsymbol{n}^*$ denote the conjugate twinning mode to the twinning mode $\boldsymbol{d}$ and $\boldsymbol{n}$. For the conjugate twin systems,

$$\boldsymbol{S}^* \boldsymbol{S}^{-1} = \boldsymbol{Q}_{\beta \boldsymbol{k}}^T \tag{4.67}$$

holds, where β and γ_0 are connected by $\gamma_0 = 2\tan(\beta/2)$ and $\boldsymbol{k} = \boldsymbol{n} \times \boldsymbol{d}$. To see this, one has to summarise $\boldsymbol{S}^* \boldsymbol{S}^{-1}$ by representing $\boldsymbol{d}^*$ and $\boldsymbol{n}^*$ in terms of $\boldsymbol{d}$ and $\boldsymbol{n}$. Apparently, one has to distinguish two cases, namely $\angle(\boldsymbol{n}, \boldsymbol{n}^*) < \pi/2$ (Fig. 4.8 left, case 1) and $\angle(\boldsymbol{n}, \boldsymbol{n}^*) > \pi/2$, (Fig. 4.8 right, case 2). One obtains

$$\begin{aligned} \boldsymbol{d}_1^* &= -\sin(\beta/2)\boldsymbol{d} + \cos(\beta/2)\boldsymbol{n} && (4.68)\\ \boldsymbol{n}_1^* &= \cos(\beta/2)\boldsymbol{d} + \sin(\beta/2)\boldsymbol{n} && (4.69) \end{aligned}$$

and

$$\begin{aligned} \boldsymbol{d}_2^* &= \sin(\beta/2)\boldsymbol{d} - \cos(\beta/2)\boldsymbol{n} && (4.70)\\ \boldsymbol{n}_2^* &= -\cos(\beta/2)\boldsymbol{d} - \sin(\beta/2)\boldsymbol{n}, && (4.71) \end{aligned}$$

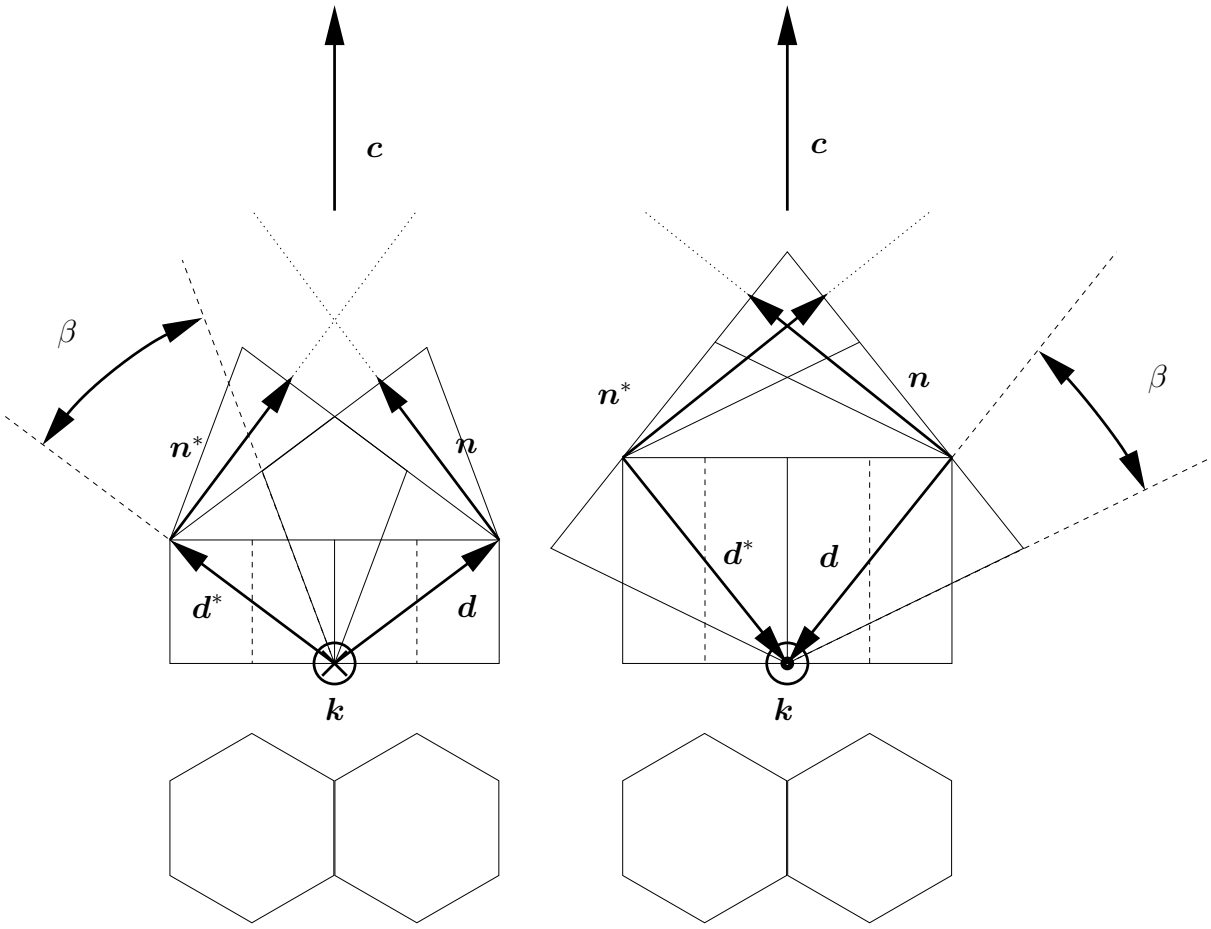

Figure 4.8: Conjugate twin systems $(\boldsymbol{d}, \boldsymbol{n}, \gamma_0)$ and $(\boldsymbol{d}^*, \boldsymbol{n}^*, \gamma_0)$ in the hexagonal unit cell, with $c/a < \sqrt{3}$ (left) and $c/a < \sqrt{3}$ (right), and $\gamma_0 = 2\tan(\beta/2)$. Note that in both cases the lateral diamonds can be mapped on each other by a rotation of amount β around the axis $\boldsymbol{k} = \boldsymbol{n} \times \boldsymbol{d}$ or, alternatively, by reverse shearing in one twin system followed by shearing in the compound system.

where one notes that $\boldsymbol{n}_2^* = -\boldsymbol{n}_1^*$ and $\boldsymbol{d}_2^* = -\boldsymbol{d}_1^*$. Due to

$$\boldsymbol{S}_1^* = \boldsymbol{I} + \gamma_0 \boldsymbol{n}_1^* \otimes \boldsymbol{d}_1^* = \boldsymbol{I} + \gamma_0 \boldsymbol{n}_2^* \otimes \boldsymbol{d}_2^* = \boldsymbol{S}_2^* \tag{4.72}$$

we can drop the case distinction. For brevity, the substitution $\beta/2 = \alpha$ is used. Summarising $\boldsymbol{S}^* \boldsymbol{S}^{-1}$ by using eqs. (4.68) and (4.69) and the identity $\boldsymbol{I} = \boldsymbol{n} \otimes \boldsymbol{n} + \boldsymbol{d} \otimes \boldsymbol{d} + \boldsymbol{k} \otimes \boldsymbol{k}$ yields

$$\begin{aligned}
\boldsymbol{S}^* \boldsymbol{S}^{-1} =& (\boldsymbol{I} + \gamma_0 \boldsymbol{d}^* \otimes \boldsymbol{n}^*)(\boldsymbol{I} - \gamma_0 \boldsymbol{d} \otimes \boldsymbol{n}) && (4.73)\\
=& \boldsymbol{I} - \gamma_0 \boldsymbol{d} \otimes \boldsymbol{n} + \gamma_0 \boldsymbol{d}^* \otimes \boldsymbol{n}^* - \gamma_0^2 (\boldsymbol{n}^* \cdot \boldsymbol{d}) \boldsymbol{d}^* \otimes \boldsymbol{n} && (4.74)\\
=& \boldsymbol{I} - \gamma_0 \boldsymbol{d} \otimes \boldsymbol{n} + \gamma_0 (-\sin\alpha \boldsymbol{d} + \cos\alpha \boldsymbol{n}) \otimes (\cos\alpha \boldsymbol{d} + \sin\alpha \boldsymbol{n}) + \\
& - \gamma_0^2 \cos\alpha (-\sin\alpha \boldsymbol{d} + \cos\alpha \boldsymbol{n}) \otimes \boldsymbol{n} && (4.75)\\
=& \boldsymbol{k} \otimes \boldsymbol{k} \\
& + [-\gamma_0 - \gamma_0 \sin^2\alpha + \gamma_0^2 \sin\alpha \cos\alpha] \boldsymbol{d} \otimes \boldsymbol{n} \\
& + [\gamma_0 \cos^2\alpha] \boldsymbol{n} \otimes \boldsymbol{d} \\
& + [1 - \gamma_0 \sin\alpha \cos\alpha] \boldsymbol{d} \otimes \boldsymbol{d} \\
& + [1 + \gamma_0 \sin\alpha \cos\alpha - \gamma_0^2 \cos^2\alpha] \boldsymbol{n} \otimes \boldsymbol{n}. && (4.76)
\end{aligned}$$

With $\gamma_0 = 2\tan\alpha$ one can summarise each of the squared brackets by applying several trigonometric relations (mostly $2\sin^2(\beta/2) = 1 - \cos(\beta)$, $2\cos^2(\beta/2) = 1 + \cos(\beta)$ and $\tan\alpha \cos\alpha = \sin\alpha$). One obtains

$$\boldsymbol{S}^* \boldsymbol{S}^{-1} = \boldsymbol{k} \otimes \boldsymbol{k} + \sin(\beta)(\boldsymbol{n} \otimes \boldsymbol{d} - \boldsymbol{d} \otimes \boldsymbol{n}) + \cos(\beta)(\boldsymbol{d} \otimes \boldsymbol{d} + \boldsymbol{n} \otimes \boldsymbol{n}), \tag{4.77}$$

where one recognises the rotation of $-\beta$ around $\boldsymbol{k}$, which corresponds to $\boldsymbol{Q}_{\beta \boldsymbol{k}}^T$. Another important relation is

$$\boldsymbol{Q}_{\beta \boldsymbol{k}}^T = \boldsymbol{R}_{\boldsymbol{n}^*} \boldsymbol{R}_{\boldsymbol{k}} \boldsymbol{R}_{\boldsymbol{n}}. \tag{4.78}$$

One can review the latter relation similarly to the previous calculation. Again, the case distinction is due to

$$\boldsymbol{R}_1^* = -\boldsymbol{I} + 2\boldsymbol{n}_1^* \otimes \boldsymbol{n}_1^* = -\boldsymbol{I} + 2\boldsymbol{n}_2^* \otimes \boldsymbol{n}_2^* = \boldsymbol{R}_2^* \tag{4.79}$$

not necessary. One obtains

$$\begin{aligned}
\boldsymbol{R}_{\boldsymbol{n}^*} \boldsymbol{R}_{\boldsymbol{k}} \boldsymbol{R}_{\boldsymbol{n}} &= (-\boldsymbol{I} + 2\boldsymbol{n}^* \otimes \boldsymbol{n}^*)(-\boldsymbol{I} + 2\boldsymbol{k} \otimes \boldsymbol{k})(-\boldsymbol{I} + 2\boldsymbol{n} \otimes \boldsymbol{n}) && (4.80)\\
&= (\boldsymbol{I} - 2\boldsymbol{k} \otimes \boldsymbol{k} - 2\boldsymbol{n}^* \otimes \boldsymbol{n}^*)(-\boldsymbol{I} + 2\boldsymbol{n} \otimes \boldsymbol{n}) && (4.81)\\
&= -\boldsymbol{I} + 2\boldsymbol{k} \otimes \boldsymbol{k} + 2\boldsymbol{n} \otimes \boldsymbol{n} + 2\boldsymbol{n}^* \otimes \boldsymbol{n}^* - 4(\boldsymbol{n} \cdot \boldsymbol{n}^*) \boldsymbol{n}^* \otimes \boldsymbol{n}. && (4.82)
\end{aligned}$$

To summarise, $\boldsymbol{n}^* = \cos\alpha \boldsymbol{d} + \sin\alpha \boldsymbol{n}$ and $-\boldsymbol{I} + 2\boldsymbol{k} \otimes \boldsymbol{k} + 2\boldsymbol{n} \otimes \boldsymbol{n} = \boldsymbol{n} \otimes \boldsymbol{n} - \boldsymbol{d} \otimes \boldsymbol{d} + \boldsymbol{k} \otimes \boldsymbol{k}$ are employed, which gives

$$\begin{aligned}
\boldsymbol{R}_{\boldsymbol{n}^*} \boldsymbol{R}_{\boldsymbol{k}} \boldsymbol{R}_{\boldsymbol{n}} =& \boldsymbol{n} \otimes \boldsymbol{n} - \boldsymbol{d} \otimes \boldsymbol{d} + \boldsymbol{k} \otimes \boldsymbol{k} + 2[\cos\alpha \boldsymbol{d} + \sin\alpha \boldsymbol{n}] \otimes [\cos\alpha \boldsymbol{d} + \sin\alpha \boldsymbol{n}] + \\
& - 4\sin\alpha [\cos\alpha \boldsymbol{d} + \sin\alpha \boldsymbol{n}] \otimes \boldsymbol{n} && (4.83)\\
=& \boldsymbol{k} \otimes \boldsymbol{k} + (1 - 2\sin^2\alpha) \boldsymbol{n} \otimes \boldsymbol{n} + (-1 + 2\cos^2\alpha) \boldsymbol{d} \otimes \boldsymbol{d} + \\
& - 2\sin\alpha\cos\alpha \boldsymbol{d} \otimes \boldsymbol{n} + 2\sin\alpha\cos\alpha \boldsymbol{n} \otimes \boldsymbol{d}. && (4.84)
\end{aligned}$$

Summarising and using trigonometric relations yields

$$\boldsymbol{R_{n^*}R_kR_n} = \boldsymbol{k}\otimes\boldsymbol{k} + \sin(\beta)(\boldsymbol{n}\otimes\boldsymbol{d} - \boldsymbol{d}\otimes\boldsymbol{n}) + \cos(\beta)(\boldsymbol{d}\otimes\boldsymbol{d} + \boldsymbol{n}\otimes\boldsymbol{n}), \tag{4.85}$$

which corresponds again to $\boldsymbol{Q}^T_{\beta\boldsymbol{k}}$.

Following eq. (4.61) the plastic transformations of conjugate twin systems are

$$\boldsymbol{P} = \boldsymbol{S}^{-1}\boldsymbol{R_n}, \qquad \boldsymbol{P}^* = \boldsymbol{S}^{*-1}\boldsymbol{R_{n^*}}, \tag{4.86}$$

where the orientation relation $\boldsymbol{R} = \boldsymbol{R_n}$ has been chosen. After establishing the result, it is shown that the result holds for $\boldsymbol{R} = \boldsymbol{R_d}$ as well. Mapping an elastic reference energy w_0 with the plastic transformations yields

$$w = w_0(\boldsymbol{P}^T\boldsymbol{C}\boldsymbol{P}), \qquad w^* = w_0(\boldsymbol{P}^{*T}\boldsymbol{C}\boldsymbol{P}^*), \tag{4.87}$$

or, by means of the Rayleigh product,

$$w = w_0(\boldsymbol{P}^T * \boldsymbol{C}), \qquad w^* = w_0(\boldsymbol{P}^{*T} * \boldsymbol{C}). \tag{4.88}$$

By substituting $\boldsymbol{C} = \boldsymbol{P}^{*-T} * \tilde{\boldsymbol{C}}$ we get

$$w = w_0((\boldsymbol{P}^T\boldsymbol{P}^{*-T}) * \tilde{\boldsymbol{C}}), \qquad w^* = w_0(\tilde{\boldsymbol{C}}). \tag{4.89}$$

We now examine

$$\boldsymbol{P}^T\boldsymbol{P}^{*-T} = \boldsymbol{R_n}\boldsymbol{S}^{-T}\boldsymbol{S}^{*T}\boldsymbol{R_{n^*}}. \tag{4.90}$$

With eqs. (4.67) and (4.78) we can summarise

$$\begin{aligned}\boldsymbol{P}^T\boldsymbol{P}^{*-T} &= \boldsymbol{R_n}\boldsymbol{Q}_{\beta\boldsymbol{k}}\boldsymbol{R_{n^*}} &(4.91)\\ &= \boldsymbol{R_n}\boldsymbol{R_n}\boldsymbol{R_k}\boldsymbol{R_{n^*}}\boldsymbol{R_{n^*}} &(4.92)\\ &= \boldsymbol{R_k}. &(4.93)\end{aligned}$$

Now, if we prefer $\boldsymbol{R} = \boldsymbol{R_d}$ as orientation relation, we obtain

$$\boldsymbol{P}^T\boldsymbol{P}^{*-T} = \boldsymbol{R_d}\boldsymbol{Q}_{\beta\boldsymbol{k}}\boldsymbol{R_{d^*}}, \tag{4.94}$$

which can be rewritten by $\boldsymbol{R_d} = \boldsymbol{R_k}\boldsymbol{R_n}$ and $\boldsymbol{R_{d^*}} = \boldsymbol{R_{n^*}}\boldsymbol{R_k}$ as

$$\begin{aligned}\boldsymbol{P}^T\boldsymbol{P}^{*-T} &= \boldsymbol{R_k}\boldsymbol{R_n}\boldsymbol{Q}_{\beta\boldsymbol{k}}\boldsymbol{R_{n^*}}\boldsymbol{R_k} &(4.95)\\ &= \boldsymbol{R_k}\boldsymbol{R_k}\boldsymbol{R_k} = \boldsymbol{R_k}. &(4.96)\end{aligned}$$

We have seen in Section 2.2 that the $\boldsymbol{R_k}$ belonging to a compound twinning mode must be in the symmetry group of the lattice. Therefore, the elastic reference energy w_0 must have $\boldsymbol{R_k}$ in its symmetry group. In this section it is shown that the strain energies w and w^* of conjugate twin systems differ by a Rayleigh transformation of $\boldsymbol{C}$ with $\boldsymbol{R_k}$. By combining both, one has to conclude that compound twin systems exhibit an elastic energy invariance, i.e. $w = w^*$, and consequently, $\partial w/\partial\boldsymbol{E} = \boldsymbol{T} = \boldsymbol{T}^*$ holds.

Depending on the twinning mode, distinct conclusions have to be drawn. In the case that the pairs ($\boldsymbol{d}$, $\boldsymbol{d}^*$) and ($\boldsymbol{n}$, $\boldsymbol{n}^*$) are crystallographically equivalent (or, in the usual twinning notation, ($\boldsymbol{\eta}_1$, $\boldsymbol{\eta}_2$) and ($\boldsymbol{k}_1$, $\boldsymbol{k}_2$)), the conjugate twinning modes belong to a set of crystallographically equivalent twin systems. Practical examples are the $\{112\}\langle\bar{1}\bar{1}1\rangle$ twinning in the bcc, $\{111\}\langle 11\bar{2}\rangle$ twinning in the fcc, $\{01\bar{1}2\}\langle 0\bar{1}11\rangle$ twinning in hcp, $\{101\}\langle 10\bar{1}\rangle$ twinning in the bct and orthorhombic and $\{100\}\langle 00\bar{1}\rangle$ twinning in the orthorhombic lattice. For example, for one of the $\{01\bar{1}2\}\langle 0\bar{1}11\rangle$ twin systems in the hcp lattice, $\boldsymbol{k}_1, \boldsymbol{\eta}_1, \boldsymbol{k}_2, \boldsymbol{\eta}_2$ are $\{01\bar{1}2\}, \langle 0\bar{1}11\rangle, \{01\bar{1}\bar{2}\}, \langle 01\bar{1}1\rangle$, respectively, see Fig. 4.8. This means that the conjugate twin to the $\{01\bar{1}2\}\langle 0\bar{1}11\rangle$ twin system is crystallographically equivalent, i.e. one has six crystallographically equivalent twin systems. These are pairwise energetically invariant, which means that from the viewpoint of an elastic modelling, one can only distinguish three possible twinning modes.

In the case when the pairs ($\boldsymbol{d}$, $\boldsymbol{d}^*$) and ($\boldsymbol{n}$, $\boldsymbol{n}^*$) are crystallographically distinct, different conclusions emerge. Practical examples are $\{01\bar{1}1\}\langle 01\bar{1}\bar{2}\rangle$ and $\{11\bar{2}2\}\langle 11\bar{2}3\rangle$ twinning in the hcp lattice, $\{031\}\langle 0\bar{1}3\rangle$ twinning in the bct lattice, $\{100\}\langle 0\bar{1}\bar{1}\rangle$ twinning in the rhombohedral lattice, $\{10\bar{1}\}\langle 1\kappa_1 1\rangle$ and $\{130\}\langle 3\bar{1}0\rangle$ twinning in the orthorhombic lattice and $\{100\}\langle 001\rangle$, $\{110\}\langle 00\bar{1}\rangle$, $\{100\}\langle 0\kappa_2\kappa_3\rangle$ and $\{011\}\langle 0\kappa_4\kappa_5\rangle$ twinning in the monoclinic lattice, where κ_i denotes some lattice constant. For example, for the $\{01\bar{1}1\}\langle 01\bar{1}\bar{2}\rangle$ twin systems in the hcp lattice, $\boldsymbol{k}_1, \boldsymbol{\eta}_1, \boldsymbol{k}_2, \boldsymbol{\eta}_2$ are $\{01\bar{1}1\}, \langle 01\bar{1}\bar{2}\rangle, \{01\bar{1}\bar{3}\}, \langle 03\bar{3}2\rangle$, respectively. This means that the conjugate twin to the $\{01\bar{1}1\}\langle 01\bar{1}\bar{2}\rangle$ twin system, which is the $\{01\bar{1}\bar{3}\}\langle 03\bar{3}2\rangle$ twin system, is crystallographically distinct, see Fig. 4.9. Therefore, it may display different characteristics, like different critical shear stresses. Both twin systems are, however, connected by the elastic energy invariance. By introducing an elastic energy density which displays the six distinct minima of the $\{10\bar{1}1\}\langle 10\bar{1}\bar{2}\rangle$ twin variants, one enables automatically $\{10\bar{1}\bar{3}\}\langle 30\bar{3}2\rangle$ twinning.

The strain energy invariance may even connect a twinning mode to a lattice invariant shear, namely to a deformation which one would consider as crystallographic glide. An example is twinning with the elements $\boldsymbol{k}_1 = \{120\}$, $\boldsymbol{\eta}_1 = \langle 2\bar{1}0\rangle$, $\boldsymbol{k}_2 = \{100\}$ and $\boldsymbol{\eta}_2 = \langle 010\rangle$ in a simple cubic lattice, see Fig. 4.10 for a sketch. One notes that $\boldsymbol{k}_2$ and $\boldsymbol{\eta}_2$ correspond to the lattice base vectors, and that a „reorientation" by a two fold rotation around $\boldsymbol{k}_2$ or $\boldsymbol{\eta}_2$ maps the lattice onto itself. This means that shearing in the shear system $\boldsymbol{\eta}_2 \otimes \boldsymbol{k}_2$ should be considered as slip, not as twinning. Due to the strain-energy invariance, one incorporates an impossible twinning mode if one constructs w such that $w = 0$ holds for the $\{120\}\langle 2\bar{1}0\rangle$ twins, which are valid twin configurations.

The non-compound twinning modes, type 1 and type 2 twinning, do not exhibit the energy invariance, since $\boldsymbol{R}_{\boldsymbol{k}}$ is not an element of the symmetry group of the lattice. Therefore, w_0 is not invariant under a symmetry transformation with $\boldsymbol{R}_{\boldsymbol{k}}$, as long as a proper elastic law is applied.

The latter conclusions are important, and therefore their derivation is roughly summarised: The $\boldsymbol{R}_{\boldsymbol{k}}$ belonging to compound twins is in the lattice symmetry group (Section 2.2). Also, their twin systems are conjugate. The conjugacy of the twin systems is induced by their alignment: shear occurs mutually along the distinguished plane that is left unstretched by shearing in the other system, but is only turned over. Starting from a twin configuration, backward twinning into the parent configuration and subsequent twinning into the conjugate twin system can be replaced by a rotation of β around the plane of shear normal $\boldsymbol{k}$, see Fig. 4.9 for an illustration. In this section it is shown that the elastic energy densities of conjugate twin systems differ by a Rayleigh transformation of $\boldsymbol{C}$ with $\boldsymbol{R}_{\boldsymbol{k}}$. Combining both yields the aforementioned conclusions.

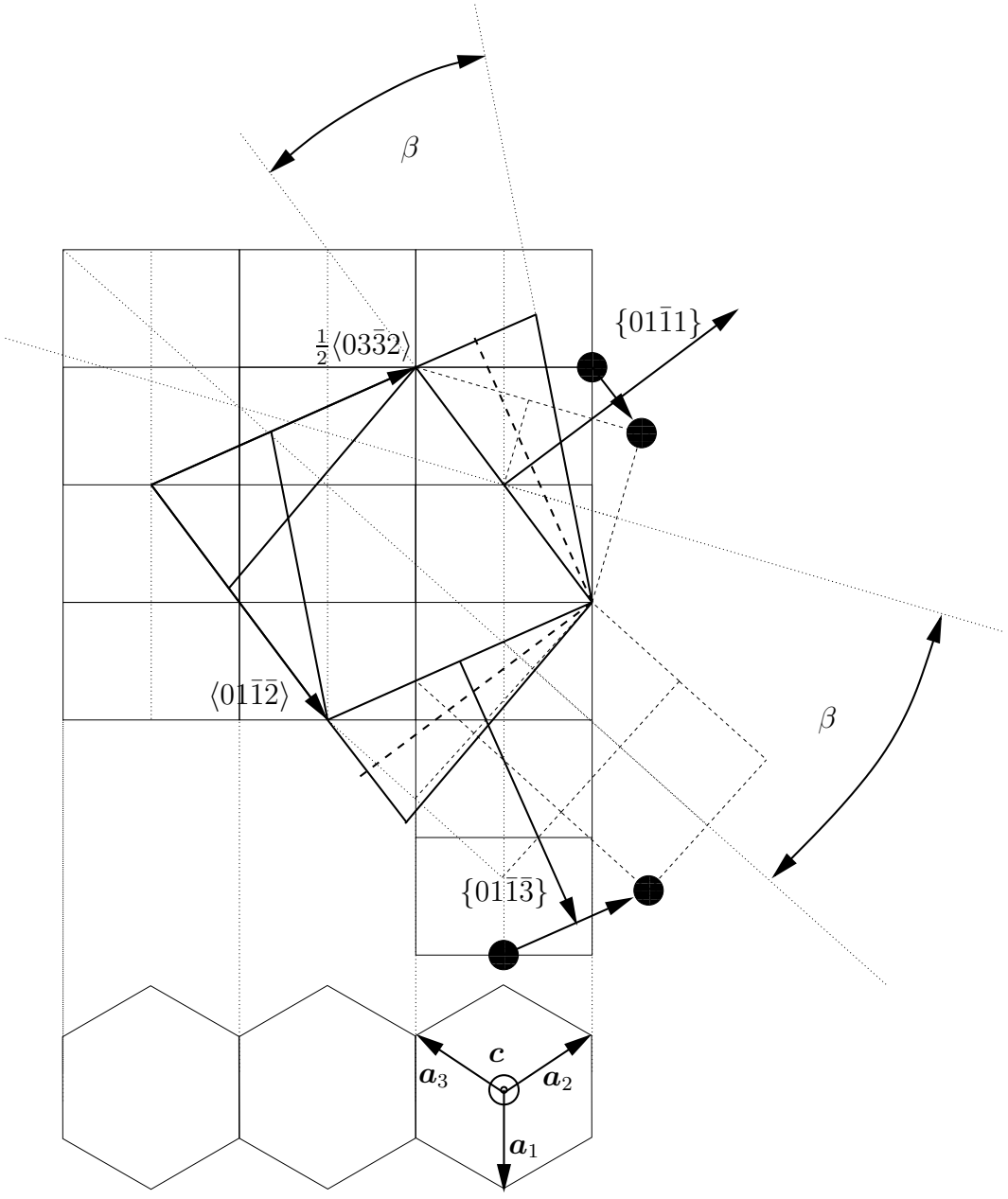

Figure 4.9: The $\{01\bar{1}1\}\langle 01\bar{1}\bar{2}\rangle$ and the $\{10\bar{1}\bar{3}\}\langle 03\bar{3}2\rangle$ twin system in the hcp lattice.

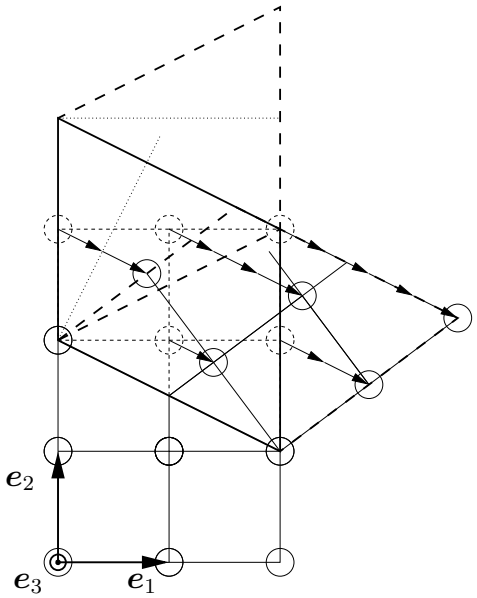

Figure 4.10: A lattice invariant shear ($\boldsymbol{d} \parallel \boldsymbol{e}_2,\ \boldsymbol{n} \parallel \boldsymbol{e}_1$) and a twinning mode ($\boldsymbol{d} \parallel (2\boldsymbol{e}_1 - \boldsymbol{e}_2),\ \boldsymbol{n} \parallel (\boldsymbol{e}_1 + 2\boldsymbol{e}_2)$) that are connected by the conjugacy of the shear systems.

The cause for the energy invariance has been shown in a more general way by Zanzotto (1992, 1996) to be the violation of the Cauchy-Born rule (Born and Huang, 1954). During twinning, the lattice vectors do not behave like material vectors due to the rearrangement of the atoms. One has to pay special attention to conjugate twin systems, especially when purely energetic considerations are made.

It should be mentioned that material models that relate the stress state to the twin system activity, e.g., by a Schmid law (Forest and Parisot, 2000), are less difficult with respect to conjugate twin systems. This comes from the fact that such a relation involves the spatial arrangement of the lattice vectors, which results in different resolved shear stresses in the conjugate twin systems.

The six possible twin variants belonging to the prominent $\{01\bar{1}2\}\langle 0\bar{1}11\rangle$ twinning mode are found in the hcp crystals of Be, Cd, Mg, Ti, Zr, Zn (Pitteri and Zanzotto, 2002) and in low-symmetry crystals with a hexagonal sublattice (e.g. sapphire). They consist of 3 pairs of crystallographically equivalent conjugate twin systems, which means that incorporating them into w_0 does not involve twinning modes which are not aimed for. For this twinning mode, $\boldsymbol{R_k}$ corresponds to $\boldsymbol{R_{a_i}}$, which maps the hexagonal unit cell onto itself. w_0 is therefore unaltered, which is manifested in linear elasticity by the fact that $\mathbb{C}_0$ has $\boldsymbol{R_k}$ in its symmetry group. Note that $\boldsymbol{S}, \boldsymbol{S}^*, \boldsymbol{R_n}, \boldsymbol{R_{n^*}}, \boldsymbol{R_d}, \boldsymbol{R_{d^*}}$ are also invariant under a Rayleigh transformation with $\boldsymbol{R_k}$.

4.8.1 Implications for the Elastic Modelling

The practical implications for the material model presented here are the pairwise energy invariances of the six twin systems. Therefore, we have to speak about three distinguishable twinning modes, each one constituted by two conjugate twin systems. The consequences are that a fully developed twin may switch its interface alignment instantaneously to its conjugate twin without altering the internal energy, if both variants are equally accomodated inside the matrix. This will be demonstrated later on. Zanzotto (1992, 1996) and Ericksen (2000) therefore doubt that twinning can be simulated by an

elasticity model. However, this behaviour is due to the fact that the modelling is fully elastic. The fact that an energy invariance between conjugate twin systems exists, solely triggers the switching between twinning modes, but the switching itself is possible in principle irrespective of the energy invariance. It is induced by the elastic modelling, which neglects the kinetic processes accompanying twinning. Although the latter sounds discouraging, it will be demonstrated that, if no severe strain path changes occur, the elastic modelling works sufficiently well. The conjugate twins cannot be distinguished if one focuses on a material point, but by the alignment of the interfaces that evolve. However, if one intends to model, e.g., double twinning or slip system activity inside the twin, one needs to know the lattice orientation inside the twin, which is not uniquely determined due to the energy invariance.

The model exhibits different critical strain state definitions in the parent and the twin configurations. Therefore, the attentive reader may note that the energy invariance cannot be entirely fulfilled by the model, at least in the overcritical strain regions. The different critical strain state definitions are owed to the fact that one cannot map the twin formation possibilities of the parent to the twins, because this would induce an infinite chain of twin variants. One would have to simultaneously respect infinitely many individual strain energies in the compound strain energy $\tilde{w} = a_i w_i$. Moreover, the direct establishment of twins which are only accessible by multiple twinning has to be avoided, see Fig. 4.11. For this reason, the model is constructed such that only twinning and detwinning with respect to the $\{\bar{1}012\}\langle\bar{1}011\rangle$ twinning modes is possible, and multiple (recursive) twinning needs to be avoided.

In the model, the conjugate twin variants are treated individually, and not as one twinning mode. Due to the phenomenological model adaptation, the energy invariance is not exactly met. This, however, does not induce spurious consequences. The energy invariance does not induce a special material property that needs to be reflected by the model. Rather, the energy invariance induces material behaviour that is not observed experimentally.

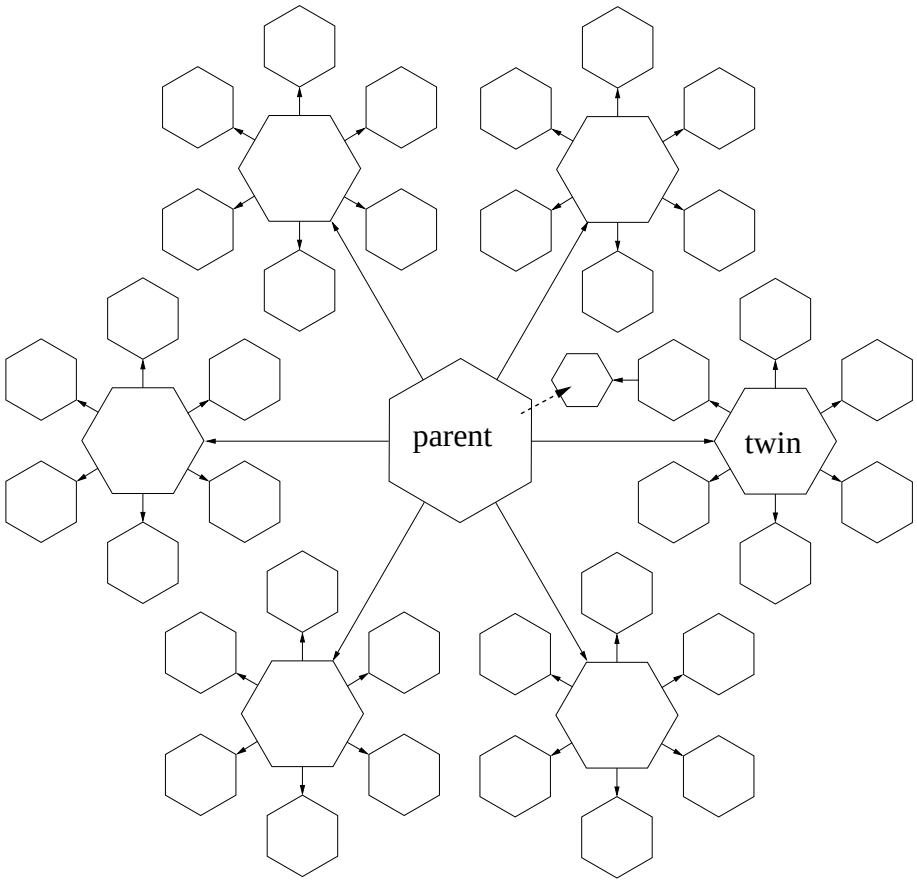

Figure 4.11: Illustration of the recursive character of twinning. Each twin, since it exhibits the crystallographic structure of the parent, may act as parent for further twinning. Incorporating simultaneously all possible twin variants would allow for twin formation following the dashed arrow, which is not reasonable.

4.9 Constitutive Equations of the Base Model

With the regularisation of the Ball and James approach and the individual strain energies at hand, the stress-strain relation so far is given by

$$\boldsymbol{T} = \frac{\partial w}{\partial \boldsymbol{E}} = \frac{\partial a_i w_i}{\partial \boldsymbol{E}} \tag{4.97}$$

$$= \frac{\partial a_i}{\partial \boldsymbol{E}} w_i + a_i \frac{\partial w_i}{\partial \boldsymbol{E}} \tag{4.98}$$

$$= \frac{\partial a_i}{\partial w_j} \frac{\partial w_j}{\partial \boldsymbol{E}} w_i + a_i \frac{\partial w_i}{\partial \boldsymbol{E}}, \tag{4.99}$$

with

$$\frac{\partial a_i}{\partial w_j} = \frac{(\delta_{ij} - a_i) a_j}{h(w_j) - h(w_j)^2} h'(w_j), \quad h(w_j) = \exp(-k w_j), \quad h(w_j)' = -k \exp(-k w_j) \tag{4.100}$$

$$\frac{\partial w_i}{\partial \boldsymbol{E}} = \boldsymbol{T}_i. \tag{4.101}$$

After summing up, the stress strain relation becomes

$$\boldsymbol{T} = \frac{(a_i - \delta_{ij}) a_j k w_i}{1 - \exp(-k w_j)} \boldsymbol{T}_j + a_i \boldsymbol{T}_i \tag{4.102}$$

where i and j are summation indices. Near the stress-free configuration of phase i, w_i tends to zero, and a_i tends to 1, while $a_j,\ i \neq j$ tend as well to zero. By looking eq. (4.102) it becomes clear that in this case all the summands represented by the first term are zero, which allows to approximate stress-strain relation by

$$\boldsymbol{T} \approx a_i \boldsymbol{T}_i. \tag{4.103}$$

We have seen that the regularisation picks out the smallest strain energy w_i by $a_i = 1$ as k tends to infinity. Consequently, for a reasonable choice of k the approximation (4.103) holds. The latter simplification is used instead of eq. (4.102), at the cost of the integrability condition of hyperelasticity. However, by adjusting a reasonably large regularisation parameter k, the neglected term becomes arbitrarily small. In order to get an impression of the effect of neglecting the first term, graphs for a comparison are plotted in Fig. 4.9. One notes that for larger values of k the difference between eq. (4.102) and (4.103) concentrates more at the transition points. The stress-strain characteristic is approximately the same in both cases. In the remainder, the simplification (4.103) is used.

Eq. (4.103) has a striking similarity to the calculation of the homogenised stresses when Taylor's assumption is applied. However, the characteristics of the present model are entirely different, and can be summarised as follows: The regularisation between different quadratic elastic strain energies yields a nonconvex elastic strain energy. As the material is fully elastic, the body locally returns to one of the stress free configurations of the n phases when all constraints are removed. The a_i depend on the current deformation state $\boldsymbol{C}$. In a Taylor model, the a_i are interpreted physically as volume fractions, which evolve depending on the loading path. In the present model, the a_i are elements of a regularisation, and have therefore no physical interpretation.

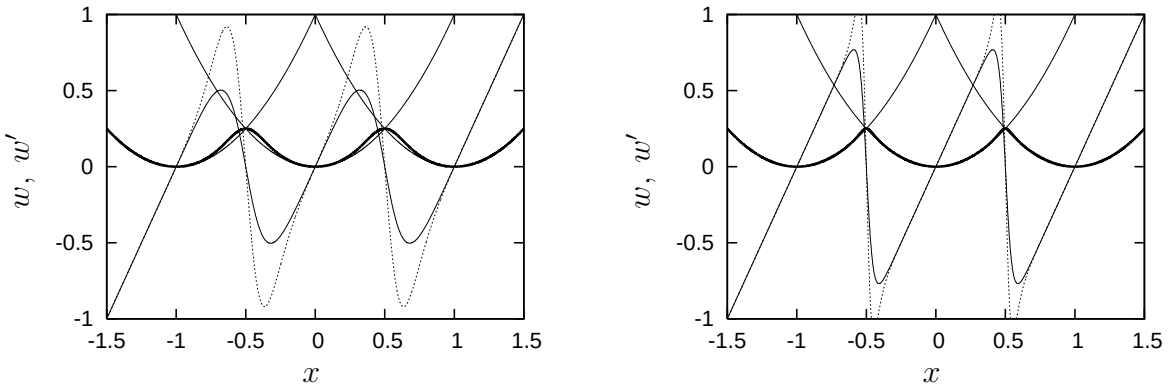

Figure 4.12: Regularisation (bold lines), its full derivative (dashed line) and the approximated derivative applied to $w_1 = x^2$, $w_2 = (x-1)^2$ and $w_3 = (x+1)^2$, with $k = 5$ (a) and $k = 20$ (b).

4.10 Incorporation of Crystallographic Glide

In magnesium below 225°C, slip occurs mainly along the $\langle \bar{2}110 \rangle$, $\langle 1\bar{2}10 \rangle$ and $\langle 11\bar{2}0 \rangle$ directions in the basal $\{0001\}$ plane (Emles, 1966). Due to the regular alignment of the slip systems in only one slip plane it is reasonable to approximate the collective of slip systems by the card glide mechanism, Fig. 4.13. It is assumed that slip occurs in the direction of the largest shear stress in the slip plane, as is

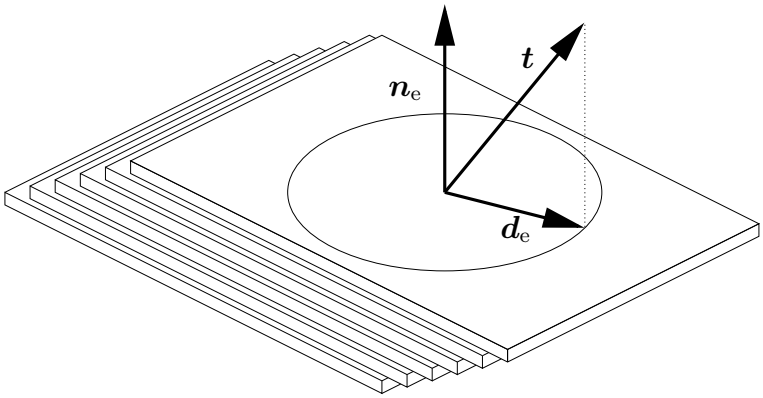

Figure 4.13: Card glide mechanism.

observed on a card deck. Following Bertram (2005); Böhlke and Bertram (2001), the shear stress is given by

$$\tau = (\tilde{\boldsymbol{F}}^T \boldsymbol{\sigma} \tilde{\boldsymbol{F}}^{-T}) \cdot\cdot (\boldsymbol{d} \otimes \boldsymbol{n}), \qquad \tilde{\boldsymbol{F}} = \boldsymbol{F}\boldsymbol{P}. \tag{4.104}$$

The direction $\boldsymbol{d}$ corresponding to the largest largest shear stress in the plane $\boldsymbol{n}$ is given by projecting the traction $\tilde{\boldsymbol{F}}^T \boldsymbol{\sigma} \tilde{\boldsymbol{F}}^{-T} \boldsymbol{n}$ into the $\boldsymbol{n}$-plane,

$$\boldsymbol{d} = (\boldsymbol{I} - \boldsymbol{n} \otimes \boldsymbol{n}) \tilde{\boldsymbol{F}}^T \boldsymbol{\sigma} \tilde{\boldsymbol{F}}^{-T} \boldsymbol{n}. \tag{4.105}$$

The evolution of the plastic transformation, which is a material variable (i.e. invariant with respect to Euclidean transformations), is given by

$$-\boldsymbol{P}^{-1}\dot{\boldsymbol{P}} = \dot{\gamma}\boldsymbol{d}^* \otimes \boldsymbol{n}, \qquad \boldsymbol{d}^* = \frac{\boldsymbol{d}}{\|\boldsymbol{d}\|}. \tag{4.106}$$

If $\boldsymbol{d}^*$ and $\boldsymbol{n}$ are constant, one obtains with $\boldsymbol{P}(t=0) = \boldsymbol{P}_0$ a solution for $\boldsymbol{P}$, namely

$$\boldsymbol{P} = \boldsymbol{P}_0(\boldsymbol{I} - \gamma \boldsymbol{d}^* \otimes \boldsymbol{n}), \tag{4.107}$$

This leaves only $\gamma(t)$ to be determined consistent with the elastic or viscoelastic law. In terms of resolved shear stresses, one has to employ $\tau_{\mathrm{el}} = \tau_{\mathrm{basal}}$. In the case of perfect plasticity, τ_{basal} is a function of γ, or, without hardening, τ_{basal} is constant. In the viscoelastic case, τ_{basal} depends on γ and $\dot{\gamma}$, or only on $\dot{\gamma}$ if hardening is ignored. In this work a perfectly plastic behaviour is preferred, since it can be resolved more easily in this quasi 1D-case. Due to the fact that the twin lamellae are mostly thin and dislocation free, basal slip is assumed to be potentially active only in the parent configuration (see, e.g., Shiekhelsouk et al. (2009)). The numerical treatment of the basal glide is explained in Section 6.2.

4.11 Adding the Viscous Regularisation

As explained in Section 4.2, in order to obtain a solvable set of constitutive equations, the elastic energy should not be convexified, but the model category is shifted from a total constitutive law to a rate-type law. This is done by adding a strain rate sensitivity to the stresses, namely the viscous contribution $\boldsymbol{T}_{\mathrm{v}}$. In the spatial description,

$$\boldsymbol{\sigma}_{\mathrm{v}} = \boldsymbol{f}(\boldsymbol{D}) \tag{4.108}$$

serves as starting point, with $\boldsymbol{D}$ being the symmetric part of the velocity gradient $\boldsymbol{L} = \dot{\boldsymbol{F}}\boldsymbol{F}^{-1}$. By assuming viscous isotropy, the viscous stresses can be decomposed into a volumetric and a distortional part

$$\boldsymbol{\sigma}_{\mathrm{v}} = \eta_1(\boldsymbol{D})\boldsymbol{D}^{\circ} + \eta_2(\boldsymbol{D})\boldsymbol{D}'. \tag{4.109}$$

There are several reasons to drop the first term. Firstly, in crystal elasticity and plasticity volume changes are very small. Secondly, a viscosity is physically induced by friction forces between particles that pass by each other, which does not happen in purely dilatational deformations of crystals. Moreover, the viscosity is added in order to regularise the material behaviour when the material undergoes the simple shear deformation connected to the twin formation, which is isochoric. Therefore, the first term in eq. (4.109) and, thus, the index of η_2 are not needed. Further, a Newtonian viscous relation is assumed,

$$\boldsymbol{\sigma}_{\mathrm{v}} = \eta \boldsymbol{D}'. \tag{4.110}$$

This is translated to the material description by using

$$\boldsymbol{\sigma}_{\mathrm{v}} = J^{-1}\boldsymbol{F}\boldsymbol{T}_{\mathrm{v}}\boldsymbol{F}^{T}, \quad J = \det(\boldsymbol{F}) \tag{4.111}$$

$$\boldsymbol{D} = \frac{1}{2}\boldsymbol{F}^{-T}\dot{\boldsymbol{C}}\boldsymbol{F}^{-1} \tag{4.112}$$

One obtains

$$\boldsymbol{T}_{\mathrm{v}} = \frac{J\eta}{2}\boldsymbol{F}^{-1}(\boldsymbol{F}^{-T}\dot{\boldsymbol{C}}\boldsymbol{F}^{-1})'\boldsymbol{F}^{-T} \tag{4.113}$$

$$= \frac{J\eta}{2}(\boldsymbol{F}^{-1}(\boldsymbol{F}^{-T}\dot{\boldsymbol{C}}\boldsymbol{F}^{-1} - \frac{1}{3}\mathrm{tr}(\boldsymbol{F}^{-T}\dot{\boldsymbol{C}}\boldsymbol{F}^{-1})\boldsymbol{I})\boldsymbol{F}^{-T}) \tag{4.114}$$

$$= \frac{J\eta}{2}(\boldsymbol{C}^{-1}\dot{\boldsymbol{C}}\boldsymbol{C}^{-1} - \frac{1}{3}\mathrm{tr}(\boldsymbol{C}^{-1}\dot{\boldsymbol{C}})\boldsymbol{C}^{-1}). \tag{4.115}$$

By using $\boldsymbol{C} \approx \boldsymbol{I}$, one can simplify the latter to

$$\boldsymbol{T}_{\mathrm{v}} = \frac{J\eta}{2}(\dot{\boldsymbol{C}} - \frac{1}{3}\mathrm{tr}(\dot{\boldsymbol{C}})\boldsymbol{I}) \tag{4.116}$$

$$= \frac{J\eta}{2}\dot{\boldsymbol{C}}'. \tag{4.117}$$

Chapter 5

Phenomenological Model Adaptation

5.1 The Schmid Law for Twinning

By means of a critical resolved shear stress criterion, a twin-parent interface moves towards the twin or the parent when a critical shear stress in the twin system is reached. Experiments indicate that the tensile stress for twinning does not depend on the hydrostatic pressure (Reed-Hill and Abbaschian, 1994), which suggests that the twins appear as a result of shear stresses. The twin boundary moves when the atoms sketched in Fig. 5.1 jump into the positions indicated by the arrows. By means of the Schmid law the twin would grow or shrink (i.e. the twin boundary would move towards the parent or the twin) if one of the inequalities

$$\tau_{\mathrm{TS,T}} \geq -\tau_{\mathrm{twin}}, \text{ shrinking of the twin if violated (arrow 1 in Fig. 5.1)} \tag{5.1}$$

$$\tau_{\mathrm{TS,P}} \leq \tau_{\mathrm{twin}}, \text{ growth of the twin if violated (arrow 2 in Fig. 5.1)} \tag{5.2}$$

is violated. $\tau_{\mathrm{TS,T}}$ and $\tau_{\mathrm{TS,P}}$ denote the resolved shear stresses in the twin system on both sides of the interface, respectively, while τ_{twin} represents a critical twinning stress. Multiplying eq. (5.2) by -1 and adding to eq. (5.1) yields

$$\tau_{\mathrm{TS,T}} - \tau_{\mathrm{TS,P}} \geq -2\tau_{\mathrm{twin}} \tag{5.3}$$

$$-\frac{1}{2}[\![\tau_{\mathrm{TS}}]\!] \leq \tau_{\mathrm{twin}}. \tag{5.4}$$

If the stress jump $[\![\boldsymbol{\sigma}]\!]$ at the static interface is known, the jump of the shear stress in the twin system can be calculated by

$$[\![\tau_{\mathrm{TS}}]\!] = [\![\boldsymbol{\sigma}]\!] \cdot\cdot (\boldsymbol{d}_{\mathrm{T}} \otimes \boldsymbol{n}_{\mathrm{T}}) \tag{5.5}$$

and, inserted into eq. (5.4), be used to estimate lower bound of τ_{crit}. For pure magnesium, Glüge and Kalisch (2008) derived a value consistent with the critical shear stress of 2.7 MPa given by Koike (2005).

The applicability of a Schmid law still depends strongly on the material and the modelling scale. Two extreme examples are Zn and Mg. In Zn, the propagation stress of a twin is well below the nucleation stress (Bell and Cahn, 1957), which induces a jerky yield behaviour. Further, the twin-parent interfaces are almost uncurved, and are aligned only in some specific orientations, the preference of which is temperature-dependent (Straumal et al., 2001).

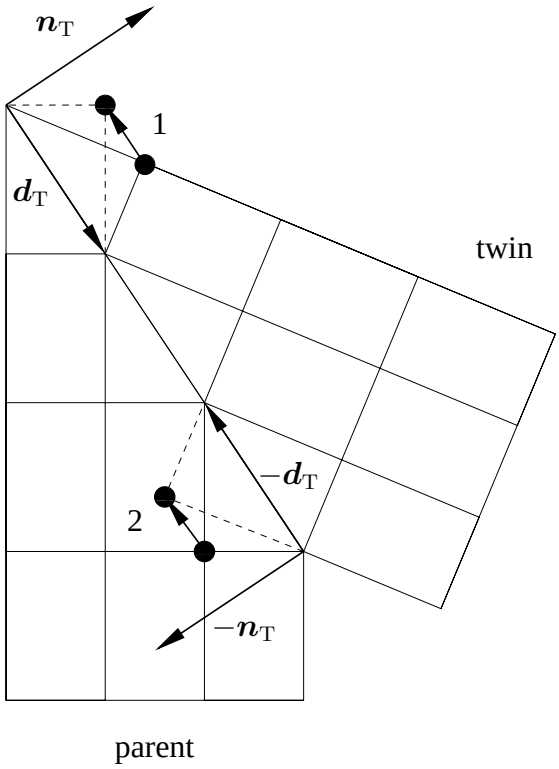

Figure 5.1: Atom movement for twinning (arrow 2, growth of the twin, the interface moves towards the parent) and detwinning (arrow 1, growth of the parent, the interface moves towards the twin). It is pointed out that the viewpoint which side of the interface is a parent and which is a twin is arbitrary. In this work, the definition is such that $\boldsymbol{n}$ directs into the twin and that $\boldsymbol{d}$ directs into the shear direction connected to twin growth.

From a microscopic point of view, the application of a Schmid law as a twinning criterion seems to be reasonable due to the fact that the twin formation can be explained by the movement of the partial dislocations, since a Schmid law works well for the dislocation movement underlying crystallographic slip. In fact, it is applied successfully to magnesium (Barnett, 2003), but seemed to be useless due to the large scattering of experimentally measured critical shear stresses (Thompson and Hingley, 1955; Wonsiewicz and Backofen, 1967; Christian and Mahajan, 1995). One problem is that such measurements are difficult to perform. Twins nucleate at inhomogeneities in the crystal, like intersectioning points of slip lines, at grain boundaries, or at crack tips. If one is interested in determining a critical nucleation stress, it would be necessary to determine the local stress where and when the twin emerges. Due to the unavoidable inhomogeneities, a reliable estimation of such a critical stress state is rather difficult. As mentioned before, molecular dynamic simulations are capable to give a deeper insight into the mechanism underlying twin propagation (see, e.g., the series of articles by Serra and Bacon).

However, since a Schmid law seems to work well for magnesium, it is applied in the remainder. The approach by Ball and James, that is used here in a regularised version, states that the phase that has the least strain energy is the preferred one. In the 1D-example above, one would come up with the stress-strain curve given in Fig. 4.5. The critical point of the phase change lies exactly in the middle of the stress-free configurations, with the corresponding critical stress. Applied to twinning, these would correspond approximately to

$$\tau_{\text{twin}} = G\frac{\gamma_0}{2}, \tag{5.6}$$

with G being the shear modulus in the twin system. This yields as an example $\tau^{\text{c}}_{\text{Mg}} \approx 2000$ MPa for $\langle\bar{1}011\rangle\{\bar{1}012\}$ twinning in magnesium, which is clearly too large. The observed critical stress $\tau^{\text{c}}_{\text{Mgreal}} \approx 2.7$ MPa (Koike, 2005) is three orders of magnitude lower than the one that emerges from the Ball and James-approach. This comes from the partial dislocation movement, which is ignored by the purely elastic modelling. Therefore, one has to think of how the model so far developed can be adapted to realistic stress states for twinning. One could introduce a plastic variable, which would not have a physical interpretation on the microscale, and which would require an evolution equation. The only way to stick to an elastic modelling is to modify the elastic law such that the apparent stress strain relation is approximated. Such nonlinear elastic laws can be used to model plastic material behaviour (Hencky, 1924; Ramberg and Osgood, 1943), as long as no local unloading occurs. In the following two sections, two possible modifications of the elastic law are discussed.

5.2 Adaptation of the Stresses

A simple solution is to project the stress state $\boldsymbol{T}$ into an admissible stress state $\boldsymbol{T}^*$ if the critical stress state has been passed,

$$\boldsymbol{T}_{\text{crit}} = \boldsymbol{T} - \lambda\frac{\partial\phi}{\partial\boldsymbol{T}}, \quad \phi(\boldsymbol{T}_{\text{crit}}) = 0. \tag{5.7}$$

The ϕ indicates whether the critical stress state is passed. It can be considered as a 5D-hypersurface in the 6D stress space, representing all critical stress states. Therefore, it is sometimes referred to as ”yield surface”. For example, if a Schmid law is applied

$$\phi = \tau - \tau_{\text{twin}}, \quad \tau = (\boldsymbol{C}\boldsymbol{T}) \cdot\cdot\, \boldsymbol{M} = \boldsymbol{T} \cdot\cdot\, \text{sym}(\boldsymbol{C}\boldsymbol{M}), \quad \boldsymbol{M} = \boldsymbol{d}_0 \otimes \boldsymbol{n}_0, \tag{5.8}$$

with the Mandel stress tensor $\boldsymbol{CT}$ and the Schmid tensor $\boldsymbol{M}$. In the latter equation, one has ensure that $\boldsymbol{d}$ and $\boldsymbol{n}$ are pulled back to the reference placement (see, e.g., Bertram (2005) p. 298), where $\boldsymbol{n}_0$ and $\boldsymbol{d}_0$ are normalised and perpendicular. Then, if $\phi > 0$, the critical stress state is passed, and one has to project the stresses $\boldsymbol{T}$ according to eq. (5.7) into an admissible stress state $\boldsymbol{T}_{\text{crit}}$. If $\partial\phi/\partial\boldsymbol{T}$ is normalised, λ can serve as a distance measure between $\boldsymbol{T}$ and $\boldsymbol{T}_{\text{crit}}$. The latter method can be applied to the twin variants if no double twinning is regarded, i.e., if the twin variants can only jump back to the one parent configuration from which they stem, which means that only one twin system has to be incorporated. One obtains from eqs. (5.7) and (5.8)

$$\lambda = \frac{\tau - \tau_{\text{twin}}}{\|\text{sym}(\boldsymbol{CM})\|^2}, \tag{5.9}$$

$$\boldsymbol{T}_{\text{crit}} = \boldsymbol{T} - \lambda \text{sym}(\boldsymbol{CM}). \tag{5.10}$$

When $\boldsymbol{C} \approx \boldsymbol{I}$, the latter can be simplified to

$$\boldsymbol{T}_{\text{crit}} = \boldsymbol{T} - 2(\boldsymbol{T} \cdot\cdot\ \text{sym}(\boldsymbol{M}) - \tau_{\text{twin}})\text{sym}(\boldsymbol{M}). \tag{5.11}$$

The situation is different when regarding the parent, which can convert into more than one twin variant. Applying the Schmid law, one has to check $\tau_i \leq \tau_{\text{twin}}$ in all potential twin systems. Due to the $\mathcal{C}^0$-continuity of the corresponding yield surface, the projection method (eq. 5.7) cannot be applied without further efforts. The same problem arises in crystal plasticity when a Schmid law is combined with an associated flow rule. Therefore, different regularisation schemes have been proposed (e.g., Bertram (2005)). A common regularised yield surface is

$$\phi = \sum_{i=1}^{n} \left(\frac{|\tau_i|}{\tau_{\text{twin}\ i}} \right)^m - 1, \quad m \geq 1, \tag{5.12}$$

which tends to the Schmid law when $m \to \infty$. $\boldsymbol{T}_{\text{crit}}$ and λ cannot be calculated explicitely for $m \neq 1$. Due to the polarity of twinning, the absolute value $|\tau_i|$ has to be replaced by $\langle\tau_i\rangle = (\tau_i + |\tau_i|)/2$. A simpler way to obtain a stress state $\boldsymbol{T}_{\text{crit}}$ with Schmid stresses lower than τ_{twin} in any twin system is to use the radial return method (Simo and Hughes, 1998), i.e. scale down the entire stress tensor, taking as proportion that the largest τ_i has to be equal to τ_{twin}. Since the trace of $\boldsymbol{M}_i$ is 0, it is sufficient to recalculate the Mandel stress deviator. This is automatically fulfilled by the projection methods described above, but has to be respected explicitely in the radial return method. In the following, $\boldsymbol{M}$ is the Schmid tensor corresponding to the twin system in which the maximal shear stress is found. The recalculated Mandel stresses are given by

$$(\boldsymbol{CT})^* = (\boldsymbol{CT})^\circ + \alpha(\boldsymbol{CT})', \tag{5.13}$$

and should yield

$$\tau_{\text{twin}} = (\boldsymbol{CT})^* \cdot\cdot\, \boldsymbol{M}, \tag{5.14}$$

which is used to determine α:

$$\tau_{\text{twin}} = ((\boldsymbol{CT})^\circ + \alpha(\boldsymbol{CT})') \cdot\cdot\, \boldsymbol{M} = \alpha\tau_{\max}, \tag{5.15}$$

i.e. $\alpha = \tau_{\text{twin}}/\tau_{\max}$. One can confirm that the recalculated Mandel stresses yield symmetric second Piola Kirchhoff stresses,

$$\boldsymbol{T}_{\text{crit}} = \boldsymbol{C}^{-1}(\boldsymbol{CT})^{*} = \boldsymbol{C}^{-1}\left((\boldsymbol{CT})^{\circ} + \frac{\tau_{\text{crit}}}{\tau_{\max}}(\boldsymbol{CT})'\right) \tag{5.16}$$

$$\boldsymbol{T}_{\text{crit}} = \boldsymbol{C}^{-1}\left(\frac{\tau_{\text{twin}}}{\tau_{\max}}(\boldsymbol{CT}) + \frac{1}{3}\text{tr}(\boldsymbol{CT})\left(1 - \frac{\tau_{\text{twin}}}{\tau_{\max}}\right)\boldsymbol{I}\right) \tag{5.17}$$

$$\boldsymbol{T}_{\text{crit}} = \frac{\tau_{\text{twin}}}{\tau_{\max}}\boldsymbol{T} + \frac{1}{3}\text{tr}(\boldsymbol{CT})\left(1 - \frac{\tau_{\text{twin}}}{\tau_{\max}}\right)\boldsymbol{C}^{-1}. \tag{5.18}$$

Again, one can simplify by means of the approximation $\boldsymbol{C} \approx \boldsymbol{I}$,

$$\boldsymbol{T}_{\text{crit}} = \boldsymbol{T}^{\circ} + \frac{\tau_{\text{twin}}}{\tau_{\max}}\boldsymbol{T}'. \tag{5.19}$$

The given methods have a big disadvantage: By altering $\boldsymbol{T}$, in general, the integrability condition for hyperelasticity is not met, and the second law of thermodynamics is violated. Therefore, one has to think of alternative approaches.

5.3 Adaptation of the Strain Energy

Beyond the critical state, the existence of an elastic strain energy is questionable. As discussed before, an entirely physically motivated modelling must incorporate the movement and arrangement of the partial dislocations, involving a kinetic relation. Here, it is as well focused on practicability and numerical efficiency, which is aimed for by a purely elastic modelling. Therefore, the w_i have to be adapted beyond the critical state such that the elastic law yields results which are in agreement with experimental findings.

For the explanation of the concept, indexing of the different phases and configuration change is omitted in the remainder. As the individual strain energies are defined in terms of strains, an indicator function $\phi(\boldsymbol{E})$ is defined, which is used to identify critical strain states, beyond which the strain energy is modified. If $\phi(\boldsymbol{E}) < 0$, $\boldsymbol{E}$ is a subcritical strain state. If $\phi(\boldsymbol{E}) > 0$, $\boldsymbol{E}$ is an overcritical strain state. The critical strain states correspond to $\phi(\boldsymbol{E}) = 0$. A critical strain state connected to an overcritical strain $\boldsymbol{E}$ can be specified by an orthogonal projection

$$\boldsymbol{E}_{\text{crit}} = \boldsymbol{E} - \lambda\phi'(\boldsymbol{E}_{\text{crit}}), \qquad \phi(\boldsymbol{E}_{\text{crit}}) = 0, \tag{5.20}$$

sketched in Fig. 5.2. Alternatively, one could think of a critical strain state assignment $\boldsymbol{E}_{\text{crit}}(\boldsymbol{E})$ by demanding $\min\|\boldsymbol{E} - \boldsymbol{E}_{\text{crit}}\|,\ \phi(\boldsymbol{E}_{\text{crit}}) = 0$. The latter formulation is alike the projection method, but it does not require the C^1 continuity of $\phi(\boldsymbol{E})$. An even simpler way is to use the radial return method $\boldsymbol{E}_{\text{crit}} = \alpha\boldsymbol{E},\ \phi(\boldsymbol{E}_{\text{crit}}) = 0$, which does not even demand the convexity of $\phi(\boldsymbol{E})$. In anticipation of the numerical results, no significant difference between the orthogonal projection and the radial return method could be determined.

Focusing on the definition of ϕ, if a critical twinning shear strain γ_{twin} is defined in one potential twin system, one can take

$$\phi_1(\boldsymbol{E}) = \gamma - \gamma_{\text{twin}}, \qquad \gamma = 2\boldsymbol{E} \cdot\cdot\, \boldsymbol{M}, \qquad \boldsymbol{M} = \boldsymbol{d} \otimes \boldsymbol{n}. \tag{5.21}$$

For this simple case, eq. (5.20) can be solved explicitly for $\boldsymbol{E}_{\mathrm{crit}}$, namely

$$\boldsymbol{E}_{\mathrm{crit}} = \boldsymbol{E} - \lambda \mathrm{sym}(\boldsymbol{M}), \qquad \lambda = \gamma - \gamma_{\mathrm{twin}}. \tag{5.22}$$

Although this approach is quite similar to the proposal from the latter Section, the thermodynamic consistency can be assured more easily by formulating the critical state in terms of strains. By simply stating w in terms of strains and corresponding unique critical strain states its existence is assured. Moreover, as magnesium is elastically approximately isotropic, the critical stress state can be easily linked to the a critical strain state, namely by a simple shear deformation in the twin system.

The latter projection is useful if only one twin system is potentially active. If more than one twin system can be activated, the "critical strain state hypersurface" has to be constructed such that a unique assignment $\boldsymbol{E} \rightarrow \boldsymbol{E}_{\mathrm{crit}}$ is possible. I.e., it must be $\mathcal{C}^1$ continuous and convex in the sense that $\phi(\alpha \boldsymbol{E}_{\mathrm{crit1}} + (1-\alpha)\boldsymbol{E}_{\mathrm{crit2}}) < 0,\ \alpha \in [0,1]$ holds for any two critical strain states. Moreover, a "shooting through" the domain of admissible strain states is always possible, which yields two solutions for $\boldsymbol{E}_{\mathrm{crit}}$. The feasible one is the one which is closer to the strain state $\boldsymbol{E}$, i.e., the one with the smaller absolute value of λ.

A possible ϕ_n for n different twin systems is

$$\phi_n(\boldsymbol{E}) = \sum_{i=1}^{n} \langle \gamma_i / \gamma_{\mathrm{twin}} \rangle^m - 1, \qquad \gamma_i = 2\boldsymbol{E} \cdot\cdot \boldsymbol{M}_i, \tag{5.23}$$

with $\langle x \rangle = (x + |x|)/2$ to respect the polarity of twinning. Here, if one out of the n distinct $\gamma_i > \gamma_{\mathrm{twin}}$, then $\phi_n(\boldsymbol{E}) > 0$. m is a preferably large integer regularisation parameter. By taking a large value for m, γ_{twin} can practically be reached in all twin systems simultaneously without passing a critical strain state. For $m > 1$, $\boldsymbol{E}_{\mathrm{crit}}$ cannot be given explicitly.

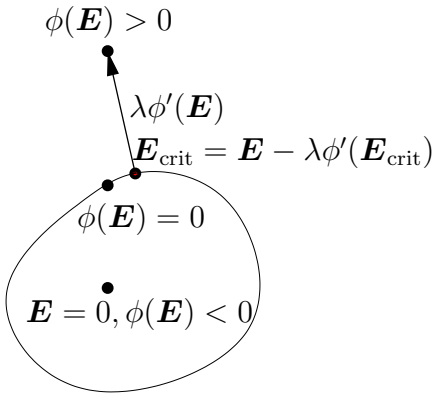

Figure 5.2: Scheme on the orthogonal projection to a critical strain state.

With the critical strain definition at hand, one is able to modify the strain energy. It is pointed out again that beyond the critical strain state, the strain energy density is used as a pure modelling tool, but its existence ensures the thermodynamic consistency in the large. The following modified strain energy is applied:

$$w = w_0 = \frac{1}{2}\boldsymbol{E} \cdot\cdot \mathbb{C} \cdot\cdot \boldsymbol{E} \qquad \text{if} \quad \phi(\boldsymbol{E}) \leq 0 \tag{5.24}$$

$$w = w_0 - \frac{1}{2}(\boldsymbol{E} - \boldsymbol{E}_{\mathrm{crit}}) \cdot\cdot \mathbb{C}_0 \cdot\cdot (\boldsymbol{E} - \boldsymbol{E}_{\mathrm{crit}}) \qquad \text{if} \quad \phi(\boldsymbol{E}) > 0. \tag{5.25}$$

With the major symmetry of $\mathbb{C}_0$, in the case of $\phi(\boldsymbol{E}) > 0$, w can be simplified to

$$w = w_0 - \frac{1}{2}(\boldsymbol{E} - \boldsymbol{E}_{\mathrm{crit}}) \cdot\cdot\, \mathbb{C}_0 \cdot\cdot\, (\boldsymbol{E} - \boldsymbol{E}_{\mathrm{crit}}) \tag{5.26}$$

$$= \frac{1}{2}\boldsymbol{E} \cdot\cdot\, \mathbb{C}_0 \cdot\cdot\, \boldsymbol{E} - \frac{1}{2}(\boldsymbol{E} - \boldsymbol{E}_{\mathrm{crit}}) \cdot\cdot\, \mathbb{C}_0 \cdot\cdot\, (\boldsymbol{E} - \boldsymbol{E}_{\mathrm{crit}}) \tag{5.27}$$

$$= \boldsymbol{E} \cdot\cdot\, \mathbb{C}_0 \cdot\cdot\, \boldsymbol{E}_{\mathrm{crit}} - \frac{1}{2}\boldsymbol{E}_{\mathrm{crit}} \cdot\cdot\, \mathbb{C}_0 \cdot\cdot\, \boldsymbol{E}_{\mathrm{crit}}. \tag{5.28}$$

The latter modification of w is chosen because it is $\mathcal{C}^1$ continuous. Moreover, it ensures that the stress level does not increase after passing the critical strain state. If we ignore the dependence of $\boldsymbol{E}_{\mathrm{crit}}$ on $\boldsymbol{E}$, we yield a strain energy which is linear in $\boldsymbol{E}$. In a monotonic strain driven test (in direction of $\partial\phi/\partial\boldsymbol{E}|_{\boldsymbol{E}_{\mathrm{crit}}}$, i.e. $\boldsymbol{E}_{\mathrm{crit}}$ is constant), one obtains a constant stress strain relation beyond the critical strain state, corresponding to the linear increase of w represented by the first term in eq. (5.28).

To calculate the stresses $\boldsymbol{T} = \partial w/\partial\boldsymbol{E}$, the derivative $\partial\boldsymbol{E}_{\mathrm{crit}}/\partial\boldsymbol{E}$ is needed. $\boldsymbol{E}_{\mathrm{crit}}$ is given implicitly by eq. (5.20), which can be rearranged as

$$\boldsymbol{0} = \boldsymbol{g} = \boldsymbol{E} - \lambda\phi'(\boldsymbol{E}_{\mathrm{crit}}) - \boldsymbol{E}_{\mathrm{crit}} \tag{5.29}$$

$$0 = g = \phi(\boldsymbol{E}_{\mathrm{crit}}). \tag{5.30}$$

The dependence of ϕ and its derivatives on $\boldsymbol{E}_{\mathrm{crit}}$ is omitted in the remainder. The complete differential of the latter equations with respect to $\boldsymbol{E}$ is also zero, so that

$$\boldsymbol{0} = \frac{\mathrm{d}\boldsymbol{g}}{\mathrm{d}\boldsymbol{E}} = \mathbb{I}^S - \lambda\phi'' \cdot\cdot\, \frac{\partial\boldsymbol{E}_{\mathrm{crit}}}{\partial\boldsymbol{E}} - \phi' \otimes \frac{\partial\lambda}{\partial\boldsymbol{E}} - \frac{\partial\boldsymbol{E}_{\mathrm{crit}}}{\partial\boldsymbol{E}} \tag{5.31}$$

$$= \mathbb{I}^S - \phi' \otimes \frac{\partial\lambda}{\partial\boldsymbol{E}} - (\lambda\phi'' + \mathbb{I}^S) \cdot\cdot\, \frac{\partial\boldsymbol{E}_{\mathrm{crit}}}{\partial\boldsymbol{E}} \tag{5.32}$$

$$\boldsymbol{0} = \frac{\mathrm{d}g}{\mathrm{d}\boldsymbol{E}} = \phi' \cdot\cdot\, \frac{\partial\boldsymbol{E}_{\mathrm{crit}}}{\partial\boldsymbol{E}}, \tag{5.33}$$

with $\mathbb{I}^S$ being the fourth-order identity on symmetric second-order tensors. The system of 36+6 linear equations has 36+6 unknowns $\partial\boldsymbol{E}_{\mathrm{crit}}/\partial\boldsymbol{E}$ and $\partial\lambda/\partial\boldsymbol{E}$, while all other derivatives can be directly calculated. Rearranging eq. (5.32) to

$$\frac{\partial\boldsymbol{E}_{\mathrm{crit}}}{\partial\boldsymbol{E}} = \mathbb{A} \cdot\cdot\, \left(\mathbb{I}^S - \phi' \otimes \frac{\partial\lambda}{\partial\boldsymbol{E}}\right), \qquad \mathbb{A} = (\mathbb{I}^S + \lambda\phi'')^{-1} \tag{5.34}$$

and inserting into eq. (5.33) yields

$$\frac{\partial\lambda}{\partial\boldsymbol{E}} = \alpha^{-1}\phi' \cdot\cdot\, \mathbb{A}, \qquad \alpha = \phi' \cdot\cdot\, \mathbb{A} \cdot\cdot\, \phi' \tag{5.35}$$

which can be substituted in eq. (5.34) to obtain

$$\frac{\partial\boldsymbol{E}_{\mathrm{crit}}}{\partial\boldsymbol{E}} = \mathbb{A} - \alpha^{-1}(\mathbb{A} \cdot\cdot\, \phi') \otimes (\mathbb{A} \cdot\cdot\, \phi'), \tag{5.36}$$

where possible simplifications by using the symmetries of $\boldsymbol{E}$ and $\mathbb{A}$ have been employed. One notes that $\partial\boldsymbol{E}_{\mathrm{crit}}/\partial\boldsymbol{E}$ has the projector property $\partial\boldsymbol{E}_{\mathrm{crit}}/\partial\boldsymbol{E} \cdot\cdot\, \phi' = \boldsymbol{0}$. This has been expected due to the fact that different $\boldsymbol{E}$ can be projected to the same $\boldsymbol{E}_{\mathrm{crit}}$.

Chapter 6

Final Constitutive Equations and Implementation

In this section, the model derived in the last Sections is summarised. The index 0 indicates the parent configuration, while the indices $1 \dots n$ run over the possible twin variants. In order to avoid confusion, in this Section all sums are written out, i.e. multiple indices in a product do not imply summation automatically. The strain energy density is given by

$$\tilde{w} = \sum_{i=0}^{n} a_i w_i \qquad a_i = \frac{g_i}{\sum_{j=0}^{n} g_j} \qquad g_i = \frac{h(w_i)}{1 - h(w_i)} \qquad h(w_i) = \exp(-k w_i), \tag{6.1}$$

with k being a preferably large regularisation parameter, see Section 4.4. The w_i are given by

$$w_i = \frac{1}{2} \boldsymbol{E}_i \cdot\cdot \mathbb{C}_0 \cdot\cdot \boldsymbol{E}_i \qquad \text{if } \phi_i(\boldsymbol{E}_i) \leq 0 \tag{6.2}$$

$$w_i = \boldsymbol{E}_i \cdot\cdot \mathbb{C}_0 \cdot\cdot \boldsymbol{E}_{\text{crit}i} - \frac{1}{2} \boldsymbol{E}_{\text{crit}i} \cdot\cdot \mathbb{C}_0 \cdot\cdot \boldsymbol{E}_{\text{crit}i} \qquad \text{if } \phi_i(\boldsymbol{E}_i) > 0, \tag{6.3}$$

according to the phenomenological model adaptation of the strain energies of Section 5.3. $\mathbb{C}_0$ is the elasticity tetrad. $\boldsymbol{E}_{\text{crit}i}$ are given implicitly through the orthonormal projection

$$\boldsymbol{E}_{\text{crit}i} = \boldsymbol{E}_i - \lambda \phi_i'(\boldsymbol{E}_{\text{crit}i}) \qquad \phi_i(\boldsymbol{E}_{\text{crit}i}) = 0, \tag{6.4}$$

where λ needs to be calculated such that the latter equation holds. The ϕ_i are given by

$$\phi_0(\boldsymbol{E}_0) = \sum_{j=1}^{n} \langle \gamma_j / \gamma_{\text{twin}} \rangle^m - 1 \qquad \gamma_j = \boldsymbol{E}_0 \cdot\cdot \boldsymbol{M}_j \tag{6.5}$$

$$\phi_i(\boldsymbol{E}_i) = \langle \gamma_i - \gamma_{\text{twin}} \rangle \qquad \gamma_i = \boldsymbol{E}_i \cdot\cdot \boldsymbol{M}_i \qquad i = 1 \dots n, \tag{6.6}$$

with the preferably large regularisation parameter m and a critical shear strain γ_{twin}. The Green's strains $\boldsymbol{E}_i$ are obtained by

$$\boldsymbol{E}_i = \frac{1}{2} (\boldsymbol{P}_i^T \boldsymbol{C} \boldsymbol{P}_i - \boldsymbol{I}). \tag{6.7}$$

The plastic transformations map the elastic reference law to the reference placement. $\boldsymbol{P}_0$ is given by the parent crystal orientation, and $\boldsymbol{P}_i,\ i = 1..n$ are given by

$$\boldsymbol{P}_i = \boldsymbol{P}_0 \boldsymbol{P}_{i0} \qquad i = 1...n, \tag{6.8}$$

with the plastic transformations $\boldsymbol{P}_{i0}$

$$\boldsymbol{P}_{i0} = -\boldsymbol{I} - \gamma_0 \boldsymbol{d}_i \otimes \boldsymbol{n}_i + 2\boldsymbol{n}_i \otimes \boldsymbol{n}_i \qquad i = 1...n, \tag{6.9}$$

which map the elastic reference law to the twin configurations, see eq. (4.64) and Fig. 6.1. With $\tilde{w}$ at hand by the latter system of equations, the second Piola Kirchhoff stresses are

$$\boldsymbol{T} = \frac{\partial \tilde{w}}{\partial \boldsymbol{E}} \approx \sum_{i=0}^{n} a_i \boldsymbol{T}_i \tag{6.10}$$

$$\boldsymbol{T}_i = \frac{\partial w_i}{\partial \boldsymbol{E}} = \boldsymbol{P}_i \frac{\partial w_i}{\partial \boldsymbol{E}_i} \boldsymbol{P}_i^T, \tag{6.11}$$

see Section 4.6. This is, so far, the elastic law. Incorporating the viscous regularisation corresponds to adding the deviatoric part of $\frac{J\eta}{2}\dot{\boldsymbol{C}}$ to the second Piola Kirchhoff stresses. Regarding the card glide mechanism, the plastic transformation of the parent evolves corresponding to

$$-\boldsymbol{P}_0^{-1}\dot{\boldsymbol{P}}_0 = \dot{\gamma}\boldsymbol{d}^* \otimes \boldsymbol{n}, \qquad \boldsymbol{d}^* = \frac{\boldsymbol{d}}{\|\boldsymbol{d}\|}, \tag{6.12}$$

with

$$\boldsymbol{d} = (\boldsymbol{I} - \boldsymbol{n} \otimes \boldsymbol{n})\tilde{\boldsymbol{F}}^{-1}\boldsymbol{\sigma}\tilde{\boldsymbol{F}}^{-T}\boldsymbol{n}, \qquad \tilde{\boldsymbol{F}} = \boldsymbol{F}\boldsymbol{P}_0. \tag{6.13}$$

$\dot{\gamma}$ is determined consistently with the elastic law. I.e., during the plastic flow, the resolved shear stress in the card glide system is equal to the flow stress.

6.1 Implementation into the FE System ABAQUS

The variables $\mathbb{C}_0$, $\boldsymbol{d}_{i0}$ and $\boldsymbol{n}_{i0}$ have been defined with respect to an orthonormal basis as depicted in Fig. 6.1. With $\boldsymbol{d}_{i0}$ and $\boldsymbol{n}_{i0}$, the plastic transformations $\boldsymbol{P}_{i0}$ have been defined following eq. (6.9), which map the elastic law of the reference twin configurations to the elastic law of the parent, i.e. to the elastic reference law. The final plastic transformations which map the elastic reference laws of the parent and all potential twin variants to the reference placement are given by eq. (6.8) for $i = 1...n$ and $\boldsymbol{P}_i = \boldsymbol{P}_0$ for $i = 0$, where $\boldsymbol{P}_0$ maps the lattice basis of the (parent) elastic reference law to the lattice basis in the reference placement.

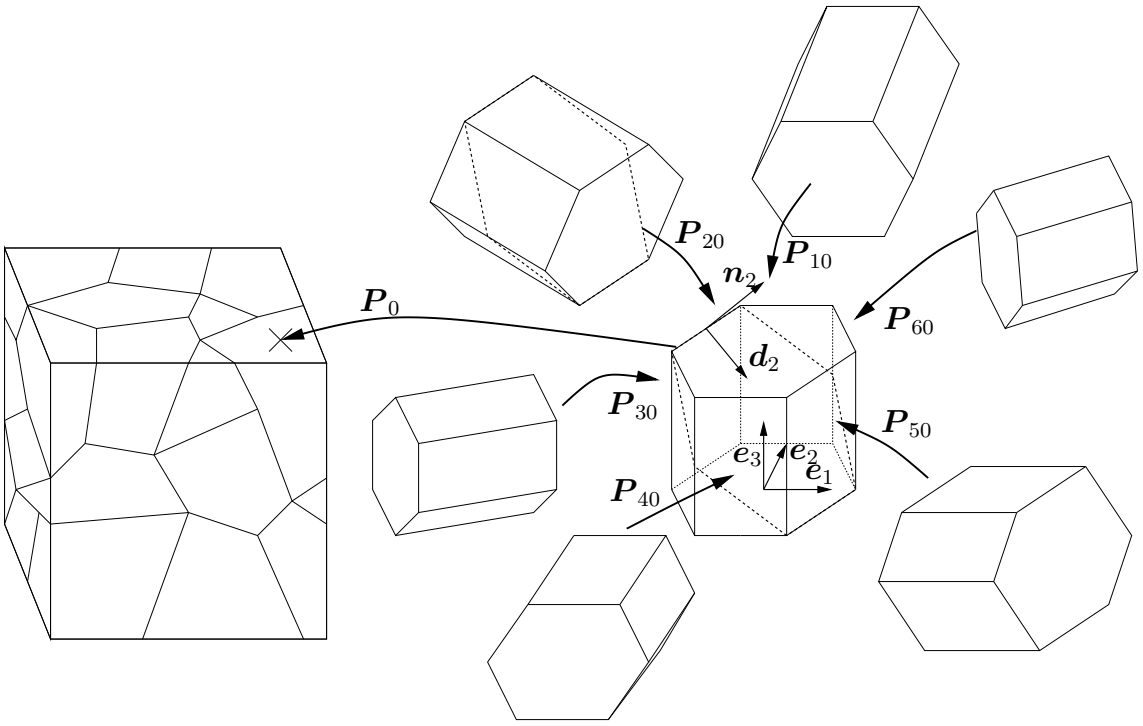

Figure 6.1: Connection of elastic reference law and reference placement.

6.2 Implementation of the Card Glide Mechanism

As most FE systems evaluate the node displacement as a primary result, the displacements (and hence the strains) are not internal variables, and taken care of by the FE program. This means that although $\dot{\boldsymbol{C}}$ appears in the equations, time integration of $\boldsymbol{C}$ needs not to concern the user of the UMAT interface. However, the card glide mechanism is the one ingredient of the model that forces to deal with the integration of an internal variable, namely $\boldsymbol{P}_0$, the plastic transformation of the parent configuration. The index 0 is omitted in the remainder of this Section since no other $\boldsymbol{P}$ appears. See Bertram (2005) for an account to plasticity, and Simo and Hughes (1998) for an account to its numerical treatment.

The Mandel stresses with respect to the elastic reference law are given by

$$\overset{\mathrm{M}}{\boldsymbol{T}} = \frac{1}{2}\boldsymbol{P}^T\boldsymbol{C}\boldsymbol{P}\left(\mathbb{C}_0 \cdot\cdot \left(\boldsymbol{P}^T\boldsymbol{C}\boldsymbol{P} - \boldsymbol{I}\right)\right). \tag{6.14}$$

Then, the direction of and the maximal shear stress in the basal plane are given by

$$\boldsymbol{d} = (\overset{\mathrm{M}}{\boldsymbol{T}} \cdot \boldsymbol{n}) \cdot (\boldsymbol{I} - \boldsymbol{n} \otimes \boldsymbol{n}) \tag{6.15}$$

$$\tau_{\mathrm{el}} = \sqrt{\boldsymbol{d} \cdot \boldsymbol{d}}, \tag{6.16}$$

with $\boldsymbol{n}$ being the normalised $\boldsymbol{c}$-axis direction vector. The yield and loading conditions are

$$\phi(\tau_{\mathrm{el}}, \tau_{\mathrm{basal}}) = \tau_{\mathrm{el}} - \tau_{\mathrm{basal}} = 0, \qquad \dot{\phi} > 0. \tag{6.17}$$

If both are fulfilled, $\boldsymbol{P}$ evolves, otherwise the deformation is elastic, and $\dot{\boldsymbol{P}} = \boldsymbol{0}$. While $\boldsymbol{P}$ evolves, the consistency condition $\dot{\phi} = 0$ must hold. When elastoplasticity is treated numerically, one does not

obtain a continuous evolution of $\boldsymbol{P}$, but a sequence of discrete $\boldsymbol{P}_n$. Therefore, the loading condition does not enter the numerical considerations, while the consistency condition is ensured pointwise at each of the discrete time steps.

ABAQUS passes $\boldsymbol{P}_n$, $\boldsymbol{F}_n$ and $\boldsymbol{F}_{n+1}$ to the user subroutine, and the plastic transformation $\boldsymbol{P}_{n+1}$ needs to be determined. First, a predictor step is carried out, where $\boldsymbol{P}_{n+1} = \boldsymbol{P}_n$ is assumed. By this, one treats the strain increment as fully elastic, and calculates the Mandel stresses and resolved shear stress as given above. Then, if

$$\tau_{\mathrm{el},n+1} > \tau_{\mathrm{basal},n} \tag{6.18}$$

is fullfilled, $\boldsymbol{P}_{n+1}$ has to be determined such that $\tau_{\mathrm{el},n+1} = \tau_{\mathrm{basal},n+1}$. By assuming a constant slip direction, one can make use of eq. 4.107, and write

$$\boldsymbol{P}_{n+1} = \boldsymbol{P}_n(\boldsymbol{I} - \Delta\gamma \boldsymbol{d}^* \otimes \boldsymbol{n}), \tag{6.19}$$

where $\boldsymbol{d}^*$ is the normalised $\boldsymbol{d}$ from the predictor step. In order to respect isotropic hardening, let us assume that τ_{basal} depends on the accumulated shear

$$\gamma_{\mathrm{acc},n+1} = \gamma_{\mathrm{acc},n} + |\Delta\gamma|, \tag{6.20}$$

which is an internal variable just like $\boldsymbol{P}$. One can determine the scalar variable $\Delta\gamma$ such that the scalar equation $\tau_{\mathrm{el},n+1} = \tau_{\mathrm{basal},n+1}$ holds by Newtons method, or, slower but more stable, by the bisection method. The fact that only one scalar equation has to be solved renders the card glide mechanism in this case fairly fast and stable.

As mentioned before, basal glide is taken into account only in the parent configuration, and it remains to discuss how this can be implemented. For this purpose, the indicator function ϕ from Section 5.3 has been used. ϕ is equal to -1 in the stress-free parent configuration, and grows with the regularisation exponent n, as the strain state diverges from this state. It is 0 when the critical strain state is reached. By defining $\tau_{\mathrm{basal}} = (\phi+2)\tau_{\mathrm{basal0}}$, one obtains a virtually unreachable Schmid stress when the critical strain is passed, while leaving τ_{basal} approximately unaltered in subcritical strain region. Although this treatment appears empiric at first glance, it can be interpreted as a regularisation of the algebraic condition that slip is only possible in the parent configuration, i.e. as long as $\phi_0(\boldsymbol{E}_0) < 0$. When the regularisation parameter $m \to \infty$ in ϕ_0 (eq. 5.23), $\tau_{\mathrm{basal}} = \tau_{\mathrm{basal0}}$ due to $\phi_0 \to -1$ for subcritical strain states, and $\tau_{\mathrm{basal}} \to \infty$ if a critical strain state is passed. Algebraic formulations are, however, not preferable from a numerical point of view, which is why the regularised formulation is used in this work.

In order to not mix too many ingredients in one model, hardening has been generally neglected, and $\tau_{\mathrm{basal0}} = \mathrm{const.}$ In the remainder, τ_{basal0} is a material parameter, and the index 0 is omitted.

Chapter 7

Testing of the Model

7.1 Material Parameters

The material parameters are given with respect to the elastic reference law. $\boldsymbol{e}_1$ is parallel to two edges of the base hexagon while $\boldsymbol{e}_3$ is parallel to the $\boldsymbol{c}$-axis. The elastic stiffness tetrad of magnesium (Simmons and Wang, 1971), with respect to the basis $\boldsymbol{E}_1 = \boldsymbol{e}_1 \otimes \boldsymbol{e}_1$, $\boldsymbol{E}_2 = \boldsymbol{e}_2 \otimes \boldsymbol{e}_2$, $\boldsymbol{E}_3 = \boldsymbol{e}_3 \otimes \boldsymbol{e}_3$, $\boldsymbol{E}_4 = \sqrt{2}/2(\boldsymbol{e}_1 \otimes \boldsymbol{e}_2 + \boldsymbol{e}_2 \otimes \boldsymbol{e}_1)$, $\boldsymbol{E}_5 = \sqrt{2}/2(\boldsymbol{e}_1 \otimes \boldsymbol{e}_3 + \boldsymbol{e}_3 \otimes \boldsymbol{e}_1)$, $\boldsymbol{E}_6 = \sqrt{2}/2(\boldsymbol{e}_2 \otimes \boldsymbol{e}_3 + \boldsymbol{e}_3 \otimes \boldsymbol{e}_2)$, is

$$\mathbb{C} = \begin{bmatrix} 56.49 & 23.16 & 18.10 & 0 & 0 & 0 \\ & 56.49 & 18.10 & 0 & 0 & 0 \\ & & 58.73 & 0 & 0 & 0 \\ & & & 2 \cdot 16.81 & 0 & 0 \\ & & & & 2 \cdot 16.81 & 0 \\ & & & & & 55.69 - 23.16 \end{bmatrix} \boldsymbol{E}_i \otimes \boldsymbol{E}_j, \tag{7.1}$$

in GPa. $\boldsymbol{E}_i$ is an orthonormal vector basis for symmetric second-order tensors, i.e. a fourth-order tensor with both subsymmetries can be denoted as a second-order tensor with respect to $\boldsymbol{E}_i$. The six structural tensors belonging to the $\{10\bar{1}2\}\langle\bar{1}011\rangle$ twin systems are given by

$$\boldsymbol{M}_1 = \boldsymbol{d}_1 \otimes \boldsymbol{n}_1 \tag{7.2}$$

$$\boldsymbol{d}_1 = \cos(\alpha)\boldsymbol{e}_2 + \sin(\alpha)\boldsymbol{e}_3 \tag{7.3}$$

$$\boldsymbol{n}_1 = -\sin(\alpha)\boldsymbol{e}_2 + \cos(\alpha)\boldsymbol{e}_3 \tag{7.4}$$

$$\boldsymbol{M}_i = \boldsymbol{Q}^{i-1}_{\pi/3\boldsymbol{e}_3} * \boldsymbol{M}_1, \qquad i = 2...6 \tag{7.5}$$

i.e. by rotating the twin system $\boldsymbol{M}_1$ in the sixfold symmetric hexagonal cell, with

$$\alpha = \operatorname{atan}(c/(a\sqrt{3})). \tag{7.6}$$

For magnesium and its alloys, $c/a \approx 1.623$. The twinning shear for the $\{10\bar{1}2\}\langle\bar{1}011\rangle$ twin systems is given by

$$\gamma_0 = \frac{\sqrt{3}}{c/a} - \frac{c/a}{\sqrt{3}}, \tag{7.7}$$

i.e. $\gamma_0 \approx 0.13$. The regularisation parameter k and the viscosity are taken as $k = 0.025$ and $\eta = 10$GPa s, unless stated otherwise. Reasonable values for η can be estimated by reviewing that $\eta\dot{\varepsilon}$ is small compared to the critical slip and twinning stresses, where $\dot{\varepsilon}$ is the average strain rate, e.g. $\|\boldsymbol{D}'\|$ or $\dot{\gamma}$ in a simple shear test. k is chosen such that the transition between the elastic laws of twin and parent is smooth, see the next Section.

The phenomenological model adaptation that has been used is the adaptation of the strain energy as discussed in Section 5.3, with the regularisation parameter $n = 10$. The used critical shear strain is $\gamma_{\text{twin}} = 0.05\gamma_0$ unless not stated otherwise. The critical shear stress is therefore approximately $\tau_{\text{crit}} = G\gamma_{\text{twin}} \approx 0.05 \times 0.1296 \times 16500\text{MPa} \approx 107\text{MPa}$.

7.2 Simple Shear Tests in a Twin System and the Basal Plane

Before any structural problem is solved with the FEM, it should be investigated how the material model behaves in an entirely strain-driven test, and how stresses and internal variables evolve if $\boldsymbol{F}(t)$ is prescribed. Most interesting is a shear test in one of the six twin systems. Therefore,

$$\boldsymbol{F} = \boldsymbol{I} + \gamma \boldsymbol{d}_1 \otimes \boldsymbol{n}_1, \qquad \boldsymbol{P}_0 = \boldsymbol{I} \tag{7.8}$$

is imposed, with $0 < \gamma < \gamma_0$. $\boldsymbol{P}_0 = \boldsymbol{I}$ indicates that the elastic law in the reference configuration is identical to the current elastic reference law. For this test, the softening that occurs when flipping into the twin system does not bother, since no equilibrium configuration is searched for. The additive viscosity is therefore not needed, and $\eta = 0$ is applied. Basal glide is also deactivated. In Fig. 7.1 the shear stress in the twin system $\tau_1 = \boldsymbol{\sigma} \cdot\cdot\, (\boldsymbol{d}_1 \otimes \boldsymbol{n}_1)$ is plotted over γ, and the regularisation parameter k, which smoothens the transitions between the different elastic laws, has been varied.

One recognises that the material is stress-free when the twin configuration is reached, and that the elastic behaviour is linear near the stress-free states. The parameter k influences the sharpness of the transition between the elastic laws, as it is expected from the regularisation. As the transition region, which is smoothed by the regularisation parameter k, corresponds to the nonconvex region (with a negative stiffness) no stable equilibrium configuration can be found in that interval. It merely serves as the transition zone. It is therefore reasonable to choose k large enough such that the elastic laws near the stress free configurations are represented sufficiently well, but small enough to have a smooth transition between the twin and parent configuration. Therefore, for the simulations that are presented in the following sections, $k = 0.025$ has been chosen.

It is further important to review the effect of the phenomenological model adaptation. Therefore, it has been incorporated with the critical shear strain $\gamma_{\text{twin}} = 0.05\gamma_0$. The critical shear stress fits well the prior estimation of approximately 110MPa, see Fig. 7.1. One notes that the phenomenological model adaptation limits the stresses.

In order to review the basal glide, a cyclic test with

$$\boldsymbol{F} = \boldsymbol{I} + \gamma \boldsymbol{a}_1 \otimes \boldsymbol{c}^*, \qquad \boldsymbol{P} = \boldsymbol{I} \tag{7.9}$$

has been carried out, with γ evolving linearly from 0 to 0.025 and back to 0. As the reference placement and the elastic reference law coincide again, $\boldsymbol{a}_1 = \boldsymbol{e}_1$ and $\boldsymbol{c}^* = \boldsymbol{e}_3$ are chosen. The

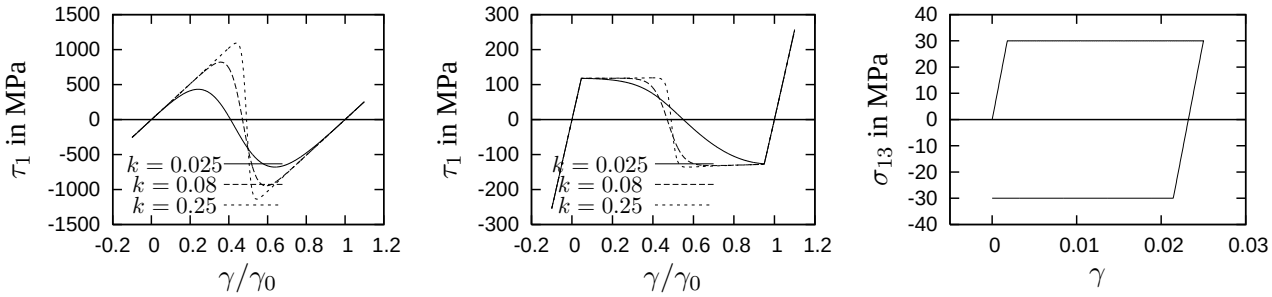

Figure 7.1: Resolved shear stress in twin system one over γ, without (left) and with (centre) the phenomenological model adaptation, resolved shear stress in a shear test within the basal plane (right), with $\tau_{\text{crit}} = 30$MPa.

resolved shear stress plotted in Fig. 7.1 corresponds therefore to the component σ_{13} when $\boldsymbol{\sigma}$ is given with respect to the basis $\boldsymbol{e}_i$. One clearly recognises the perfectly plastic behaviour as the card glide mechanism is activated, with $\tau_{\text{crit}} = 30$MPa.

7.3 FE Model 1: Simple Shear Deformation into one Twin System

7.3.1 Model Setup

In this Section, the fully deformation-controlled simple shear test from the last Section is extended to a structural problem. A strip of the dimensions 100mm×200mm×3mm is submitted to a simple shear deformation, see Fig. 7.2. The boundary conditions are such that a plane strain deformation is enforced, so that the problem is two-dimensional. Therefore along the thickness direction only one element has been assigned. The lattice is oriented such that the shear plane coincides with one of the six equivalent $\{10\bar{1}2\}$ twinning planes and that twinning can occur in the direction of the enforced shear direction. The displacement boundary conditions are such that one face is fixed, while the opposing face is displaced parallel and proportional to time by finally 15mm in 1000 seconds, and back to zero in 1000 seconds. A small notch at one of the free boundaries serves as a perturbation to trigger the twin formation. Different meshes have been been used, namely a regular hexahedral mesh with linear shape functions (element type C3D8) and irregular wedge meshes with linear and quadratic shape functions (element types C3D6 and C3D15).

The maximal displacement due to the twinning shear deformation is $\gamma_0 \times 100$mm. With $\gamma_0 \approx 0.13$, the faces should be displaced at least 13mm in order to enforce the entire twinning of the sample. The simulations are carried out with different meshes, varying the characteristic element size, the degree of the shape functions in the elements, and the viscosity in the material law.

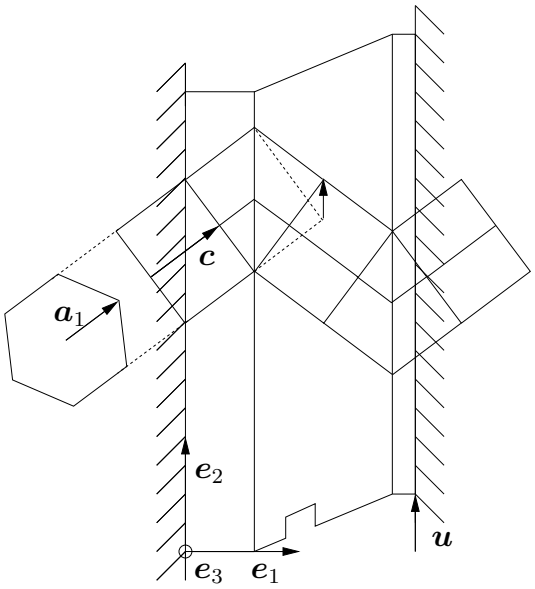

Figure 7.2: Simple shear deformation of a strip, with an oversized hexagonal cell. The lattice is oriented such that the shear plane coincides with one of the $\{10\bar{1}2\}$ twinning planes. A small notch is incorporated as preferred nucleation site.

7.3.2 Results

In the simulations a twin nucleates near the notch, and propagates along the shear direction. After invading the overall length of 200mm, the twin starts growing in direction of the shear plane normal, i.e., the thickness of the twin grows, see Fig. 7.4. As the deformation is reversed, a similar detwinning-behaviour is observed. It is pointed out that such ideal twinning and detwinning behaviour is not observed in reality. The simulation should merely demonstrate the possibility of detwinning, the effect of the phenomenological model adaptation, and the hysteresis loop.

The regularising viscosity is so small in the context of this simulation that a variation of it has no significant influence. Its effect on the nominal stress can be estimated by $\tau_{\text{visc}} \approx \dot{\gamma}\eta/2 = 1.5\text{E} - 4\text{s}^{-1}\eta/2 = 0.3$ MPa. One notes that the nominal critical twinning shear stress of approximately 110 MPa suites to the value that was adjusted in Section 7.1.

Consider the nominal shear stress-displacement diagram 7.3. One notes that at the displacement of approximately 13mm the entire specimen has been invaded by the twin, and that at ongoing deformation the elastic law of the twin is found. The distinct load drops in both diagrams are connected to the fineness of the mesh. Each load drop corresponds to the transition of the twin boundary from one element row to the next when the twin grows in thickness direction. Consequently, the coarser the mesh is, the larger is the load drop (Fig. 7.3). Moreover, the twin parent interfaces are approximately parallel to mesh interfaces, due to the mesh structure. This has an influence on the simulation results. In order to review the mesh-dependence in more detail, the simulations have been repeated with an irregular wedge mesh of moderate fineness, with linear and quadratic shape functions. The nominal shear stress over the displacement is depicted in Fig. 7.3, two particularly interesting states are depicted in Fig. 7.5. Fig. 7.3 shows the hysteresis connected to twinning and detwinning for an irregular wedge-mesh. At the onset of twinning and detwinning, the stress displacement curve fits quite well to the findings with the regular mesh. In the propagation stage, the first stress peak is not

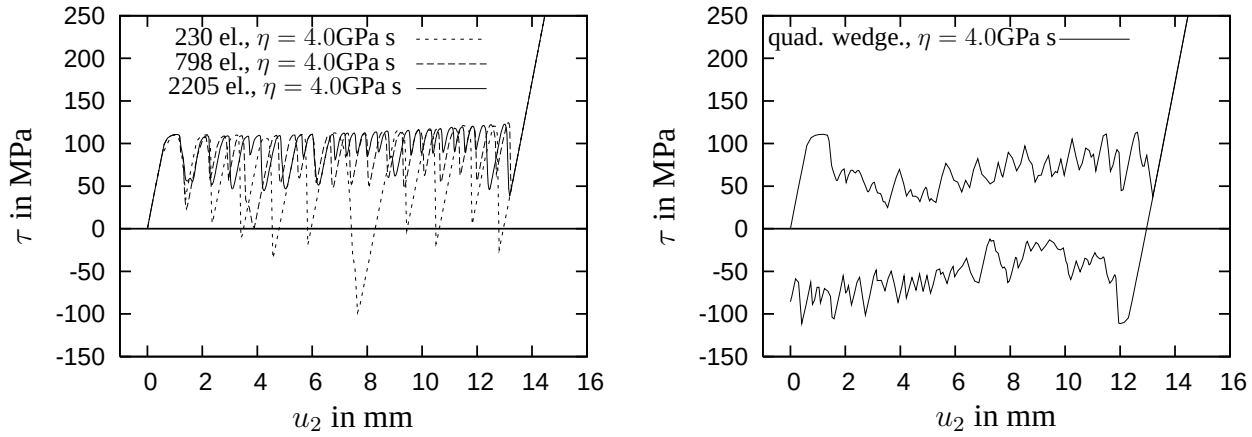

Figure 7.3: Nominal shear stress vs. displacement for different regular hexahedral meshes with linear shape functions (left) and for the quadratic wedge mesh (right). The nominal shear stress is given by $\tau = F/A$, where F is the overall reaction force in $\boldsymbol{e}_2$-direction on the displaced boundary, and the boundary area $A = 600\mathrm{mm}^2$.

reached again, and the nominal shear stress stays below the approximately constant peak level that is found in the regular mesh simulations. This behaviour is more realistic than the results with the regular meshing. The load drops are due to the mesh irregularity less pronounced.

The states depicted in Fig. 7.5 showing the twin shortly after nucleation give a good impression on the mesh-dependence in both simulations. It appears that in case of quadratic shape functions the mesh-dependence is less pronounced. The unrealistic thickening of the twin tips that are embedded according to the mesh interfaces are not encountered, and neither is the flipping of entire rows of elements.

While the overall behaviour is as expected and mostly satisfactory, observed problems should not be concealed. In the following, "regular twin" means a twin which aligns its interface parallel to the shear direction, while a kink twin aligns its interface perpendicular to the shear direction. The kink twins are not observed in practice. In Fig. 7.4 one notes that in the first place an intermediate twin evolves perpendicular to the shear direction. As the model is elastic, this twin vanishes as the deformation continues, and is replaced by the regular twin. The intermediate twin appears only in the mesh of medium fineness. Further, due to the energy invariance of conjugate twins, it is not clear whether the intermediate twin should be regarded as a kink-twin variant of the twin that is aimed for, or as a regular twin of the twin system that is conjugate to the targeted twin. The conjugate twin systems have their shear planes aligned almost perpendicular to each other, namely at 86.3°, while the mesh interfaces intersect at an angle of 90°. Due to the mesh morphology it is reasonable to suppose that a regular twin propagates along a mesh interface if its shear plane is approximately parallel to it, i.e., the propagation direction depends on the meshing. It is therefore recommendable to use irregular meshes in conjunction with the present material model, in order to not induce a preferred twin-interface alignment. Moreover, the use of quadratic shape functions appears to reduce the mesh-dependence as well. To review the mesh dependence in more detail, the nominal shear stress vs. displacement curve for three quadratic and irregular meshes of different fineness is depicted in Fig. 7.6. One sees that the discontinuity is less pronounced at the finest mesh, where the amplitude of the load drops is lowest.

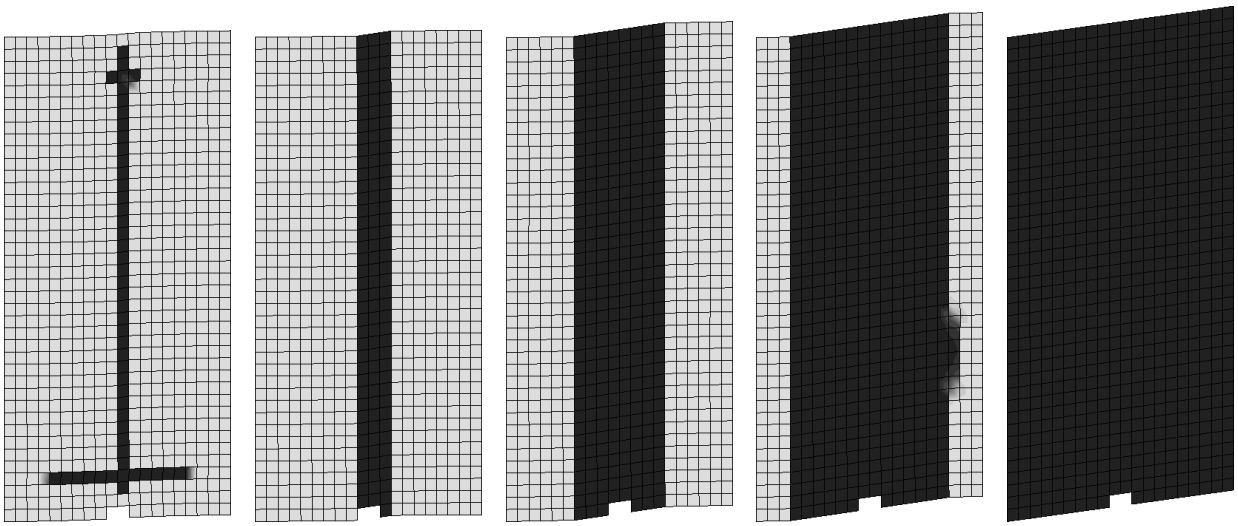

Figure 7.4: Twin evolution from left to right at u =2.7mm, 2.9mm, 6.7mm, 10.4mm and 13mm on the intermediate fine mesh. The greyscale displays the weight factor corresponding to the parent configuration, $(\text{white})\ 0 < a_0 < 1\ (\text{black})$. Note the intermediate twin at $u = 2.67$mm, and the propagation of the interface into the next row recorded at $u = 10.4$mm.

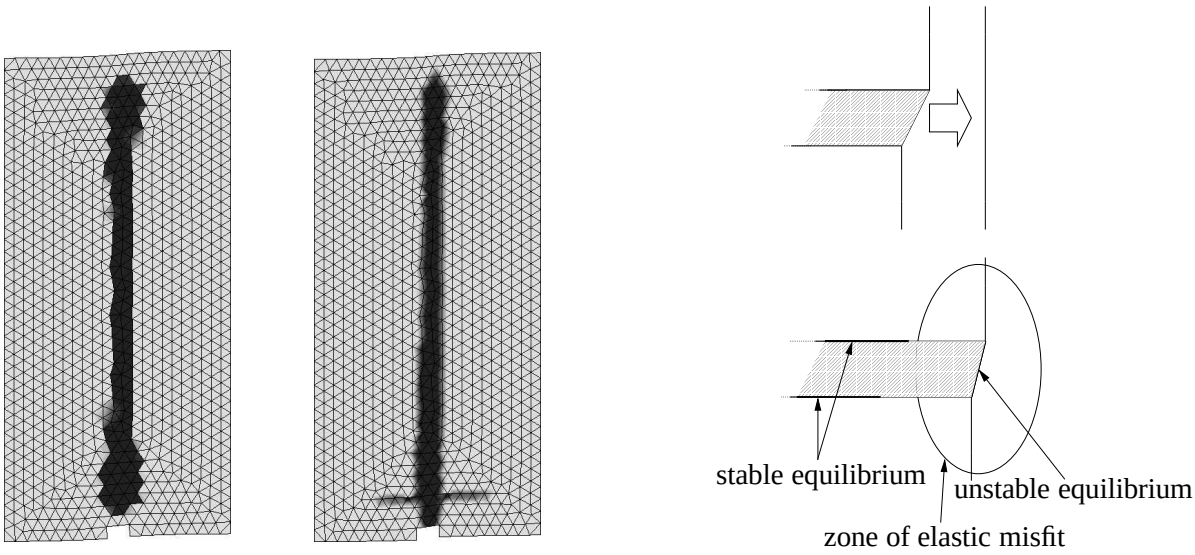

Figure 7.5: Twin shortly after nucleation in the linear (left) and the quadratic (right) wedge mesh.

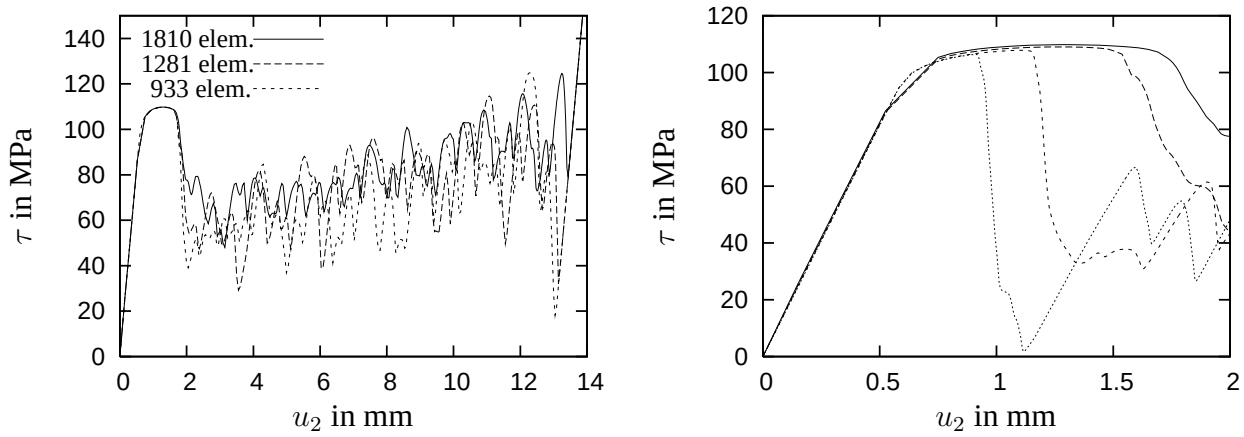

Figure 7.6: Nominal shear stress vs. displacement for the quadratic wedge meshes of different fineness (left) and different viscosities ($\eta = \{1000\text{MPas}, 2000\text{MPas}, 6000\text{MPas}, 10000\text{MPas}\}$, right). The smaller the viscosity, the earlier occurs the load drop.

Unsteady Twin Formation

The existence of a peak stress at the twin nucleation, and a lower propagation stress level is in accordance with observations and theoretical considerations (Christian and Mahajan, 1995; Kochmann and Le, 2009). It is responsible for the burst-like propagation of newly formed twins. This behaviour is similar to the stick-slip phenomenon encountered in dry-friction, and has been verified experimentally (Boyko et al., 1994; Kawabata et al., 2000) and by atomistic modelling (Hu et al., 2009).

Even though no nucleation stress has been explicitely accounted for, the burst-like propagation is observed in the simulations. It is interesting to note that neither the nucleation nor the propagation stress depend on the fineness of the mesh, see Fig. 7.6. From the simulations it can be concluded that the load drop from the nucleation to the propagation level occurs as soon as the twin tips reach the free boundaries, and the twin propagation by advancing the two interfaces towards the parent crystal starts. This behaviour is quite realistic. In the micrograph Fig. 1.1, one merely finds a free twin tip inside the grain, but only at the grain boundaries.

The equilibrium at the interface between twin nucleus and parent is unstable (see Fig. 7.5 for a sketch). A small perturbation, like external loading or internal stresses, lead to interface motion. The fact that the twin tip shoots through the sample instead of advancing proportionally with the application of the boundary conditions indicates that the elastic misfit strain caused by the twin triggers the twin propagation. The conclusion is that the elastic misfit can give the crucial stroke to the unstable equilibrium, which causes the observed shooting-through of the twin. In the simulations, the speed at which the twin tip shoots through is not infinite because of the viscous regularisation. A reduction of the viscosity results in a shorter nucleation stage, respectively a faster shooting-through of the twin, see Fig. 7.6. In FE-simulations with a domino-row arrangement of elements, the twin propagation speed has been found to be inversely proportional to the viscosity.

Summarising roughly, the discrepancy between nucleation- and propagation stress is partially caused by the elastic misfit strain around the twin nucleus, which pushes the neighbouring parent crystal towards the twin configuration. This results in a reduction of the stress that has to be applied to trigger

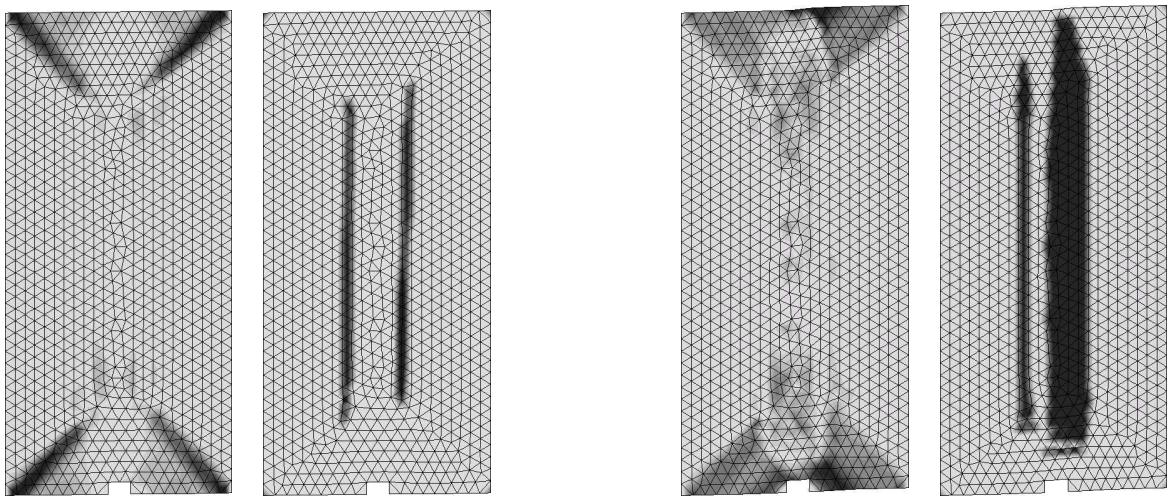

Figure 7.7: Slip twin interaction at $t = 82.5$s (left figures) and at $t = 224$s (right figures). In each pair of figures, the left figure displays the accumulated basal shear (0...0.05 and 0...0.1) while the right figure displays the twin volume fraction (0...1).

the twin propagation, compared to the loading that is necessary to generate a twin nucleus from the uniform parent crystal. The twin nucleation is controlled by the movement and agglomeration of partial dislocations, which may occur at stresses that depart significantly from the propagation stress of an evolved twin.

7.3.3 Incorporation of Basal Glide

If basal glide is activated, the plane deforms initially by slip bands, which start at the corners and end inside the plane. Then, two twins develop such that they connect the ends of the slip bands, see Fig. 7.7. The shear bands deviate slightly from the orientation $\pm 45°$with respect to the model edges, because the angle between the basal plane and the $\{10\bar{1}2\}$ plane (parallel to the displaced face) is $\approx 43.16°$.

7.4 FE Model 2: Elongation of a Notched Band

7.4.1 Model setup

The second FE model consists of a notched single crystal band, which is elongated along the length axis (Fig. 7.8). Again, a plane strain state is enforced by prescribing $u_1 = 0$ on the principal faces of the stripe, while the transverse displacement perpendicular to the thickness direction is not constrained. The notch is the inhomogeneity at which twins should nucleate. The hexagonal crystal lattice is aligned such that an edge of the base hexagon is parallel to the band normal, while the $\boldsymbol{c}$-axis deviates slightly from the length axis with the angle α. The non-zero displacement boundary condition is applied proportional to time, which runs from 0 to 1000s. Regular hexahedral meshings with linear and quadratic shape shape functions have been used (element types C3D8 and C3D20). The

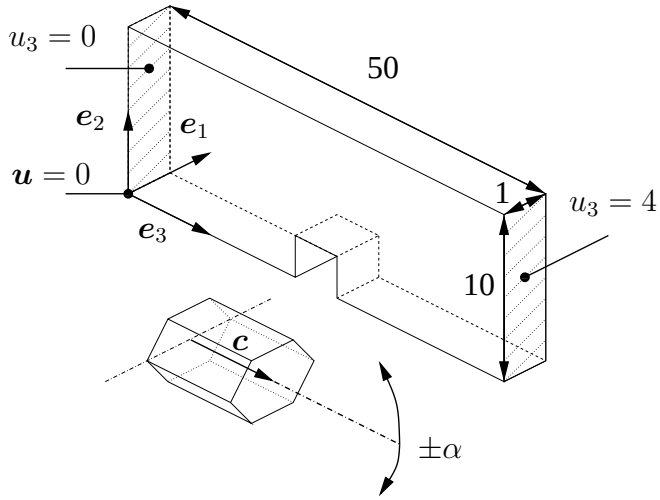

Figure 7.8: Model of a notched band (1x10x50).

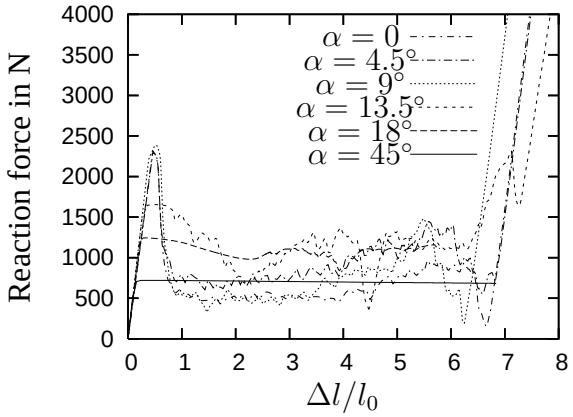

Figure 7.9: Reaction force over the nominal elongation strain for the monotonic elongation of the band using the wedge-mesh with quadratic shape functions and taking into account basal slip, $\gamma_{\text{twin}} = 0.05\gamma_0$. As α increases, basal slip is triggered instead of twinning. With $\tau_{\text{twin}} \approx 4\tau_{\text{basal}}$, the force necessary to elongate the band decreases. For $\alpha = 45°$, the elongation was entirely accomplished by basal slip.

regular meshing is considered as unproblematic, since the crystal orientation enforces an interface orientation which is far from parallel to the mesh interfaces.

7.4.2 Cyclic Loading and General Observations

A cyclic loading test has been employed in order to examine the detwinning characteristics and the effect of the phenomenological model adaptation. After loading the strip as depicted in Fig. 7.8, the loading has been reversed. Basal slip is disabled in the first place as well.

The band behaves initially linearly elastic. At a certain point, a twin nucleates at the notch, and propagates rapidly through the width of the specimen. With ongoing loading, it propagates along its thickness direction, i.e. the established interface moves through the sample. After the entire specimen is twinned, one observes again linear elastic behaviour. As the deformation is reversed, the behaviour is similar to the loading process. One observes linear elastic behaviour until the twin (which has initially been the parent) invades the specimen, and the initial state is restored. With the phenomenological model adaptation, one is able to limit the stress at which twinning takes place, which is depicted in Fig. 7.10. One important result is that the critical force at which the linear elastic stage ends is doubled as the critical twinning shear γ_{twin} is doubled, which suggests that a proportional scaling $\tau_{\text{twin}} \approx G\gamma_{\text{twin}}$ can be used for stresses and strains of relevant order. The simulations with regular and irregular meshes yield approximately the same results.

One notes that the reaction force level is not constant in the stage of twin or parent propagation, irrespective of the jerky behaviour. The reason for this is that the stress state changes qualitatively during

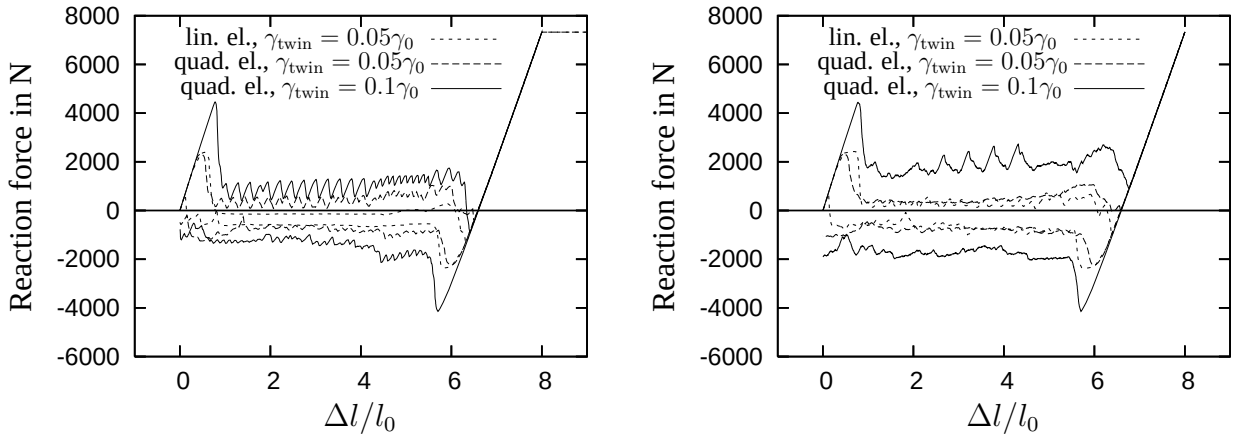

Figure 7.10: Reaction force over the nominal elongation strain for the cyclic elongation, for regular hexahedral meshes (left) and wedge-meshes (right).

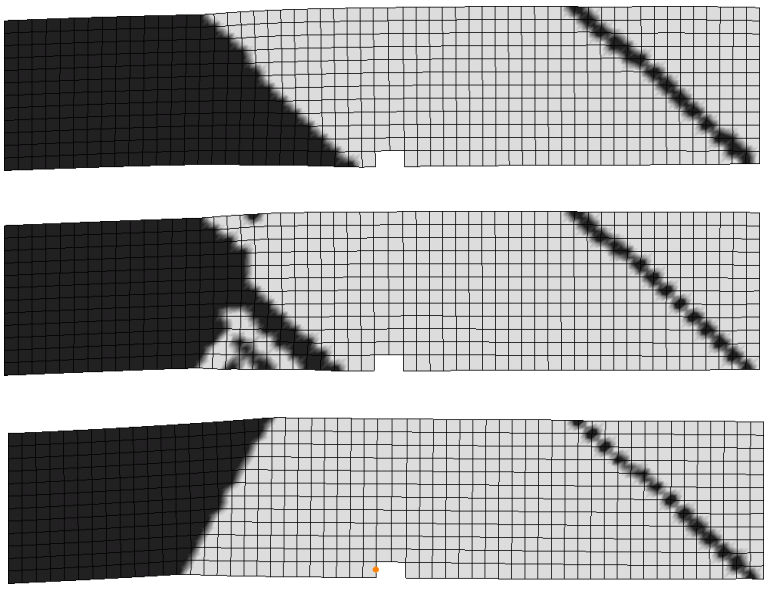

Figure 7.11: The interface alignment shifts to the orientation of the conjugate twin.

the loading. As the twin propagates, the band undergoes a shear deformation lateral to the elongation direction, which induces a small bending component. At load reversal, a slight necking is observed, causing again a small bending component. The change of the stress state is responsible for the sudden shifting of the interface, which has been observed in some calculations. Some exemplifying states are depicted in Fig. 7.11. The angle between the new and old interface is approximately 86°, which means that we do not face a kink twin, but a pair of conjugate twins. The prediction of such behaviour is a drawback of the elastic modelling. However, it is a minor problem in the primary loading stage, and only of matter if strain path changes occur on the twinned structure.

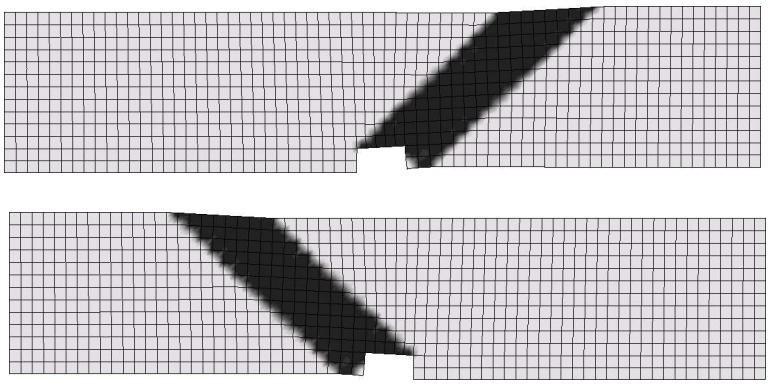

Figure 7.12: Plot of the weight factor a_0 of the parent, $0(\text{black}) < a_0 < 1(\text{white})$, for a positive and negative inclination of the lattice with respect to the elongation direction.

7.4.3 Distinction of Conjugate Twin Systems

Due to the energy invariance of conjugate twin systems, it is interesting to see how they can be distinguished in an FE simulation. For this purpose, the phenomenological model adaptation and basal slip have been deactivated. Therefore, the conjugate twin systems (the opposing twin systems in the hcp cell) are energetically not distinguishable (see Section 4.8). However, due to the asymmetry coming from the inclination of the crystal lattice with respect to the elongation direction, it has to be presumed that one twin system is preferred. In fact, one can clearly distinguish the twin bands that evolve, not by looking at both weight factors a_i or the strain energies w_i of the conjugate twin systems at a material point, but by relating the interface that evolves to the crystal basis. The conjugate twin systems can be triggered by inclining $\boldsymbol{c}$ by a small positive or a negative α, see Figs. 7.8 and 7.12. Inside the twin lamella the weight factors of the two equivalent twin systems are both approximately 0.5. The interface alignment clearly determines which of the conjugate twins has evolved, while the weight factors are equal for any deformation. In fact, by cancelling out one of the two conjugate twin systems in each of the three pairs, the FE calculation is not altered at all. Thus, the conjugate twin systems can be treated as one twinning mode.

One problem with the conjugate twin systems is that one twin may be bounded by interfaces belonging to the two distinct conjugate twins, as depicted in Fig. 7.13. The simulation has been carried out at a ten times larger elongation rate. It is observed that two regular conjugate twins unite to a mixed twin, which is an artifact of the model. The mixed twin is at least unstable and shifts quite fast to a regular twin.

In one case, a rather unexpected result has been encountered, namely the force displacement curve for the regular mesh with linear shape functions. In this simulation, the reaction force is not jerky, and in the first propagation stage it is negative, see Fig. 7.10. The implications of this are that the twin grows by itself, exerting a compressive force to the band, which contradicts physical experience. An explanation for this may be that an unfortunate combination of model parameters has been chosen. This suspicion is furnished by the fact that in no other simulation with a qualitatively better FE model such behaviour is observed.

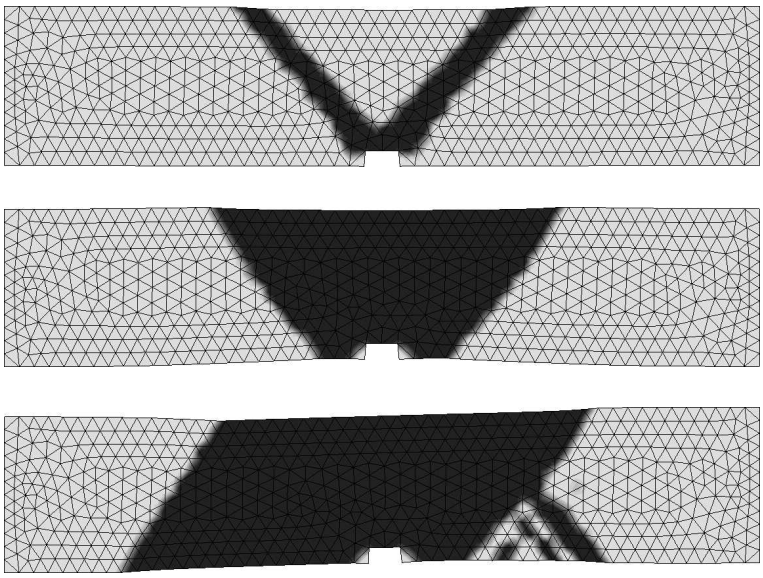

Figure 7.13: Plot of the weight factor a_0 of the parent, $0(\text{black}) < a_0 < 1(\text{white})$. The elastic modelling induces artificial deformation modes, namely the interface shifting between conjugate twins and the union of conjugate twins.

7.4.4 Incorporation of Basal Glide

In this Section, the twin-basal glide interaction is studied. The critical shear stress for basal glide is determined such that $\tau_{\text{twin}}/\tau_{\text{slip}} \approx 4$ holds. With $\gamma_{\text{twin}} = 0.05\gamma_0$, yielding $\tau_{\text{twin}} \approx 110$MPa, $\tau_{\text{slip}} = 30$MPa has been chosen. These values are larger than the values for pure magnesium, but reasonable for MgAl alloys. The elongation test has been carried out at $\alpha = 0$, 4.5°, 9°, 13.5°, 18° and 45°.

As expected, the basal slip activity depends on the inclination of the lattice. The simulation at $\alpha = 0°$ is practically unaffected by the incorporation of basal slip, since the basal plane is perpendicular to the tension direction. While the twin nucleates and propagates, marginal slip activity is observed near the twin interface. As the twin interfaces reach the ends of the bar, more slip system activity is observed due to the fact that the boundary conditions at the ends of the band are incompatible with the twinning shear. The increased slip induces a less homogeneous parent structure, which triggers the evolution of a twin network at load reversal (Fig. 7.14).

For $\alpha = 4.5°$ and $\alpha = 9°$, similar behaviour with more pronounced slip activity is observed. For $\alpha = 13.5°$, slipping and twinning interact already in the loading stage. Soon after the twin nucleates, a considerable amount of slip occurs near the twin tip (Fig. 7.15). Moreover, the twin tip has a pronounced cusp shape, as often observed in real crystals, and predicted by the theory of transformation dislocations (Boyko et al., 1994). A slip band propagates at an angle of approximately 17.5° to the elongation direction, which is approximately parallel to the $\boldsymbol{c}$-axis. From this band, a distinguished zone of large slip deformation evolves, which acts as a barrier for the twin propagation (Fig. 7.15). Again, the major problem with the elastic modelling of twinning becomes visible. In the upper left subfigure in Fig. 7.15 one sees that the band undergoes a downward lateral deformation. In the final stage, the lateral shearing is upward. This means that the twin must have changed to its conjugate between the two states.

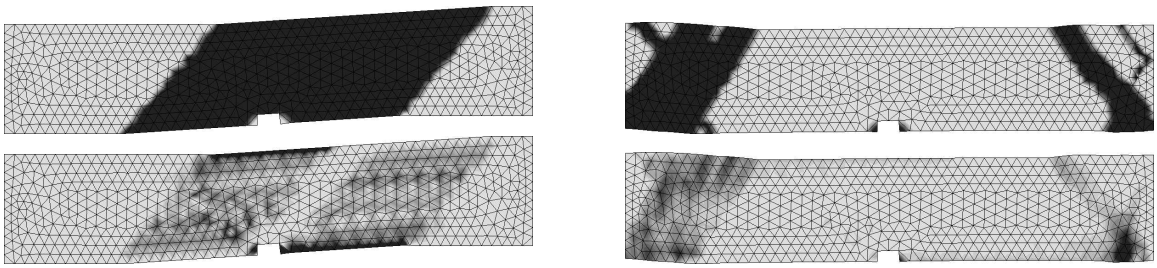

Figure 7.14: Twin and basal slip evolution for the elongation test with $\alpha = 0°$. Top: Plot of the weight factor a_0 of the parent, $0(\text{black}) < a_0 < 1(\text{white})$. Bottom: Plot of the accumulated basal shear strain, from 0...0.025 in the left and 0...0.2 in the right figure. At the loading stage, the twin grows homogeneously into the parent, accompanied by slight basal slip. At the end of the loading stage basal slip is enforced at the band ends, which leads at load reversal to a heterogeneous twin structure (right).

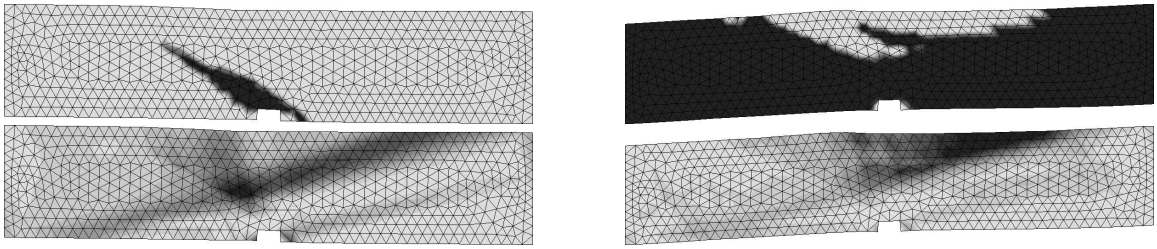

Figure 7.15: Twin and basal slip evolution for the elongation test with $\alpha = 13.5°$. Top: Plot of the weight factor a_0 of the parent, $0(\text{black}) < a_0 < 1(\text{white})$. Bottom: Plot of the accumulated basal shear strain, from 0...0.15 in the left and 0...0.4 in the right figure. Note the cusp shape of the twin tip and the slip activity near the twin tip. The slip zone stretches to a slip band, which acts later as a boundary for twin growth.

In case of $\alpha = 45°$, slip bands evolve, and the deformation is entirely accommodated by basal slip, and no twinning is observed, Fig. 7.16. The critical force is approximately one fourth of the critical force in case of $\alpha = 0$, i.e., one recovers the ratio $\tau_{\text{twin}} \approx 4\tau_{\text{basal}}$.

The model setup is appropriate for further investigations, e.g., whether slip and twin interaction produce accommodation kinking. For magnesium, kink patterns are well documented by Roberts and Partridge (1966). It is found that two $\{10\bar{1}2\}$ twins that grow from the surface and meet inside the crystal enclose a triangle, in which accommodation kinking by a certain slip pattern is observed. This somewhat specific twin-slip-pattern can be reproduced successfully in a FE Simulation, see Fig. 7.17. The regular quadratic mesh has been used, with $\tau_{\text{twin}} \approx 110$MPa, $\tau_{\text{basal}} = 30$MPa and $\alpha = 0$.

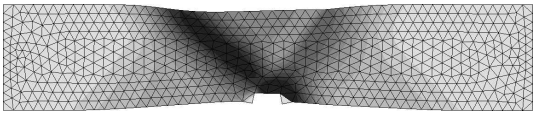

Figure 7.16: Plot of the accumulated basal shear strain from 0...0.5, at $\alpha = 45°$. The entire elongation is accommodated by a slip band, and no twinning is observed.

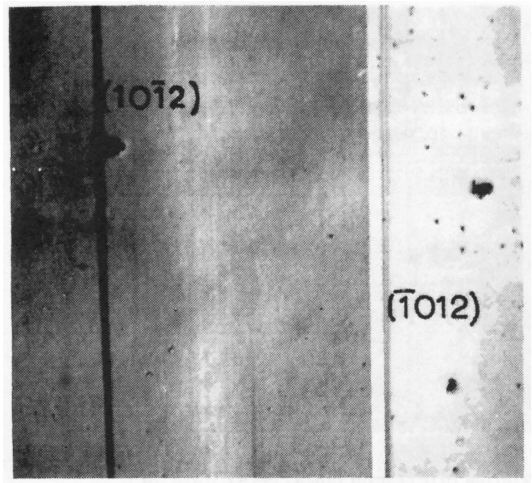

(a) Growth when the twins converged beneath the surface. ×300

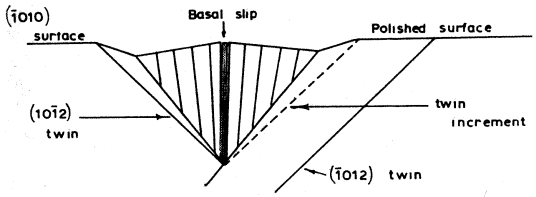

(b) Schematic section of (a) normal to the specimen surface: tilts exaggerated.

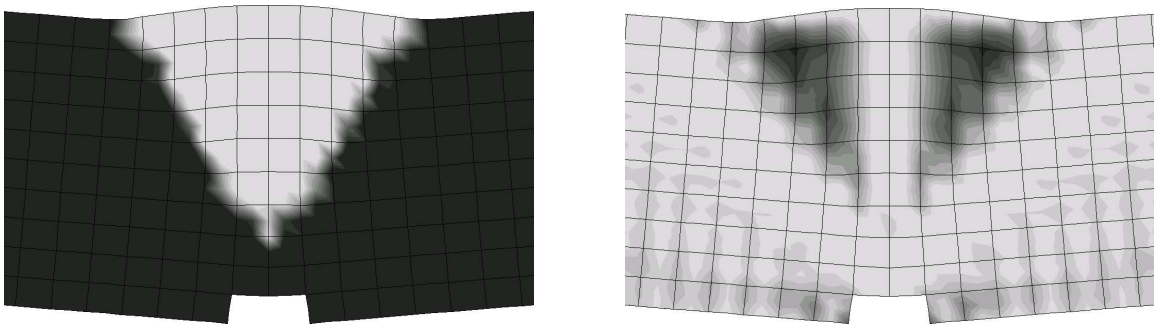

Figure 7.17: Kink pattern observed by Roberts and Partridge (1966) and simulated kink pattern. The deformation is scaled by a factor of two in order to magnify the kinks. Left: Plot of the weight factor a_0 of the parent, $0(\text{black}) < a_0 < 1(\text{white})$. Right: Plot of the accumulated basal shear strain, from 0...0.08.

7.5 FE Model 3: Simple Shear of a Plane

7.5.1 Model Setup

While the latter FE simulations result in approximately homogeneously loaded parts of twin and parent, in this section the effect of inhomogeneous loading conditions is examined. For this purpose, a 200mm $\times$ 100mm plane is subjected to a simple shear deformation, and the lattice is aligned such that the twin interfaces disturb the section-wise homogeneous deformation, unlike to the simulations of the two latter sections, see Fig. 7.18. Again, the deformation is restricted to be plane. One of the short edges is kept fixed while the opposing one is displaced proportional by 20mm parallel to the fixed one. The displacement occurs time proportional in 1000s. If the lattice is oriented such that a rotation of 180° inside the plane is element of the symmetry group of the lattice, the model is point-symmetric with respect to the plane centre point. The lattice is oriented such that the shear direction is parallel to $\boldsymbol{c}$ while the model plane normal coincides with one of the $\boldsymbol{a}_i$. Therefore, only one half of the model has been incorporated, namely a 100mm $\times$ 100mm sheet, where the midpoint of one edge is fixed, while the opposing face is displaced 10mm parallel the fixed edge. Along the fixed edge, $\boldsymbol{u}(d) = -\boldsymbol{u}(-d)$ holds, where d runs from -50mm to 50mm, see Fig. 7.18. A regular 50 $\times$ 50 mesh with quadratic elements has been used. The regular mesh is regarded less problematic in this simulation, as the mesh interfaces intersect the twin interface at an angle of approximately 45°. A regular hexahedral meshing with quadratic shape functions (element type C3D20) has been employed.

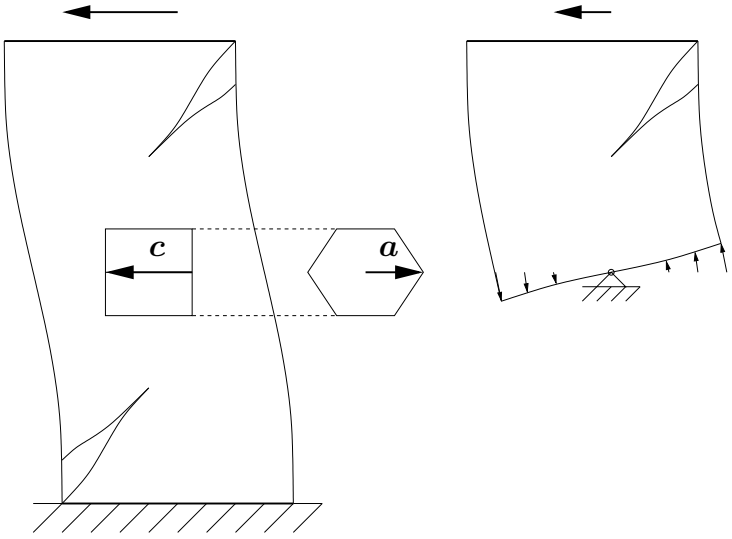

Figure 7.18: Model of a plane (200mm$\times$ 100mm) that is subjected to a simple shear deformation. The hexagonal crystal lattice is aligned such that the edge of the base hexagon is perpendicular to the model plane while the $\boldsymbol{c}$-axis is parallel to the shear direction. The boundary conditions are such that the deformation is plane.

7.5.2 Simulation Results without Basal Slip

In the simulations, a twin nucleates in one corner and rapidly propagates diagonally halfway through the plate. Then, as the loading continues, it grows thicker at the nucleation site while the tip of the twin remains sharp. Consequently, a cusp-shaped twin develops, with its interfaces slightly inclined to the $\{10\bar{1}2\}$ shear plane. However, the interfaces cannot be inclined beyond a certain angle, which depends on the twinning stress. After reaching the critical inclination, the twin breaks up into several twins, see Fig. 7.19. In Fig. 7.20, the twin shape just before the splitting of the twin is depicted for different twinning stresses. One notes that the larger the twinning stress is, the larger is the maximum interface inclination. This result is in agreement with analytical findings by Glüge and Kalisch (2008). Moreover, the cusp-shape of a twinning tip is predicted by the considerations regarding the dislocation nature of twinning (Boyko et al., 1994), and observed experimentally as well, see Fig. 7.21.

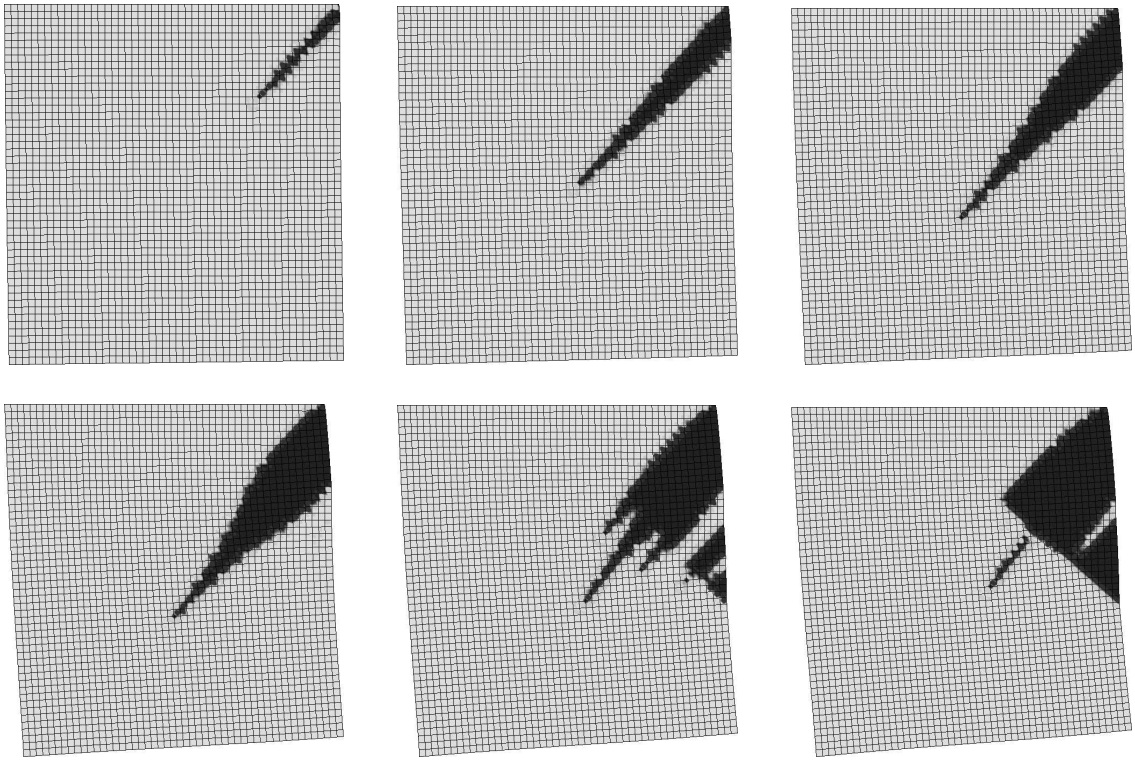

Figure 7.19: Twin growth and breakup for $\tau_{\mathrm{twin}} \approx 240$MPa, model depicted at 143s, 283s, 432s, 605s, 695s and 800s. Plot of the weight factor a_0 of the parent, $0(\mathrm{black}) < a_0 < 1(\mathrm{white})$.

7.5.3 Incorporation of Basal Glide

If basal slip is incorporated, the single-crystal simulations are very sensitive with respect to the initial conditions. At $\tau_{\mathrm{basal}} = 30$MPa and $\tau_{\mathrm{twin}} = 120$MPa, a very small twin evolves, while the deformation is accommodated by basal slip in the large, see Fig. 7.22. If the lattice is slightly rotated (9° around the plane normal), the twin invades the plane, and the slip-twin interaction at the twin tip can be studied, see Fig. 7.23. One notes that the cusp-shape of the twin is practically lost. The reason for this is that basal slip accompanies the advancing twin tip, as the twin grows along the $\{10\bar{1}2\}$ shear plane. By crystallographic glide, large stresses are relaxed, as it acts as an additional deformation

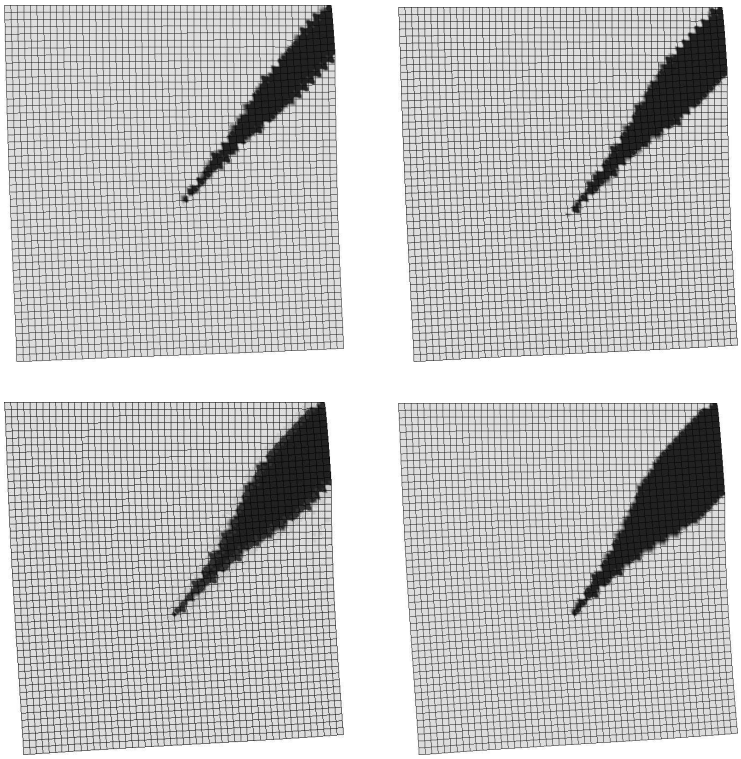

Figure 7.20: Twins shortly before breakup for a twinning stress of 60MPa (387s), 120MPa (484s), 240MPa (605s) and 360MPa (658s). Plot of the weight factor a_0 of the parent, $0(\text{black}) < a_0 < 1(\text{white})$.

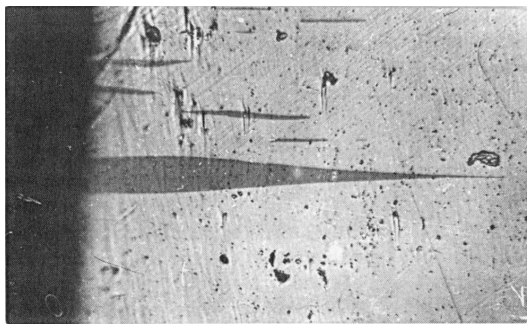

Figure 7.21: Real twins may exhibit a cusp-shaped twin tip (courtesy of Boyko et al. (1994)).

mechanism to twinning. Large stresses are found at the twin tip and along the interface, where the stresses increase monotonously with the interface inclination, which is an important ingredient for the cusp shape of the twin tip. In Fig. 7.23., one notes that there exist zones where the twin occupies zones of prior crystallographic slip.

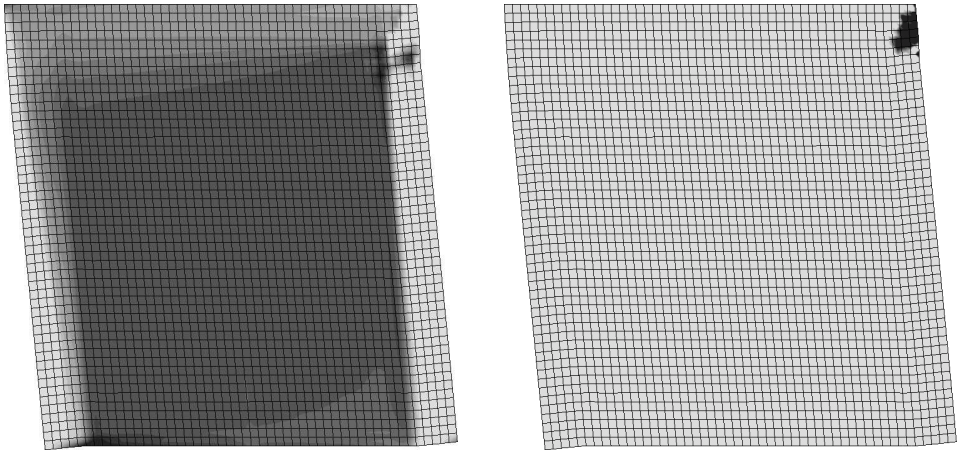

Figure 7.22: If basal slip is incorporated, the deformation is mainly accommodated by basal slip, and only a small twin tip remains. $\tau_{\text{twin}} = 120$MPa, $\tau_{\text{basal}} = 30$MPa, at 1000s. Left: accumulated basal shear strain, from 0...0.15, right: Plot of the weight factor a_0 of the parent, $0(\text{black}) < a_0 < 1(\text{white})$.

7.6 FE Model 4: Simple Compression of an RVE

In order to obtain results that are comparable to experimental data, the RVE method is used to simulate the simple compression of an extruded magnesium alloy along the extrusion direction. The crystallographic texture of the latter is such that the $\boldsymbol{c}$-axes are aligned approximately perpendicular to the extrusion direction, i.e., the compression along the extrusion direction results in $\boldsymbol{c}$-axis elongation, which is accommodated by $\{10\bar{1}2\}\langle\bar{1}011\rangle$ twinning (see Jiang et al. (2007); Al-Samman and Gottstein (2008)).

7.6.1 Model Setup

The FE model of the RVE consist of a regularly meshed cube with 30×30×30 linear hexahedron elements. The initial microstructure has been approximated by a periodic Voronoi tessellation, consisting of 20 grains, Fig. 7.24. The limited number of grains is necessary to provide a reasonable discretisation of each grain, since the grains are partitioned by twinning. The crystal orientations are restricted such that the $\boldsymbol{c}$-axes do not deviate more than α from the plane of compression, and are uniformly distributed. No preferred orientation of the remaining degree of freedom (rotating the $\boldsymbol{a}_i$ around the $\boldsymbol{c}$-axis) has been established. The displacement boundary conditions are periodic on the entire surface of the cube. To exclude shear deformations with respect to the orthonormal base system used for the model description, the off-diagonal components of the mean displacement gradient have

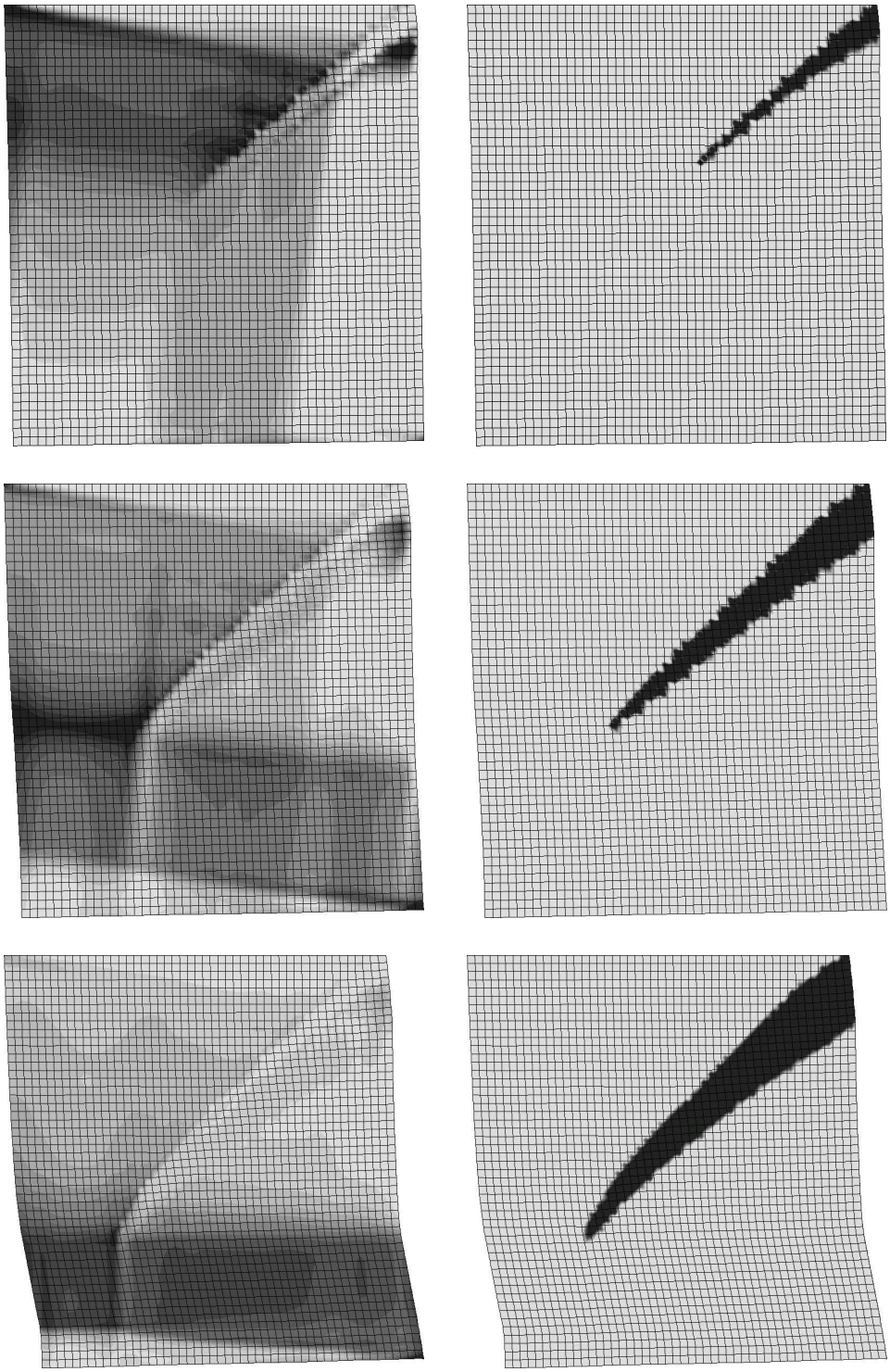

Figure 7.23: Slip-twin interaction at the tip of the twin, $\tau_{\text{twin}} = 120\text{MPa}$, $\tau_{\text{basal}} = 30\text{MPa}$, states depicted at 223s, 443s and 1000s (from top to bottom row). Left: accumulated basal shear strain, 0...0.0375 (top), 0...0.075 (centre) and 0...0.25 (bottom). Right: Plot of the weight factor a_0 of the parent, $0(\text{black}) < a_0 < 1(\text{white})$.

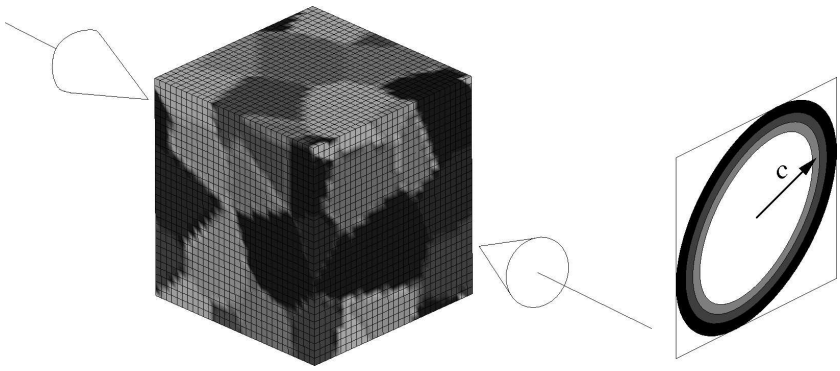

Figure 7.24: FE Model of the RVE, with schematic pole figure of the $\boldsymbol{c}$-axes. The greyscaling exemplifies the periodic Voronoi structure of the grains.

been constrained to be equal to zero. Further, the 11-component has been constrained,

$$\boldsymbol{H} = \begin{bmatrix} f(t) & 0 & 0 \\ 0 & \cdot & 0 \\ 0 & 0 & \cdot \end{bmatrix} \boldsymbol{e}_i \otimes \boldsymbol{e}_j, \tag{7.10}$$

while H_{22} and H_{33} have not been constrained. Instead, the mean reaction forces along the $\boldsymbol{e}_2$ and $\boldsymbol{e}_3$ directions have been constrained at the corresponding faces to be equal to zero, in order to obtain the average uniaxial stress state along the $\boldsymbol{e}_1$ direction.

7.6.2 General Observations

In the simulations, twins nucleate and spread rapidly over the FE model. In Fig. 7.25, the propagation of a twin over a grain boundary is illustrated. In Fig. 7.26, a sequence of states illustrating the twin spreading in the RVE is given. Both Figures are obtained from the simulation with a maximum deviation of $\alpha = 30°$of $\boldsymbol{c}$ from the plane of compression. The incorporation of basal glide does not significantly aller the results, which is due to the approximately perpendicular alignment of the basal planes to the principal stress direction. In Fig. 7.27, two deformation states of the RVE are depicted.

7.6.3 Comparison to Experimental Findings

As a reference, the works of Reed-Hill (1973) and Jiang et al. (2007) have been used, where compression tests for two magnesium alloys and pure magnesium are documented. In Fig. 7.28, graphs for the twin volume fraction evolution in the experiments and the simulations are depicted. One notes that the evolution of the twin volume fraction is in good agreement with the experimental findings. The rapidly increasing twinning rate at 3 to 5% of logarithmic strain, as well as the saturation to 100% twin volume fraction are captured by the model. In Figs. 7.28 and 7.29, the twin volume fraction and the nominal compression stress are plotted. Therefore, it is to be expected that the crystallographic texture evolution is in good accordance, as twinning dominates the texture evolution for this particular experiment.

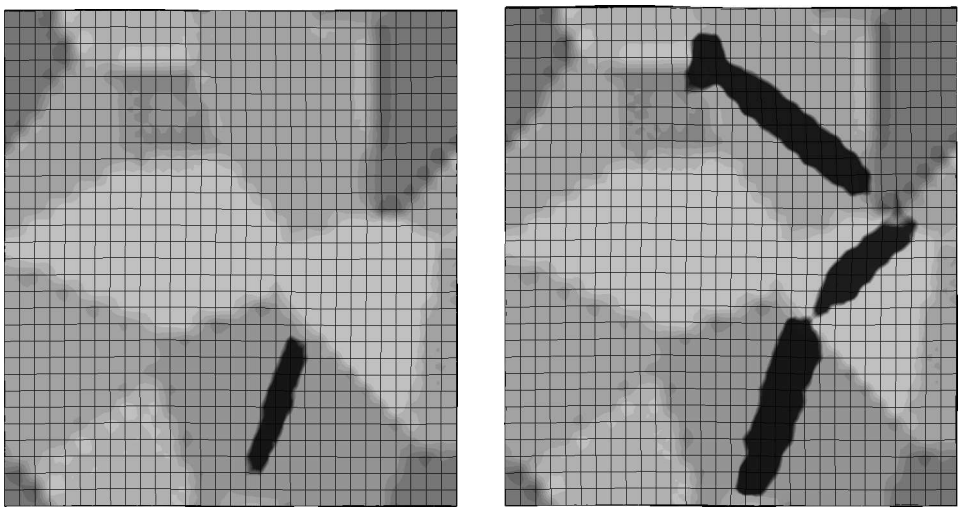

Figure 7.25: Propagation of a twin (black) over a grain boundary. The greyscaling represents the grain structure.

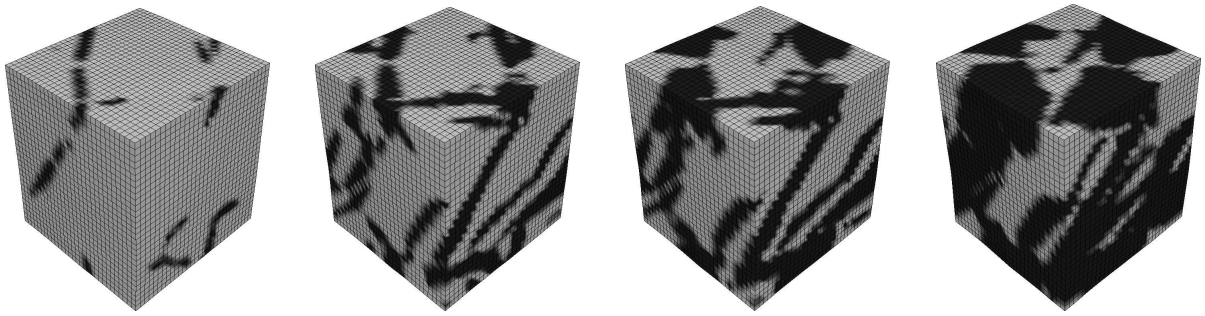

Figure 7.26: Twin spreading on the RVE, at a nominal compression strain of 2%, 2.6%, 3.12% and 4.3%, from left to right.

Figure 7.27: Twin spreading on the RVE, at a nominal compression strain of 3.3% and 4%. The greyscaling indicates the grain structure. The twins are the dark areas, while the accumulated basal slip is depicted by the contour lines (0 to 0.004 in the left and 0 to 0.06 in the right figure).

However, comparing to the stress strain response given by Jiang et al. (2007), one finds that the experimental results display a pronounced hardening behaviour, which is not found in the simulations. This is due to the fact that the hardening behaviour of the magnesium alloy under consideration is very complex due to precipitates (see Section 2.10), which is not captured by the model. This explanation is furnished by the fact that the stress strain response is in considerable agreement with the compression experiments with pure magnesium (Reed-Hill, 1973), which displays a less complicated hardening behaviour due to its lack of precipitates, see Fig. 7.29. For this simulations, the critical stresses for twinning and slip have been adjusted by $\gamma_{\text{twin}} = 0.006\gamma_0$ to $\tau_{\text{twin}} \approx 13$MPa and $\tau_{\text{basal}} = 4$MPa. It is found that the zero-hardening-plateau at approximately 60 MPa (≈ 8.7 ksi) corresponds to the twin nucleation stage. At approximately 3% of logarithmic strain, the nominal stress increases constantly, which coincides with the point where volume-filling twinning starts seriously. Similar findings are given by Muránsky et al. (2009). The hardening is explained by the fact that the twins form firstly at stress concentration points, or expressed differently, at the most favourable twinning sites. For further twinning, the loading must be increased in order to activate the less favoured twinning sites. One notes that the hardening rate is overpredicted in the simulations. This is due to the fact that the material model does not capture secondary twinning and slip inside the twins, which renders them stiffer as in reality.

7.6.4 Texture evolution.

The RVE-simulations allow to compare the texture evolution with experimental results. At a material point, the significant orientation is assumed to be given by the parent or twin variant with the smallest strain energy. Due to the phenomenological model adaptation, the strain energy invariance is not exactly met by the model, i.e. a definite orientation can be extracted at each of the 8×30^3 integration

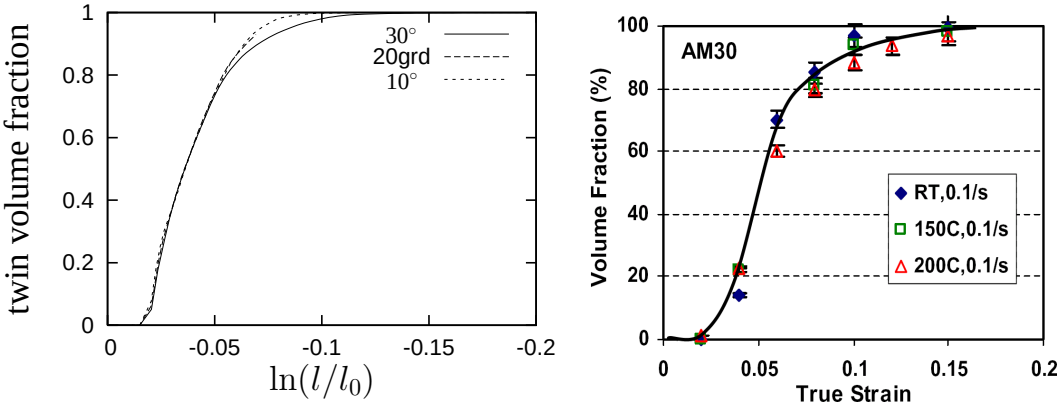

Figure 7.28: Comparison of the experimental (Jiang et al., 2007) and the RVE-simulated twin volume fraction evolution. The simulated curves are obtained with different texture sharpnesses, the maximum deviation of the $\boldsymbol{c}$ axes from the compression plane is given.

points of the FE model. The $\boldsymbol{c}$-axes of 20 initial orientations deviate at most by 15° from the compression plane, see Fig. 7.30 for pole figures of the initial orientation distribution. The sequence of $\boldsymbol{c}$ and $\boldsymbol{a}$ pole figures for the compression test is given in Fig. 7.31. One notes that the texture evolution corresponds qualitatively well to experimental results of Jiang et al. (2007), although the rate at which the texture shifts is overestimated.

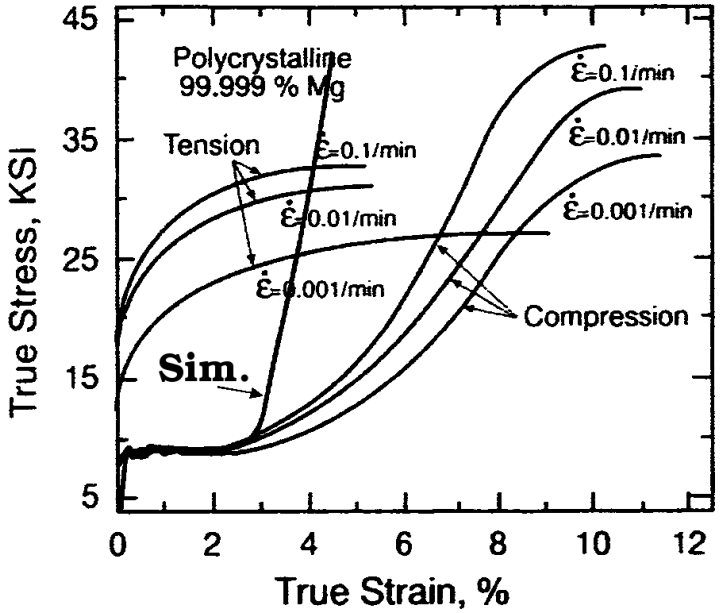

Figure 7.29: Comparison of the experimental (Reed-Hill, 1973) and the RVE-simulated stress evolution (Cauchy stress over logarithmic strain).

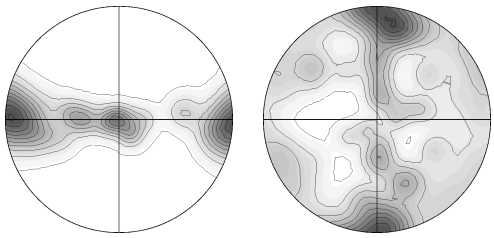

Figure 7.30: $\boldsymbol{c}$ and $\boldsymbol{a}$ pole figures of the initial orientation distribution, with $I_{\boldsymbol{c}\max} = 9.403$ and $I_{\boldsymbol{a}\max} = 5.173$. The projection plane is parallel to the compression direction. The pole figures are calculated using a Mises-Fisher distribution (Fisher, 1953) with a half-width of 20° around the individual orientations.

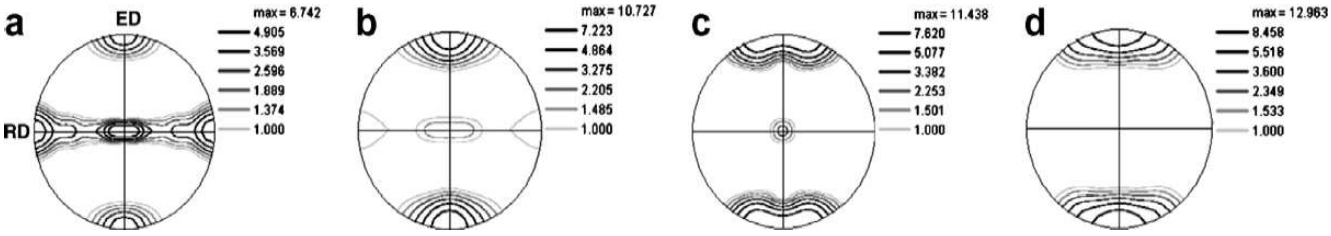

Experimental $\boldsymbol{c}$ pole figures measured by Jiang et al. (2007) at ε_0 of -4%, -8% -11% and -15%.

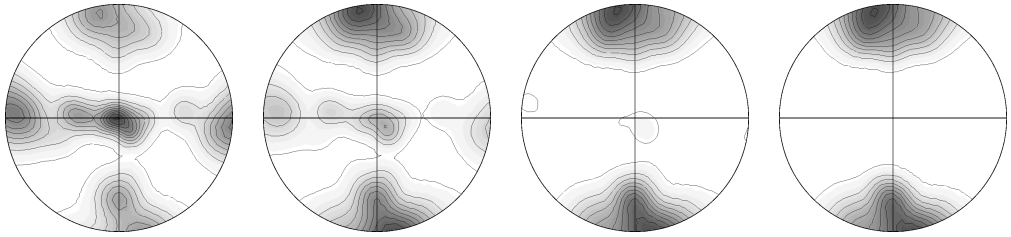

$I_{\max} = 6.78$ $I_{\max} = 8.05$ $I_{\max} = 10.99$ $I_{\max} = 11.23$

simulated $\boldsymbol{c}$ pole figures

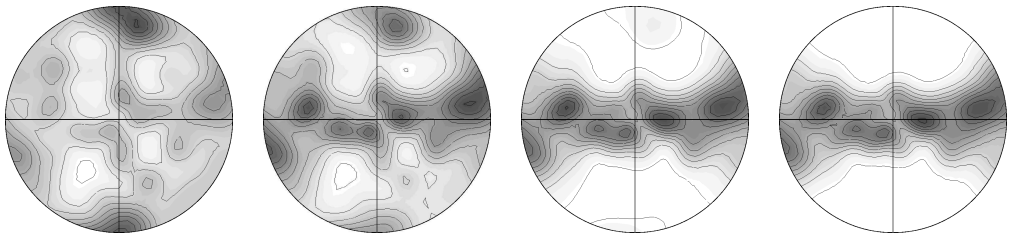

$I_{\max} = 3.95$ $\varepsilon_0 = -2.9$ | $I_{\max} = 3.03$ $\varepsilon_0 = -4.8$ | $I_{\max} = 3.71$ $\varepsilon_0 = -8.2$ | $I_{\max} = 3.79$ $\varepsilon_0 = -14.2$

simulated $\boldsymbol{a}$ pole figures

Figure 7.31: $\boldsymbol{c}$ and $\boldsymbol{a}$ pole figures for the compression test. The projection plane is parallel to the compression direction. The pole figures are calculated using a Mises-Fisher distribution with a half-width of 20° around the individual orientations.

Chapter 8

Summary and Outlook

Summary. In the first part of this work, twinning is analysed by geometrical considerations in simple lattices. It is shown that all compound twins exhibit an elastic energy invariance, which holds practically for all technologically interesting twinning modes. The existence of an energy invariance for certain twinning modes has been found by Ericksen (1984b); Zanzotto (1992, 1996). However, it appears that the statement that all compound twins obey the energy invariance is new. The cases that the compound twins are crystallographically equivalent or distinct and its consequences for the elastic modelling of twinning have been discussed.

The strain energy invariance enforces a treatment of pairs of conjugate twins as one twinning mode if modelled by means of elasticity. Although not distinguishable at each material point, one can clearly recognise each of the conjugate twins by the interface alignment that is established. It is to expect that the elastic modelling works not for crystallographically distinct conjugate twins. This is because one has to treat them due to the energy invariance as one twinning mode, although they may feature different properties. The strain energy invariance may even connect a regular twinning mode to a lattice invariant shear. However, due to the high symmetry of the cubic, tetragonal and hexagonal crystals, many compound twins are crystallographically equivalent, e.g., $\{112\}\langle 11\bar{1}\rangle$ twinning in the bcc, $\{111\}\langle 11\bar{2}\rangle$ twinning in the fcc (the TWIP-twins in manganese-alloyed steels), $\{\bar{1}012\}\langle 10\bar{1}2\rangle$ twinning in hcp (extension twinning), $\{101\}\langle 11\bar{1}\rangle$ twinning in the bct and othorhombic, $\{100\}\langle 00\bar{1}\rangle$ in the orthorhombic lattice, the pairs of conjugate twin systems of which are treatable as one twinning mode.

In the second half of this work, an elastic material model for twinning is developed. It consists in its core of a quadratic strain energy, which is extended by the isomorphy of the elastic law and the Ball and James-approach (Ball and James, 1987) to a piecewise quadratic nonconvex elastic energy. To obtain a continuously differentiable strain energy, a regularisation for the latter is introduced. Further, to adapt the twinning-stresses, a phenomenological model adaptation which relies on the Schmid law is introduced. In order to avoid the ill-posedness of the pseudoelastic boundary value problem, the viscous regularisation is used. The model is applied to the $\{10\bar{1}2\}\langle\bar{1}011\rangle$ twinning in the hcp lattice, the twinning stress and the c/a ratio are close to common magnesium alloys. As hcp crystals undergo readily crystallographic glide in the basal plane, the visco-elastic model is extended by the card glide mechanism, which allows plastic deformations by basal slip in the parent crystal.

The model is tested in various finite element simulations. It is able to predict the nucleation and prop-

agation of the twins. The stress-drop observed shortly after the nucleation (Christian and Mahajan, 1995) and predicted by Kochmann and Le (2009) is found in the simulations as well. The predicted cusp-shape of the twin tips are in accordance with experimental findings and conclusions from the theory of transformation dislocations (Boyko et al., 1994). Moreover, it is found that the interface inclination with respect to the shear plane is limited by the critical twinning stress, which is concluded from a stress jump analysis as well (Glüge and Kalisch, 2008). In conjunction with the basal slip mechanism, the model is able to predict the kink patterns observed by Roberts and Partridge (1966). The model is used in a simple compression simulation of an RVE, where the orientation distribution is similar to the one that is experimentally observed in extruded magnesium. It is found that the predicted twin structure is quite realistic. It is observed that due to the misfit strains the twins propagate across grain boundaries. The average twin volume fraction corresponds well to experimental findings of Jiang et al. (2007). Therefore, as the texture evolution is linked directly to the twin volume fraction, the texture evolution due to twinning is reproduced as well. Due to the complicated hardening behaviour owed to twin-particle interactions, the hardening rate of Magnesium alloys is underestimated. In the stage of extensive twinning, the model predicts a zero hardening plateau, which is in accordance to experimental observations on pure magnesium, i.e. when no twin-particle interactions are present. At the end of the stage of extensive twinning, the stresses are overpredicted in both cases. This is due to the lack of deformation mechanisms like secondary twinning and slip inside the twins, and the lack of a damage criterion.

However, the elastic modelling induces some difficulties. The most problematic fact is that twinning is connected to the movement of partial dislocations. This induces a strain path-dependence and energy dissipation, which are neglected by any pseudoelastic modelling. Moreover, the strain energy invariance of conjugate twins restricts the elastic modelling to crystallographically equivalent conjugate twins. Although the conjugate twins can be distinguished clearly in the FE simulations by considering the interface orientation, the elastic modelling leaves the possibility that a twin turns over into its conjugate twin. Such behaviour is not realistic due to the kinetic process underlying the twin formation. The conclusion is that the pseudoelastic modelling cannot be applied if severe strain path changes occur.

Outlook. One disadvantage of the model, namely the necessity of the phenomenological adaptation for reasonable twinning stresses, comes from the Ball and James-approach. I see basically two possibilities of how the model could be advanced.

Instead of modifying the elastic law, one could think of introducing an internal variable, which evolves according to a nucleation criterion and a kinetic relation. This could be a small twinned volume at the time of nucleation, the interface of which moves according to the kinetic relation. It is to expect that such a modelling strategy is very challenging from the practical point of view.

Another method could be to derive the elastic strain energy from molecular dynamics or molecular statics simulations instead of postulating it. If one constrains the atomic arrangement to be periodic, it should be possible to derive a strain energy by summing up atomic potentials from deforming a small reference cell. If one applies Born's rule, in a molecular statics calculation, the strain energy would emerge straightforward and display energy minima for shuffle-free twinning modes. Unfortunately, for the twinning modes involving shuffling, one has to abandon Born's rule, which means that the motion of the atoms has to be tracked. Such a two-step homogenisation is as well challenging from the practical point of view, but it may be capable to model a variety of phenomenas observed in

crystals by only a few physically conclusive equations.

Bibliography

Abeyaratne, R., Knowles, J., 2006. Evolution of Phase Transitions - A Continuum Theory. Cambridge University Press. 46, 51, 52, 55

Acerbi, E., Bouchitté, G., Fonseca, I., 2003. Relaxation of convex functionals: The gap problem. Annales de l' Institut Henri Poincaré (C) Analyse non linéaire 20, 359–390. 51

Ahzi, S., M'Guil, S., 2008. A new intermediate model for polycrystalline viscoplastic deformation and texture evolution. Acta Materialia 56, 5359–5369. 45

Al-Samman, T., Gottstein, G., 2008. Room temperature formability of a magnesium AZ31 alloy: Examining the role of texture on the deformation mechanisms. Materials Science and Engineering A 488, 406–414. 33, 34, 106

Allain, S., Chateau, J.-P., Bouaziz, O., 2004. A physical model of the twinning-induced plasticity effect in a high manganese austenitic steel. Materials Science and Engineering A 387–389, 143–147. 45

Andrews, G., 1980. On the existence of solutions of the equation $u_{tt} = u_{xxt} + \sigma(u_x)_x$. Journal of Differential Equations 35, 200–231. 55

Andrews, G., Ball, J., 1982. Asymptotic behaviour and changes of phase in one-dimensional nonlinear viscoelasticity. Journal of Differential Equations 44, 306–341. 55

Asaro, R., Needleman, A., 1985. Overview 42: Texture development and strain-hardening in rate dependent polycrystals. Acta Metallurgica 33, 923–953. 55

Bacon, D., Liang, M., 1986. Computer simulation of dislocation cores in h.c.p. metals I. Interatomic potentials and stacking-fault stability. Philosophical Magazine A 53, 163–179. 35

Ball, J., 1977. Convexity conditions and existence theorems in nonlinear elasticity. Archive for Rational Mechanics and Analysis 63, 337–403. 51

Ball, J., Holmes, P., James, R., Pego, R., Swart, P., 1991. On the dynamics of fine structure. Journal of Nonlinear Science 1, 17–90. 55

Ball, J., James, R., 1987. Fine phase mixtures as minimizers of energy. Archive for Rational Mechanics and Analysis 100, 13–52. 55, 56, 115

Ball, J., James, R., 1992. Proposed experimental tests of a theory of fine microstructure, and the two-well problem. Philosophical Transactions of the Royal Society of London A 338, 389–450. 56

Barnett, M., 2003. A Taylor Model Based Description of the Proof Stress of Magnesium AZ31 during Hot Working . Metallurgical and Materials Transactions A 34 (9), 1799–1806. 79

Bartels, C., Carstensen, C., Hackl, K., Hoppe, U., 2004. Effective relaxation for microstructure simulations: algorithms and applications. Computer Methods in Applied Mechanics and Engineering 193, 5143–5175. 51, 56

Basinski, Z., Szczerba, M., Niewczas, M., Embury, J., Basinski, S., 1992. The transformation of slip dislocations during twinning of copper-aluminum alloy crystals. Revue de Metallurgie. Cahiers D'Informations Techniques 94, 1037–1043. 40

Bell, R., Cahn, R., 1957. The dynamics of twinning and the interrelation of slip and twinning in zinc crystals. Proceedings of the Royal Society of London A 239, 494–521. 77

Bertram, A., 2003. Finite thermoplasticity based on isomorphisms. International Journal of Plasticity 19, 2027–2050. 61

Bertram, A., 2005. Elasticity and Plasticity of Large Deformations. Springer Verlag, Berlin. 14, 61, 73, 80, 87

Bertram, A., Böhlke, T., Silhavy, M., 2007. On the rank 1 convexity of stored energy functions of physically linear stress-strain relations. Journal of Elasticity 86, 235–243. 51

Bilby, B., Crocker, A., 1965. The theory of the crystallography of deformation twinning. Proceedings of the Royal Society of London A 288, 240–255. 26

Bingert, J., Mason, T., Kaschner, G., Maudlin, P., Gray III, G., 2002. Deformation twinning in polycrystalline Zr: Insights from electron backscattered diffraction characterization. Metallurgical and Materials Transactions A: Physical Metallurgy and Materials Science 33, 955–963. 36

Böhlke, T., 2001. Crystallographic Texture Evolution and Elastic Anisotropy- Simulation, Modeling and Applications. Shaker Verlag. 45

Böhlke, T., 2004. The Voigt bound of the stress potential of isotropic viscoplastic FCC polycrystals. Archive of Mechanics 56, 423–443. 55

Böhlke, T., Bertram, A., 2001. The evolution of Hooke's law due to texture development in polycrystals. International Journal of Solids and Structures 38, 9437–9459. 73

Böhlke, T., Güge, R., Klöden, B., Skrotzki, W., Bertram, A., 2007. Finite element simulation of texture evolution and Swift effect in NiAl under torsion. Modelling and Simulation in Materials Science and Engineering 15, 619–637. 45

Böhlke, T., Risy, G., Bertram, A., 2006. Finite element simulation of metal forming operations with texture based material models. Modelling and Simulation in Materials Science and Engineering 14, 365–387. 45, 46

Bolling, G., Richman, R., 1965. Continual mechanical twinning. Acta Metallurgica, Parts I,II,III: Vol. 13, 709–757, Parts IV,V: Vol. 14, 637–647. 43

Born, M., Huang, K., 1954. Dynamical Theory of Crystal Lattices. Clarendon Press, Oxford. 11, 69

Boyko, V., Garber, R., Kossevich, A., 1994. Reversible Crystal Plasticity. AIP Press, New York. 30, 95, 100, 104, 105, 116

Bunge, H., 1977. Textur und Anisotropie Magnetischer Werkstoffe. Journal of Magnetism and Magnetic Materials 4, 305–320. 46

Cáceres, C., Lukác, P., Blake, A., 2008. Strain hardening due to $\{10\bar{1}2\}$ twinning in pure magnesium. Philosophical Magazine 88, 991–1003. 40

Cahn, R., 1953. Plastic deformation of alpha-uranium: twinning and slip. Acta Metallurgica 53, 49–70. 17

Cahn, R., Haasen, P. (Eds.), 1996. Physical Metallurgy. Vol. 3. Elsevier Science B.V., Ch. Mechanical properties of single phase crystalline media. 20

Carstensen, C., 2005. Ten remarks on nonconvex minimisation for phase transition simulations. Computer Methods in Applied Mechanics and Engineering 194, 169–193. 51, 55, 56

Chino, Y., Kimura, K., Mabuchi, M., 2008. Twinning behavior and deformation mechanisms of extruded az31 mg alloy. Materials Science and Engineering A 486, 481–488. 35

Christian, J., Mahajan, S., 1995. Deformation twinning. Progress in Materials Science 39, 1–157. 22, 26, 41, 42, 79, 95, 116

Clark, J., 1968. Age hardening in a Mg-9 wt.% Al alloy. Acta Metallurgica 16 (2), 141–152. 41

Clayton, J., 2009. A continuum description of nonlinear elasticity, slip and twinning, with application to sapphire. Proceedings of the Royal Society of London A 465, 307–334. 17

Collins, C., 1993. Computation of twinning. The IMA Volumes in Mathematics and its Applications Vol. 54. Springer Verlag, pp. 39 – 50. 47

Dafermos, C., 1969. The mixed initial-boundary value problem for the equations of nonlinear one-dimensional viscoelasticity. Journal of Differential Equations 6, 71–86. 55

Demczyk, B., 1990. Estimation of the surface energy in coherent-phase mixtures controlled by elastic-strain energy. Physical Review Letters B 42, 4738–4740. 39

Efendiev, M., Mielke, A., 2006. On the rate-independent limit of systems with dry friction and small viscosity. Journal of Convex Analysis 13, 151–167. 55

Emles, E., 1966. Principles of Magnesium Technology. Pergamon, Oxford. 37, 73

Ericksen, J., 1975. Equilibrium of bars. Journal of Elasticity 5, 191–202. 50, 53

Ericksen, J., 1980. Some phase transitions in crystals. Archive for Rational Mechanics and Analysis 73, 99–124. 47

Ericksen, J., 1984a. The Cauchy-Born hypothesis for crystals. In: Gurtin, M. (Ed.), Phase Transformations and Material Instabilities in Solids. Academic Press. 22

Ericksen, J., 1984b. Twinning of Crystals. Preprint Series of the Institute for Mathematics and its Application of the University of Minnesota 95, 1–18. 22, 115

Ericksen, J., 1991. On kinematic conditions of compatibility. Journal of Elasticity 26, 65–74. 22

Ericksen, J., 2000. On correlating two theories of twinning. Archive for Rational Mechanics and Analysis 153, 261–289. 69

Eshelby, J., 1957. The Determination of the Elastic Field of an Ellipsoidal Inclusion, and Related Problems. Proceedings of the Royal Society of London A 241, 376–396. 45

Ewing, J., Rosenhain, W., 1900. The crystalline structure of metals. Philosophical Transactions of the Royal Society of London A 193, 353–376. 9

Fisher, R., 1953. Dispersions on a sphere. Proceedings of the Royal Society of London A 217, 295–305. 46, 112

Fissel, A., Bugiel, E., Wang, C., Osten, H., 2006. Formation of Si twinning-superlattice: First steps towards Si-polytype growth. Materials Science and Engineering B 134, 138–141. 46

Forest, S., Parisot, R., 2000. Material crystal plasticity and deformation twinning. Rendiconti del Seminario Matematico della Università e Politecnico di Torino 58 (1), 99–111. 47, 69

Frommeyer, G., Brüx, U., Neumann, P., 2003. Supra-Ductile and High-Strength Manganese-TRIP/TWIP Steels for High Energy Absorption Purposes. ISIJ International 43, 483–446. 10

Gan, W., Wu, K., Zheng, M., Wang, X., Chang, H., Brokmeier, H.-G., 2009. Microstructure and mechanical property of the ECAPed $\mathrm{Mg_2Si/Mg}$ composite. Materials Science and Engineering A 516, 283–289. 37

Glüge, R., Böhlke, T., 2007. Micromechanical modeling of twinning. Proceedings in Applied Mathematics and Mechanics 7, 4060039–4060040. 57

Glüge, R., Kalisch, J., 2008. A lower bound estimation of a twinning stress for Mg by a stress jump analysis at the twin-parent interface. In: Bertram, A., Tomas, J. (Eds.), Micro-Macro-Interactions in Structured Media and Particle Systems. Springer-Verlag. 77, 104, 116

Govindjee, S., Mielke, A., Hall, G., 2003. The free energy of mixing for n-variant martensitic phase transformations using quasi-convex analysis. Journal of the Mechanics and Physics of Solids 51, 1–26. 51

Grassel, O., Frommeyer, G., 1998. Effect of martensitic phase transformation and deformation twinning on mechanical properties of Fe-Mn-Si-Al steels. Materials Science and Technology 14, 1213–1217. 10

Greenberg, M., 1969. On the existence, uniqueness, and stability of the equation $\rho_0 x_{tt} = e(x_x)x_{xx} + \lambda x_{xxt}$. Journal of Mathematical Analysis and Applications 25, 575–591. 55

Greenberg, M., MacCamy, R., 1970. On the exponential stability of solutions of $e(u_x)u_{xx} + \lambda u_{xtx} = \rho u_{tt}$. Journal of Mathematical Analysis and Applications 31, 406–417. 55

Greenberg, M., MacCamy, R., Mizel, V., 1968. On the existence, uniqueness, and stability of solutions of the equation $\sigma'(u_x)u_{xx} + \lambda u_{xtx} = \rho_0 u_{tt}$. Journal of Applied Mathematics and Mechanics 17, 707–728. 55

Haasen, P., 1996. Physical Metallurgy, 3rd Edition. Cambridge University Press. 39, 52, 55

Haferkamp, H., Jaschik, C., 2000. Magnesium-Tschenbuch. Aluminium-Zentrale Düsseldorf, Ch. Magnesium-Lithium-Legierungen, pp. 621–629. 37

Hales, T., 2006. Historical overview of the Kepler conjecture. Discrete and Computational Geometry 36, 5–20. 31

Hall, E., 1954. Twinning and Diffusionless Transformations in Metals. Butterworth Scientific Publications, London. 33

Hanson, R., 1985. Self-inverse integer matrices. The College Mathematics Journal 16, 190–198. 23, 25

Hartt, W., Reed-Hill, R., 1968. Internal deformation and fracture of second-order $\{10\bar{1}1\} - \{10\bar{1}2\}$-twins in magnesium. Transactions of the metallurgical society of AIME 242, 1127–1133. 35

Hencky, H., 1924. Zur Theorie plastischer Deformationen und der hierdurch im Material hervorgerufenen Nachspannungen. Zeitschrift für angewandte Mathematik und Mechanik 4, 323–334. 79

Hildebrand, F., Abeyaratne, R., 2008. An atomistic investigation of the kinetics of detwinning. Journal of the Mechanics and Physics of Solids 56, 1296–1319. 48

Hill, R., 1968. On constitutive inequalities for simple materials-I. Journal of the Mechanics and Physics of Solids 16, 229–242. 61

Hirth, J., 2000. Some current topics in dislocation theory. Acta Materialia 48, 93–104. 26, 29

Hu, Q., Li, L., Ghoneim, N., 2009. Stick-slip dynamics of coherent twin boundaries in copper. Acta Materialia 57, 4866–4873. 95

Hutchinson, J., 1976. Bounds and self-consistent estimates for creep of polycrystalline materials. Proceedings of the Royal Society of London A 348, 101–127. 55

Idesman, A., Levitas, V., Stein, E., 2000. Structural changes in elastoplastic material: a unified finite-element approach to phase transformation, twinning and fracture. International Journal of Plasticity 16 (7), 893–949. 47

Igarashi, M., Khantha, M., Vitek, V., 1991. N-body potentials for hexagonal closed-packed metals. Philosophical Magazine B 63, 603–627. 35

Jiang, L., Jonas, J., Boyle, K., Martin, K., 2008. Deformation behavior of two mg alloys during ring hoop tension testing. Materials Science and Engineering A 492, 68–73. 43

Jiang, L., Jonas, J., Mishrab, R., Luob, A., Sachdevb, A., Godetc, S., 2007. Twinning and texture development in two Mg alloys subjected to loading along three different strain paths. Acta Materialia 55, 3899–3910. 36, 106, 108, 110, 111, 113, 116

Jin, Z.-H., Gumbsch, P., Albe, K., Ma, E., Lu, K., Gleiter, H., Hahn, H., 2008. Interactions between non-screw lattice dislocations and coherent twin boundaries in face-centered cubic metals. Acta Materialia 56, 1126–1135. 48

Karaman, I., Sehitoglu, H., Gall, K., Chumlyakov, Y., Maier, H., 2000. Deformation of single crystal Hadfield steel by twinning and slip. Acta materialia 48, 1345–1359. 10

Kastner, O., Ackland, G., 2009. Mesoscale kinetics produces martensitic microstructure. Journal of the Mechanics and Physics of Solids 57, 109–121. 48

Kawabata, K., Hosokawa, Y., Saga, T., Sambongi, T., 2000. Real-time observation of twin boundary motion in crystals: an ideal dry friction system. Tribology Letters 9, 41–44. 47, 95

Kaya, A., Yucel, O., Eliezer, D., Aghion, E., 2004. An Electron Microscopy Investigation on as-cast AZ91D Alloy Modified with Nitrogen. In: Kainer, K. (Ed.), Magnesium: proceedings of the 6th International Conference Magnesium Alloys and their Applications. John Wiley and Sons. 42

Kelley, E., Hosford, W. J., 1968. Plane-strain compression of magnesium and magnesium alloy crystals. Transactions of the Metallurgical Society of AIME 242, 5–13. 33, 35, 37

Khachaturyan, A., 1983. Theory of Structural Transformations in Solids. Wiley, New York. 39

Kim, W., Kim, M., Wang, J., 2009. Ultrafine-grained Mg-9Li-1Zn alloy sheets exhibiting low temperature superplasticity. Materials Science and Engineering A 516, 17–22. 37

Klassen-Neklyudova, M., 1964. Mechanical twinning of crystals. New York: Consultants Bureau. 20

Kochmann, D., Le, K., 2009. A continuum model for initiation and evolution of deformation twinning. Journal of the Mechanics and Physics of Solids 57, 987–1002. 40, 95, 116

Koike, J., 2005. Enhanced Deformation Mechanisms by Anisotropic Plasticity in Polycrystalline Mg Alloys at Room Temperature. Metallurgical and Materials Transactions A 36, 1689–1696. 35, 77, 79

Korobeynikov, S., 2008. Objective tensor rates and applications in formulation of hyperelastic relations. Journal of Elasticity 93, 105–140. 13

Lambrecht, M., Miehe, C., Dettmar, J., 2003. Energy relaxation of non-convex incremental stress potentials in a strain-softening elastic-plastic bar. International Journal of Solids and Structures 40, 1369–1391. 51

Lapczyk, I., Rajagopal, K., Srinivasa, A., 2000. Deformation twinning during impact of a titanium cylinder- numerical calculations using a constitutive theory based on multiple natural configurations. Computer Methods in Applied Mechanics and Engineering 188, 527–541. 47

Laves, F., 1966. What is a twin and what is a "twin". Acta Metallurgica 14, 58, Letter to the editor. 43

Lay, S., Nouet, G., 1994. Interaction of slip dislocations with the (0112) twin interface in zinc. Philosophical Magazine A 70, 1027–1044. 35

Li, B., Joshi, S., Azevedo, K., Ma, E., Ramesh, K., Figueiredo, R., Langdon, T., 2009. Dynamic testing at high strain rates of an ultrafine-grained magnesium alloy processed by ECAP. Materials Science and Engineering A 517, 24–29. 37

Li, B., Ma, E., 2009a. Atomic shuffling dominated mechanism for deformation twinning in magnesium. Physical Review Letters 103, 35503–1–4. 36

Li, B., Ma, E., 2009b. Zonal dislocations mediating $\{1011\}\langle 1012\rangle$ twinning in magnesium. Acta Materialia 57, 1734–1743. 36, 48

Liu, I.-S., 2002. Continuum Mechanics. Springer, Berlin. 14, 21

Liu, K., Zhang, J., Rokhlin, L., Elkin, F., Tang, D., Meng, J., 2009. Microstructures and mechanical properties of extruded Mg-8Gd-0.4Zr alloys containing Zn. Materials Science and Engineering A 505, 13–19. 41

Liu, X., Adams, J., Ercolessi, F., Moriarty, J., 1996. EAM potential for magnesium from quantum mechanical forces. Modelling and Simulation in Materials Science and Engineering 4, 293–303. 36, 48

Lou, X., Li, M., Boger, R., Agnew, S., Wagoner, R., 2007. Hardening evolution of AZ31B Mg sheet. International Journal of Plasticity 23, 44–86. 41

Lubenets, S., Startsev, V., Fomenko, L., 1980. Elastic Twinning in In-10 Wt% Pb Alloy. Kristall und Technik 15, K78–K80. 40, 43

Ma, A., Jiang, J., Saito, N., Shigematsu, I., Yuan, Y., Yang, D., Nishida, Y., 2009. Improving both strength and ductility of a Mg alloy through a large number of ECAP passes. Materials Science and Engineering A 513-514, 122–127. 37

Maksoud, I., Ahmed, H., Rödel, J., 2009. Investigation of the effect of strain rate and temperature on the deformability and microstructure evolution of AZ31 magnesium alloy. Materials Science and Engineering A 504, 40–48. 41

Meng, L., Yang, P., Xie, Q., Mao, W., 2008. Analysis on compression twins in Magnesium. Materials Transactions 49, 710–714. 33

Müller, I., Villaggio, P., 1977. A model for an elastic-plastic body. Archive for Rational Mechanics and Analysis 65, 25–46. 49

Muránsky, O., Carr, D., Šittner, P., Oliver, E., 2009. In situ neutron diffraction investigation of deformation twinning and pseudoelastic-like behaviour of extruded AZ31 magnesium alloy. International Journal of Plasticity 25, 1107–1127. 110

Naumann, C., 1830. Lehrbuch der reinen und angewandten Krystallographie. F. A. Brockhaus, Leipzig. 9

Neumann, P., 1966. Vereinfachung kristallographischer Rechnungen in hexagonalen Gittern durch konsequente Benutzung des vierachsigen hexagonalen Koordinatensystems. Physica Status Solidi 17, K71–K74. 28

Pagano, S., Alart, P., 1999. Solid-solid phase transition modelling: relaxation procedures, configurational energies and thermomechanical behaviours. International Journal of Engineering Science 37, 1821–1840. 51

Partridge, P., 1965. Irregular Twin Growth and Contraction in Hexagonal Close Packed Metals. Acta Metallurgica 13, 1330–1335. 33

Pego, R., 1987. Phase transitions in one-dimensional nonlinear viscoelasticity: Admissibility and stability. Archive for Rational Mechanics and Analysis 97, 353–394. 52, 55

Peigney, M., 2009. A non-convex lower bound on the effective energy of polycrystalline shape memory alloys. Journal of the Mechanics and Physics of Solids 57, 970–986. 51

Petryk, H., Fischer, F., Marketz, W., Clemens, H., Appel, F., 2003. An energy approach to the formation of twins in TiAl. Metallurgical and Materials Transactions A: Physical Metallurgy and Materials Science 34, 2827–2836. 39

Pitteri, M., Zanzotto, G., 2002. Continuum Models for Phase Transitions and Twinning in Crystals. Chapman and Hall/CRC. 17, 20, 28, 31, 47, 69

Proust, G., Tomé, C., Jain, A., Agnew, S., 2009. Modeling the effect of twinning and detwinning during strain-path changes of magnesium alloy AZ31. International Journal of Plasticity 25, 861–880. 46

Ramberg, W., Osgood, W., 1943. Description of stress-strain curves by three parameters. Technical Note No. 902 , 1–28. 79

Reed-Hill, R., 1960. A study of the $\{10\bar{1}1\}$ and $\{10\bar{1}3\}$ twinning modes in Magnesium. Transactions of the Metallurgical Society of AIME 218, 554–558. 33

Reed-Hill, R., 1973. The Inhomogeneity of Plastic Deformation. American Society for Metals, Ch. Role of Deformation Twinning in Determining the Mechanical Properties of Metals, pp. 285–311. 42, 108, 110, 112

Reed-Hill, R., Abbaschian, R., 1994. Physical Metallurgy Principles. PWS Publishing Company. 29, 30, 42, 77

Reed-Hill, R., Robertson, W., 1957a. Additional modes of deformation twinning in magnesium. Acta Metallurgica 5, 717–727. 20, 33

Reed-Hill, R., Robertson, W., 1957b. The crystallographic characteristics of fracture in magnesium single crystals. Acta Metallurgica 5, 728–737. 33

Regener, D., Dietze, G., 2006. Temperature and time-dependent precipitation behaviour of the pressure die cast alloy AZ91. Praktische Metallographie/Practical Metallography 43 (7), 334–348. 41

Regener, D., Dietze, G., Schröder, A., Pinkernelle, A., 2007. The microstructure and mechanical properties of pressure die cast magnesium-lithium alloys. Praktische Metallographie/Practical Metallography 44 (1), 17–32. 37

Roberts, E., Partridge, P., 1966. The accommodation around $\{10\bar{1}2\}\langle\bar{1}011\rangle$ twins in magnesium. Acta Metallurgica 14, 513–527. 33, 101, 102, 116

Roubíček, T., 2004. Nonlinear Homogenization and its Applications to Composites, Polycrystals and Smart Materials. Kluwer Academic Publishers, Ch. Models of Microstructure Evolution in Shape Memory Alloys, pp. 269–304. 45, 56

Sato, T., Kral, M., 2008. Microstructural evolution of Mg-Al-Ca-Sr alloy during creep. Materials Science and Engineering A 498, 369–376. 41

Schmid, M., Biedermann, A., Stadler, H., Varga, P., 1992. Lattice mismatch dislocations in a preferentially sputtered alloy studied by scanning tunneling microscopy. Physical Review Letters 69, 925–928. 31

Schmidt, B., 2008. Linear Γ -limits of multiwell energies in nonlinear elasticity theory. Continuum Mechanics and Thermodynamics 20, 375–396. 51

Serra, A., Bacon, D., 1986. Computer simulation of twin boundaries in the h.c.p. metals. Philosophical Magazine A 54, 793–804. 35

Serra, A., Bacon, D., 1991. Computer simulation of twinning dislocation in magnesium using a many-body potential. Philosophical Magazine A 63, 1001–1012. 35, 36, 39, 40

Serra, A., Bacon, D., 1996. A new model for $\{10\bar{1}2\}$ twin growth in hcp metals. Philosophical Magazine A 73, 333–343. 35

Sevillano, J., 2009. An alternative model for the strain hardening of FCC alloys that twin, validated for twinning-induced plasticity in steel. Scripta Materialia 60, 336–339. 40

Shiekhelsouk, M., Favier, V., Inal, K., Cherkaoui, M., 2009. Modelling the behaviour of polycrystalline austenitic steel with twinning-induced plasticity effect. International Journal of Plasticity 25, 105–133. 74

Sidi Ammi, M., Torres, D., 2008. Regularity of Solutins of the Autonomous Integrals of the Calculus of Variations. In: Differential Equations, Chaos and Variational Problems. Springer. 52

Silling, S., 1989. Phase changes induced by deformation in isothermal elastic crystals. Journal of the Mechanics and Physics of Solids 37, 293–316. 47

Simmons, G., Wang, H., 1971. Single Crystal Elastic Constants and Calculated Aggregate Properties: A Handbook. The M.I.T. Press. 89

Simo, J., Hughes, T., 1998. Computational Inelasticity. Springer-Verlag, New York. 56, 80, 87

Sleeswyk, A., 1964. Emissary dislocation-twin interactions and twin growth. Acta Metallurgica 12, 669–673, letter to the editor. 43

Smola, B., Stulíková, I., Pelcová, J., Mordike, B., 2004. Significance of stable and metastable phases in high temperature creep resistant magnesium-rare earth base alloys. Journal of Alloys and Compounds 378, 196–201. 41, 42

Stanford, N., 2008. Observation of $\{11\bar{2}1\}$ twinning in a Mg-based alloy. Philosophical Magazine Letters 88, 379–386. 33

Stanford, N., Barnett, M., 2008. The origin of ”rare earth” texture development in extruded Mg-based alloys and its effect on tensile ductility. Materials Science and Engineering A 496, 388–408. 37

Stanford, N., Barnett, M., 2009. Effect of particles on the formation of deformation twins in a magnesium-based alloy. Materials Science and Engineering A 516, 226–234. 41

Stark, J., 1988. Mechanical twinning in crystals. Physical Review B 38, 1139–1142. 22

Staroselsky, A., Anand, L., 2003. A constitutive model for hcp materials deforming by slip and twinning: application to magnesium alloy AZ31B. International Journal of Plasticity 19 (10), 1843–1864. 10

Straumal, B., Sursaeva, V., Polyakov, S., 2001. Faceting and Roughening of the Asymmetric Twin Grain Boundaries in Zinc. Interface science 9, 275–279. 77

Thompson, M., Hingley, M., 1955. The formation of mechanical twins. Acta Metallurgica 3, 289–291. 79

Thornton, P., 1966. Reply on discussion "On {10.1} twinning in the h.c.p. structure". Acta Metallurgica 14, 444–445, letter to the editor. 28

Tomé, C., Lebensohn, R., Kocks, U., 1991. A model for texture development dominated by deformation twinning: application to zirconium alloys. Acta Metallurgica et Materialia 39, 2667–2680. 10, 45

Truesdell, C. A., Noll, W., 1965. The Non-linear Field Theories of Mechanics. Springer, Berlin, Ch. Volume III/3 of the Encyclopedia of Physics. 61

Truskinovsky, L., Zanzotto, G., 1996. Ericksen's bar revisited: energy wiggles. Journal of the Mechanics and Physics of Solids 44, 1371–1408. 39, 55

Ungár, T., Glavicic, M., Balogh, L., Nyilas, K., Salem, A., Ribárik, G., Semiatin, S., 2008. The use of X-ray diffraction to determine slip and twinning activity in commercial-purity (CP) titanium. Materials Science and Engineering A 493, 79–85. 35

Wang, Y., Jin, Y., Khachaturyan, A., 2004. The Effects of Free Surfaces on Martensite Microstructures: 3D Phase Field Microelasticity Simulation Study. Acta Materialia 52 (4), 1039–1050. 47

Westlake, D., 1966. On {10.1} twinning in the h.c.p. structure. Acta Metallurgica 14, 442–444, letter to the editor. 28

Wonsiewicz, B., Backofen, W., 1967. Plasticity of magnesium crystals. Transactions of the metallurgical society of AIME 239, 1422–1431. 33, 35, 79

Wu, L., Agnew, S., Brown, D., Stoica, G., Clausen, B., Jain, A., Fielden, D., Liaw, P., 2008. Internal stress relaxation and load redistribution during the twinning-detwinning-dominated cyclic deformation of a wrought magnesium alloy, ZK60A. Acta materialia 56, 3699–3707. 43

Xu, D., Wang, H., Yang, R., Veyssière, P., 2008. Molecular dynamics investigation of deformation twinning in γ-TiAl sheared along the pseudo-twinning direction. Acta Materialia 56, 1056–1074. 48

Yi, S., Schestakow, I., Zaefferer, S., 2009. Twinning-related microstructural evolution durcing hot rolling and subsequent annealing of pure magnesium. Materials Science and Engineering A 516, 58–64. 35

Yin, S., Yang, F., Yang, X., Wu, S., Li, S., Li, G., 2008. The role of twinning-detwinning on fatigue fracture morphology of Mg-3%Al-1%Zn alloy. Materials Science and Engineering A 494, 397–400. 35

Zanzotto, G., 1992. On the material symmetry group of elastic crystals and the Born rule. Archive for Rational Mechanics and Analysis 121, 1–36. 22, 33, 69, 115

Zanzotto, G., 1996. The Cauchy-Born Hypothesis, Nonlinear Elasticity and Mechanical Twinning in Crystals. Acta Crystallographica A 52, 839–849. 69, 115

Index